Abstract

Development of quantitative optical techniques for microgravity combustion and sooty

flame characterization

Bin Ma

2013

In order to design cleaner and more efficient practical combustion devices, such as engines and gas turbines, fundamental understanding of combustion processes, accurate diagnostic techniques and computational models are required. Optical diagnostic techniques, being non-intrusive and in-situ, are a powerful tool for characterizing combustion systems.

A color-ratio pyrometry technique using a consumer digital single lens reflex camera was developed with single-shot measurement capabilities. The technique was found to work well with SiC fibers and soot for flame temperature and soot volume fraction measurements. A novel absolute light intensity calibration method using S-type thermocouples was also developed, which offers a robust and low-cost alternative solution for traditional calibration approaches, for example expensive blackbody sources and calibrated tungsten lamps. The developed diagnostic techniques have been applied in microgravity combustion experiments completed on the International Space Station; the measured results provide ideal test cases free from buoyancy effects to improve the current computational models.

Soot radius of gyration in the Yale standard coflow laminar diffusion flames has been measured in two dimensions by using the newly developed 2-D multi-angle light scattering technique. Extinction has also been measured by a spectrally resolved line-of-sight attenuation method. These measurements further complete our understanding of soot formation, provide insights on spectral emissivities of soot at different aging stages (e.g., young soot or mature soot), and were shown to improve the accuracy of soot color-ratio pyrometry measurements.

Development of quantitative optical techniques for microgravity combustion and sooty flame characterization

A Dissertation

Presented to the Faculty of the Graduate School

of

Yale University

in Candidacy for the Degree of

Doctor of Philosophy

by

Bin Ma

Dissertation Director: Professor Marshall B. Long

September 2013

iii

Acknowledgements

I would like to express my very great appreciation to my advisor Professor Marshall Long, who brought me into the exciting field of optical diagnostics of combustion, for his invaluable guidance and support throughout my five years study at Yale University. I would also like to thank my dissertation committee members Professor Mitchell Smooke and Professor Alessandro Gomez for their insightful suggestions along the way, and Professor Thomas Dreier who graciously agreed to be the outside reader of my dissertation thesis.

I would like to thank my lab mates who kept me accompanied and shared joys and pains. They are Blair Connelly, Peter Kuhn, Federico Mella, Davide Giassi and Nathan Kempema. Their always-ready helping hands have made my dissertation research much easier.

My thanks are also due to my collaborators who have made the thesis possible. Specifically, they are Dr. Beth Anne Bennett and Mr. Su Cao in Professor Smooke's group, Mr. Dennis Stocker and Dr. Fumiaki Takahashi at NASA Glenn research center, Dr. Guanghua Wang at GE global research center, Dr. Robert Barlow and Dr. Gaetano Magnotti at Sandia national laboratories.

I would also like to thank all my friends at Yale University who have made graduate school considerably more enjoyable.

Finally and most importantly, I would like to thank my wife, Xiaowei Chen, who has made my life fulfilled with overwhelming love and joys, and my parents, Aiying Li and Heping Ma, for their everlasting support and trust.

Table of Contents

List of Figures

1 Introduction

More than seventy percent of the world's energy is contributed from energy generation via combustion. Despite the rise of alternative energy sources, burning fossil fuels is still the most prevalent energy generation approach, and is very hard to replace in many applications given the high energy density of fossil fuels and the tremendous amount of existing infrastructure. The demand for fossil fuel is increasing and will not peak in the near future. On the other hand, environmental issues such as the emission of soot particulates and NO_x along with their role in global warming are a byproduct of combustion processes. Stringent regulations have been enacted over the years to advance the development of cleaner and more efficient combustion. In order to design better practical combustion devices, such as engines and gas turbines, fundamental understanding of combustion processes along with accurate diagnostic techniques and computational models are needed.

Diffusion flames are the flame type of most practical combustion devices. Over the previous decades, systematic research on coflow laminar diffusion flames has been carried out experimentally in Professor Long's lab and computationally in Professor Smooke's lab; both diagnostic expertise and computational models continue to develop. Quantitative measurements have been compared with computational results over a wide spectrum of dilution levels, from non-sooty to sooty flames. Good agreement on various quantities, e.g., temperature and species concentration, is achieved between computation and experiments. However, discrepancies still exist at certain flame conditions. While normal gravity combustion studies can provide important information on combustion

processes, conducting the experiment in a microgravity environment has the advantage that buoyancy effects are eliminated, which simplifies the interpretation of both computational and experimental results. In addition, the microgravity environment will enable the stabilization of flames with increased levels of dilution and will help generate flames that have increased soot residence times compared to normal gravity facilities. In general, microgravity is an ideal condition to study flames near extinction and soot formation by eliminating complexities and providing 'cleaner' tests to refine the current computational models. Yale is responsible for two International Space Station (ISS) - based microgravity combustion projects that are joint experimental and computational studies focusing on coflow laminar diffusion flames. Traditional laser-based measurements and other techniques involving complex optical setups are difficult to implement on the ISS due to limited space and safety concerns. Simple, robust and accurate diagnostic techniques must be developed to adapt to the limited experimental capabilities in order to make the comparison between experiments and computations as quantitative as possible. One of the major efforts of my dissertation research focuses on the development of simple and robust diagnostic techniques for gas phase and soot temperature and volume fraction measurement. The techniques developed were applied in the ISS-based experiments in order to yield more knowledge of flame behavior in microgravity and to provide test cases free from buoyancy effects to validate and improve the computational models developed in Professor Mitchell Smooke's group.

Accurate temperature measurements are desired in many applications, given the fact that temperature is a crucial parameter for combustion chemical kinetics and is often critical in validating the design of practical combustion devices to prevent material failure

due to over heating. The temperature diagnostic technique, thin-filament pyrometry (TFP), is potentially easier to implement in practical combustion environments compared with laser-based techniques. A detailed study on the accuracy and uncertainties of the technique has been performed.

Built upon soot characterization done in previous dissertations from Professor Long's lab, soot radius of gyration measurements and spectrally resolved extinction measurements have also been performed to further complete our understanding of the Yale standard coflow laminar diffusion flames. Multiple measurements on the standard flames are shown to yield insights on the soot spectral emissivity and improve the accuracy of soot pyrometry measurements.

Overall, this dissertation touches on several aspects of optical diagnostics of combustion, including pyrometry, absolute light calibration, soot scattering and extinction, and microgravity experiments. The structure of the thesis is outlined below.

Chapter 2 describes the development of simple and robust techniques including color-ratio pyrometry using a digital single lens reflex camera and absolute light calibration using S-type thermocouples. The camera's built-in Bayer pattern red, green and blue (RGB) filter array allows simultaneous flame imaging in different color bands and makes temperature measurement possible within a single shot. The S-type thermocouple provides a low-cost and robust alternative solution for performing absolute light calibration rather than using an expensive and bulky blackbody source or calibrated tungsten lamps. The working principles of the techniques along with their applications are discussed in detail.

Chapter 3 focuses on recent developments in thin-filament pyrometry. It reviews and discusses two TFP approaches – namely the intensity-ratio and color-ratio approaches, identifies and investigates their associated error sources such as fiber aging, greybody behavior and radiation correction, and directly assesses different TFP approaches against N_2 CARS measurements in well-calibrated flames. Finally, results of uncertainty analysis are presented along with suggestions on ways to reduce measurement uncertainty.

Chapter 4 presents the measurements made in the microgravity SLICE project and the pre-investigation of pressure effects for the CLD flame project. The optical diagnostic techniques discussed in Chapter 2 and 3 are used for temperature and soot volume fraction measurements. Corresponding computational simulations, performed by Professor Smooke's group, are also shown for comparison and better understanding of the gravitational and pressure effects.

Chapter 5 presents multiple measurements that further complete our characterizations on the Yale standard flames. An innovative 2-D multi-angle light scattering technique was developed to extend the traditional point measurements into two dimensions, which enabled soot radius of gyration to be determined for the full flame. Spatially and spectrally resolved extinction measurements were also obtained by performing spectral line-of-sight attenuation with Abel inversion. Combining with the previous measurements on soot primary particle size done in Professor Long's lab, the dispersion exponent and the spectral emissivity wavelength dependence can be determined in two dimensions and used to improve the soot ratio-pyrometry measurements.

Finally, Chapter 6 provides some concluding remarks and comments on future directions.

2 Development of simple optical diagnostics

2.1 Introduction

Emission-based techniques, compared with laser-based techniques, generally employ a simpler optical setup, require less optical access and also have much lower cost. These advantages make the emission-based techniques suitable for many environments that are hard to adapt to the requirements of laser measurements. In our ISS-based microgravity experiments, due to the limited space, power supply and safety regulations, only simple experiments can be carried out. One of our major efforts is concentrating on development of simple yet accurate diagnostic techniques for making the comparison between experiments and computations as quantitative as possible. A technique utilizing a color digital camera has been developed that allows observation of flame shape, size, lift-off height, and measurements of temperature via soot and thin-filament pyrometry and a quantitative determination of soot volume fraction. Techniques for obtaining an absolute light calibration have also been developed, which is essential for measuring the absolute soot volume fraction and the number density of chemiluminescent species such as CH*. In Section 2.2, color-ratio pyrometry using digital single lens reflex (DSLR) cameras for temperature measurement based on soot radiation and thin-filament radiation will be introduced and discussed, with focus on the principle and application of the methods. The underlying assumptions, such as the thin-filament greybody assumption and aging behavior, and soot spectral emissivity wavelength dependence (i.e., the soot dispersion exponent) will be discussed in Chapters 3 and 5 respectively. In Section 2.3, a novel absolute light calibration approach using S-type thermocouples will be introduced and discussed in detail.

6

2.2 Soot and thin-filament color-ratio pyrometry using a DSLR

2.2.1 Introduction

Knowledge of temperature and soot concentration can prove valuable in understanding the processes responsible for soot production. Optical pyrometry has proven to be a practical measurement technique that can provide the temperature and concentration of soot particles in a flame by sampling the incandescence of soot that has been heated to flame temperatures [Levendis 1992; Beatrice 1995; Panagiotou 1996; De Iuliis 1998a; Cignoli 2001; Snelling 2002]. In regions where soot is not present, gas temperatures have been inferred from pyrometry of thin filaments inserted into a flame [Vilimpoc 1989; Pitts 1996; Pitts 1998; Struk 2003; Maun 2007]. Prior pyrometry methods have incorporated a variety of detection methods ranging from single photodetectors to scientific-grade imagers. Recently, Maun *et al.* [Maun 2007] provided an overview of imaging systems used for pyrometry measurements and further showed that a consumer-grade digital camera could provide results for thin filament pyrometry (TFP). In their work, the total intensity of light was measured with the camera and correlated to thermocouple temperature measurements.

In the work described here, a color digital camera is also utilized, but the ratio of two colors is used to determine the temperature of both soot and a SiC fiber inserted into nonsooting regions of a coflow diffusion flame. Incandescence from the soot and the fiber is imaged at the three wavelengths of the camera's color filter array (CFA) and the temperature is calculated using two-color ratio pyrometry [Levendis 1992; De Iuliis 1998a; Cignoli 2001]. It is further demonstrated that the image of the filament can provide an absolute intensity calibration, which allows calculation of the soot volume

fraction.

2.2.2 Camera characterization

Over the last several years, a number of digital single lens reflex (DSLR) cameras have been introduced, with a steady increase in performance factors such as resolution, dynamic range, and sensitivity. The possibility of using these detectors for quantitative measurements is attractive from the standpoint of cost, but their suitability for such an application is not a given, since consumer digital cameras are not designed for use as scientific detectors. To establish the reliability of the cameras for quantitative work, the performance of three cameras was investigated under controlled conditions. It is important to avoid some of the built-in image processing algorithms that are appropriate for snapshots, but could invalidate the assumption that the signal can be related linearly to light intensity. Fortunately, many consumer digital cameras have the ability to record images in "raw" mode, which minimizes the internal processing of the information read from the camera chip.

Three representative cameras from recent generations of consumer DSLRs are characterized and used for pyrometry measurements – the Nikon D70, D90 and D300s. Each offers the necessary manual user control of settings and 12-bit or higher raw data format at a reasonable price. The D70 is based on a CCD detector (23.7 mm × 15.6 mm) with 6.1 million (effective) pixels (2014 x 3040). The D90 and D300s utilize a CMOS sensor (23.6 mm × 15.8 mm) with 12.9 million pixels (2848 x 4288). The D90 and D300s are newer cameras compared to the D70 with higher prices and more advanced features, such as faster data transfer speed, more bracket settings and a live view mode. Since our use of these cameras is for scientific purposes rather than artistic creation, all image

enhancement options, such as sharpness, contrast, color, and saturation, were set to either "normal" or "none," as applicable, in order to ensure shot-to-shot consistency. The ISO number was set to 200 (the lowest standard setting). A white balance of "direct sunlight" was selected, but this setting simply specifies a set of color balance multipliers that were not used in processing the image data. Files were saved in the camera's "NEF" format, which is a 12-bit (14 bit for the D300s) lossless compressed raw format. Although used by many camera manufacturers as a designation for unprocessed images, raw is not a standardized format (unlike TIF, JPG, etc.). Consequently, some careful examination of the resulting image is necessary to ensure consistent reconstruction of the underlying intensity data. To facilitate a more transparent analysis, the open-source image-processing software OMA [Kalt 2013] was used to capture images, transfer them to the computer, and perform subsequent processing. Decoding of the Nikon-specific data format is done within the OMA program using a publicly available software library [Coffin 2013].

It was verified that the signal detected by all cameras in all three channels decreased linearly with attenuation and increased linearly with exposure, up to the point where the channels saturate. Results from the D70 are shown in Fig. 2.1 as an example. The signal is seen to increase linearly with increasing exposure time up to the point of saturation. A line fit to the data in the linear region results in an R^2 value that is greater than 0.999 for all three color channels. Within the linear region, the signal ratio between the different color channels exhibits a standard deviation of 1% across all data triplets. In the following work, the cameras were operated in this linear regime.
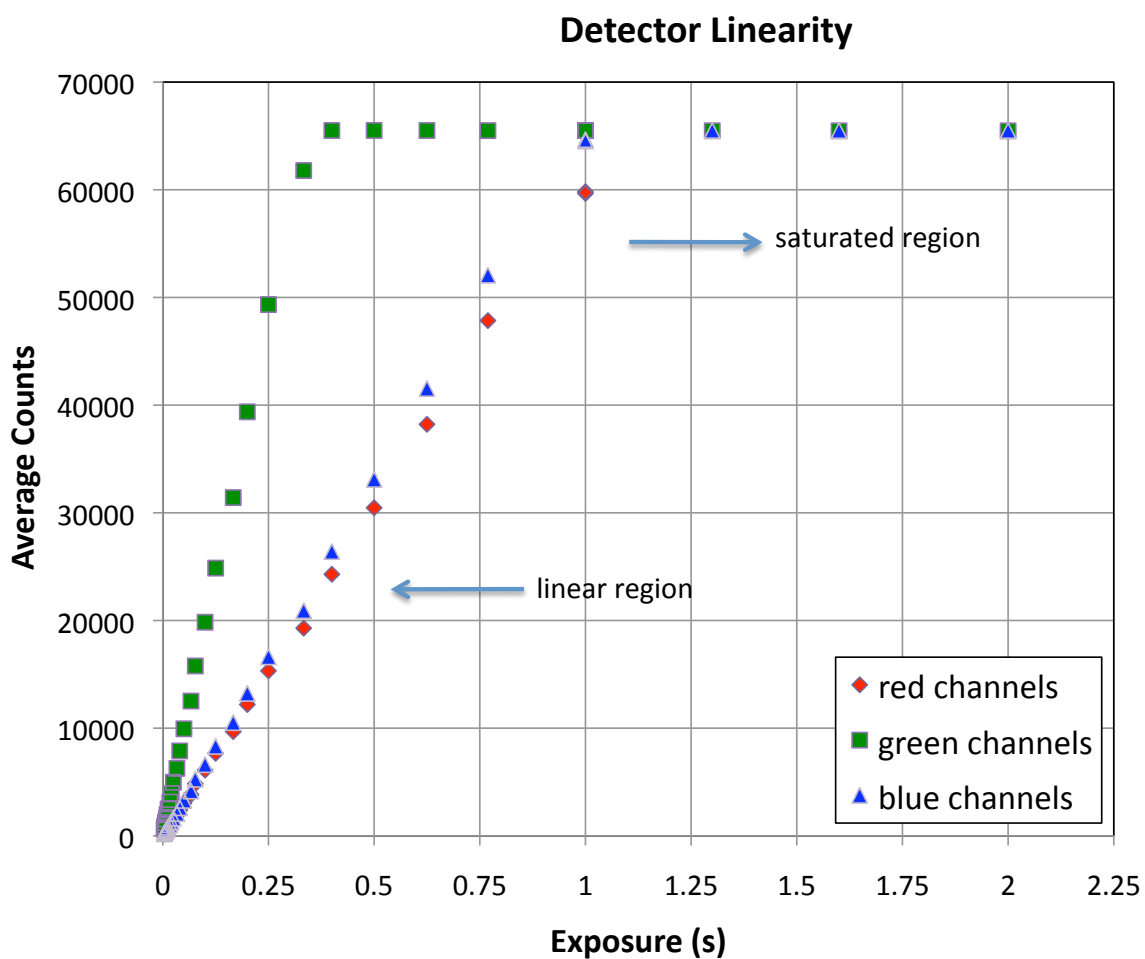
Fig. 2.1. The average signal obtained with a D70 camera in the center of the sooting region of a 40% C_2H_4 flame as a function of increasing exposure time. A BG colored glass filter was used to equalize the intensity in the three spectral channels.

The pyrometry experiments described below require characterization of the spectral response of the detector/CFA system, which is not available from the manufacturer. To provide this data, the spectrum of an illumination source was imaged onto a ground glass diffuser (DG20-1500) using an imaging spectrograph (Jobin Yvon CP200), with a 200 groove/mm grating and a 0.05 mm entrance slit as shown in Fig. 2.2.
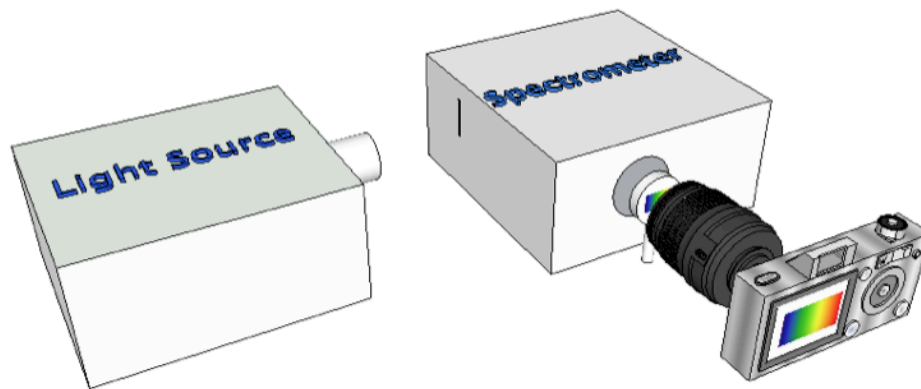
Fig. 2.2. Experimental setup for measuring the camera spectral response

The dispersed spectrum was imaged onto each digital camera through a Nikkor 50 mm f/1.4 lens. The data were separated into three images corresponding to the red, green, and blue (RGB) channels of the CFA. Spectral scaling was determined by imaging the 404.7 nm, 435.8 nm, 546 nm and 578.2 nm lines from a mercury vapor lamp. Normalization for the spectrum of the illumination source and optical throughput of the spectrograph was obtained by imaging the spectrum with a scientific camera (Cooke Sensicam with SuperVGA sensor), whose typical spectral response has been tabulated by the manufacturer. The illumination source (Dolan-Jenner Fiber-Lite series 180) was observed to be stable, giving no noticeable variation over time. All components used

11

were fixed in position, with the lens aperture set to f/2. Only the camera body was changed for different measurements. A BG color glass filter is found useful to provide better balance between the red, green, and blue intensities that are encountered in the pyrometry experiments. Color glass filters are available in different thicknesses, resulting in different transmission levels; the one used in this study reduced the intensity at 600 nm by 86 % and closely resembled the behavior of 1 mm thickness BG-7 filter manufactured by SCHOTT Inc. [08/2013b]. The measured spectral response curves of the three cameras are shown in Fig. 2.3. The RGB channels from all three cameras show similar characteristics – significant spectral overlap between channels, with a shape not accurately represented by a single Gaussian curve. The BG glass filter transmission is shown in Fig. 2.4.
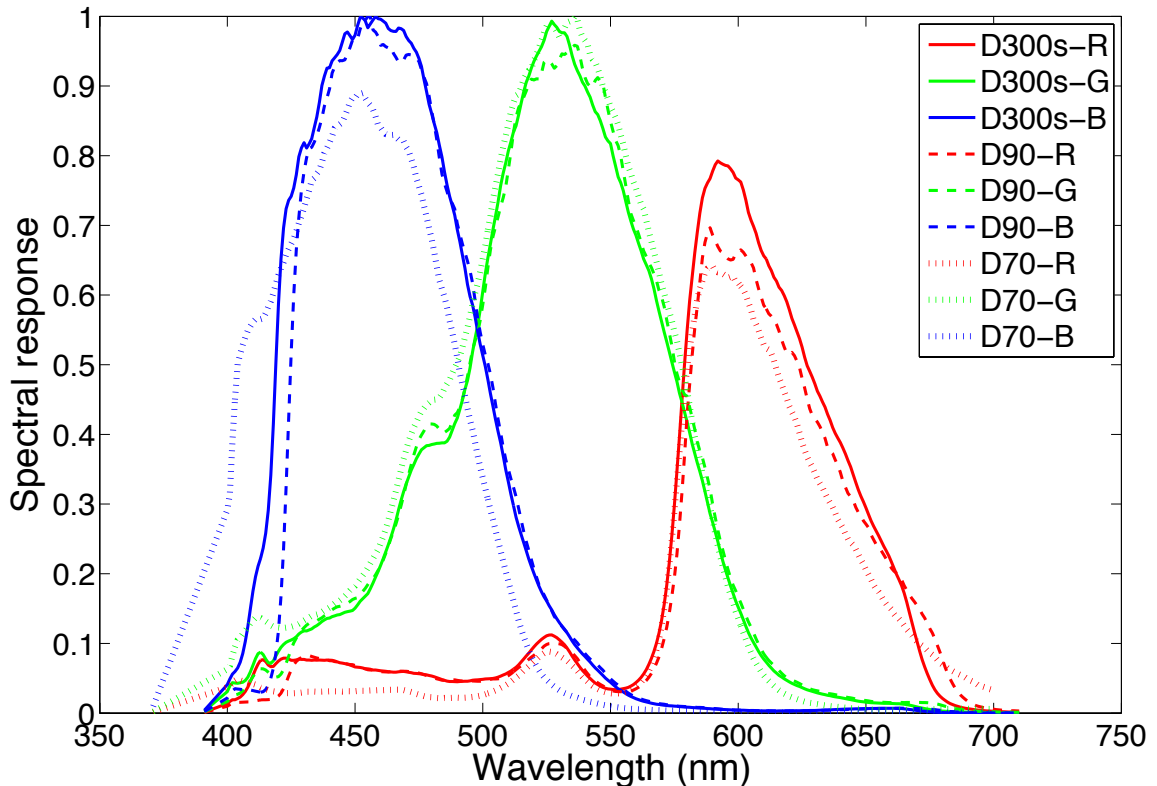
Fig. 2.3. Nikon D70, D90 and D300s spectral response curves for the blue, green and red filters (from left to right).
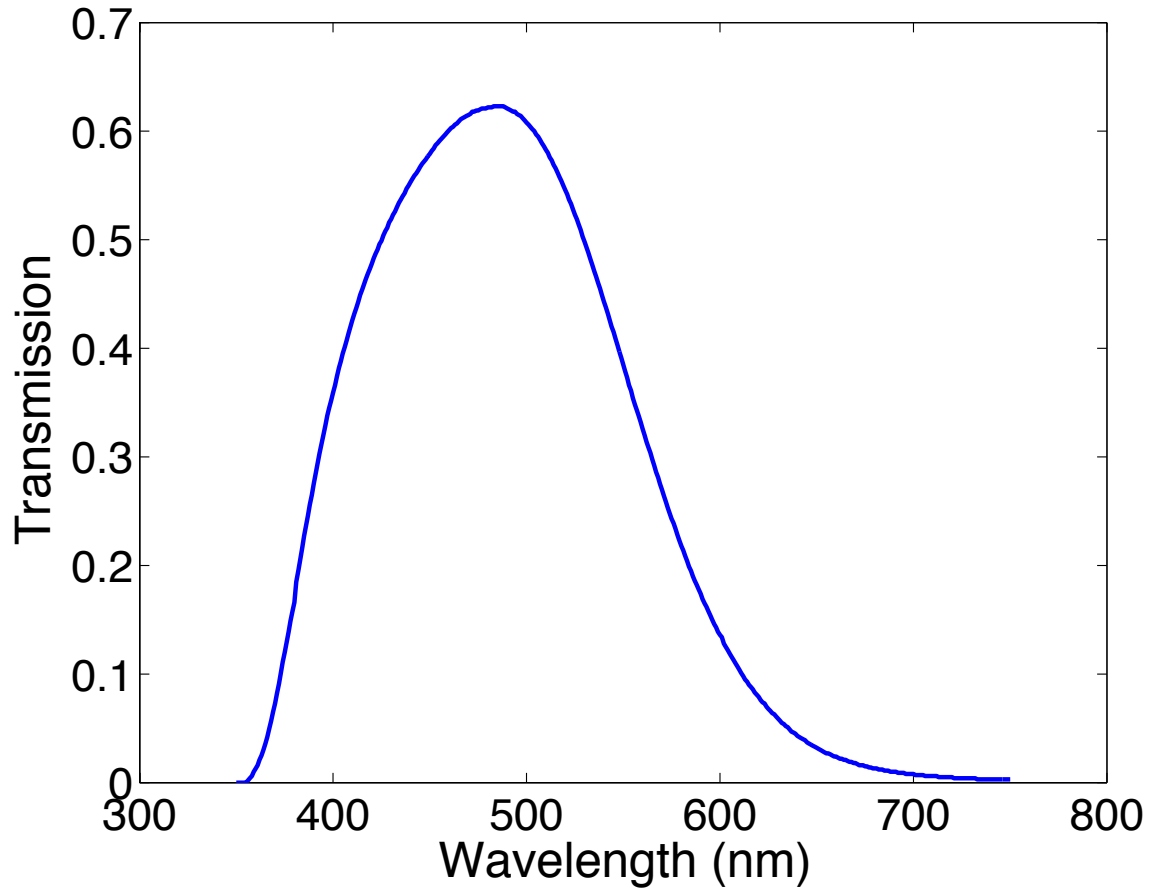
Fig. 2.4. BG glass filter transmission curve

To further characterize the detectors, independent blackbody calibrations were performed. The D70 was calibrated using a high temperature (1100 – 1160 °C) blackbody source available at Sandia national laboratories. Both the D90 and D300s were calibrated against a blackbody source (Pegasus R, Model 970) at temperatures ranging from 800 – 1200 °C, in increments of 50 °C, and a calibrated tungsten lamp (Gamma Scientific, RS-10D) with known spectral radiance and apparent temperature of 2756 K. Data from these calibrations are presented in the next section.

2.2.3   Color-ratio pyrometry background

The intensity of radiation emitted by a material at wavelength λ, is dependent on the material's emissivity $\varepsilon(\lambda)$ and the temperature T according to Planck's law as expressed by Eq. (2.2.1):

$$I(\lambda,T) = \varepsilon(\lambda)\frac{2\pi hc^2}{\lambda^5\left(e^{hc/\lambda kT} - 1\right)} \qquad (2.2.1)$$

where c is the speed of light, h is Planck's constant, and k is the Boltzmann constant. The measured signal, S_F, detected through a color filter in a time interval τ is the intensity of radiation integrated over the detection wavelengths:

$$S_F = \left(2\pi hc^2\right)\tau \int_{\lambda_1}^{\lambda_2} \frac{\varepsilon(\lambda)\eta(\lambda)}{\lambda^5\left(e^{hc/\lambda kT} - 1\right)}d\lambda \qquad (2.2.2)$$

where $\eta(\lambda)$ accounts for the efficiency of the detector, the combined lens and filter

14

transmittance, as well as a geometric factor. λ_1 and λ_2 are the low and high limits of the filter bandwidth, which are approximately 400 nm and 700 nm. In conventional color-ratio pyrometry applications, the filter bandwidths at two central wavelengths are selected to be narrow compared with the spacing between two filters. This approach, outlined by Levendis *et al.* [Levendis 1992], takes a signal ratio at two spectral bands, and uses the finite filter widths and mean multipliers for each filter at the central wavelengths to simplify Eq. (2.2.2). The result is an implicit temperature equation that can be solved iteratively for a measured signal ratio using a calibration that characterizes the detection system. In this approach, the filters are described only by a single mean wavelength and a spectral width.

The assumption of narrowband detection filters used to derive the implicit temperature equation, however, is not valid for the CFAs on the color digital cameras considered here (see Fig. 2.3).

Clearly the filter functions are broad and relatively complex and thus the Planck function varies significantly within each of the three spectral detection windows of the CFA. In previous work [Boslough 1989; Anselmitamburini 1995; Connelly 2005] it was shown that the effect of the variation in the Planck function over a broad spectral window could be overcome by calculating a new effective filter wavelength for each iteration of the temperature equation. Alternatively, it is possible to evaluate Eq. (2.2.2) without making approximations of the filter profiles. In this approach, the signal ratio is derived directly from Eq. (2.2.2) to be

$$\frac{S_{F_1}}{S_{F_2}} = \frac{\int \eta_{F_1}(\lambda) \frac{\varepsilon(\lambda)}{\lambda^5}[\exp(hc/\lambda kT)-1]^{-1} d\lambda}{\int \eta_{F_2}(\lambda) \frac{\varepsilon(\lambda)}{\lambda^5}[\exp(hc/\lambda kT)-1]^{-1} d\lambda} \qquad (2.2.3)$$

for filters F_1 and F_2, where $\eta_{F_1}(\lambda)$ and $\eta_{F_2}(\lambda)$ are the respective transmission efficiencies for each color channel as a function of wavelength. The ratio can be calculated by evaluating the integrals in Eq. (2.2.3) numerically based on the characteristics of the detection system for a range of input temperatures. Assuming the signal ratio to be single valued over the temperature range of interest, this lookup table can be used to determine temperatures based on the ratio of two colors. A camera with three separate filters will provide three ratios, all of which can be used in determining the most likely final temperature.

The color ratio *vs* temperature lookup tables are calculated and shown in Fig. 2.5, Fig. 2.6 and Fig. 2.7 for D70, D90 and D300s respectively. Solid lines correspond to the ratios calculated for a blackbody source via Eq. (2.2.3) using the measured camera response shown in Fig. 2.3. Individual asterisks show the results of the blackbody calibration, and dashed lines show the expected signal ratio for soot. A high temperature blackbody source was used to calibrate the D70, and a medium temperature blackbody source and a tungsten lamp were used together to calibrate the D90 and D300s. The agreement between the measured blackbody ratios and the ratios calculated from the measured spectral curves are improved by small modifications (<5%) to the RGB scaling parameters and these are included in the ratios shown in Fig. 2.5 through Fig. 2.7 as well as in the response shown in Fig. 2.3. To generate the soot lookup table, the emissivity of

16

soot is assumed to vary as $\lambda^{-1.38}$. This is based on the wavelength dependence of the refractive index measured by Chang and Charalampopoulos [Chang 1990b] together with the expression for emissivity as a function of refractive index from [De Iuliis 1998a]. Such wavelength dependence is the so-called dispersion exponent. It will be discussed in detail in Chapter 5 where spatially resolved 2-D measurements will be presented. A constant value of 1.38 is now assumed without distracting from the main purpose of this chapter. The emissivity of the SiC fiber is normally assumed to not vary with wavelength in the visible region of the spectrum ($\varepsilon = 0.88$) [Maun 2007]. Under such a greybody assumption, the emissivity terms in Eq. (2.2.3) cancel and the blackbody lookup table can be used. The validity of the greybody assumption of the SiC fibers is examined by measuring its spectral emissivity and performing aging tests; more detailed information is given in Chapter 3 along with uncertainty and accuracy assessment.
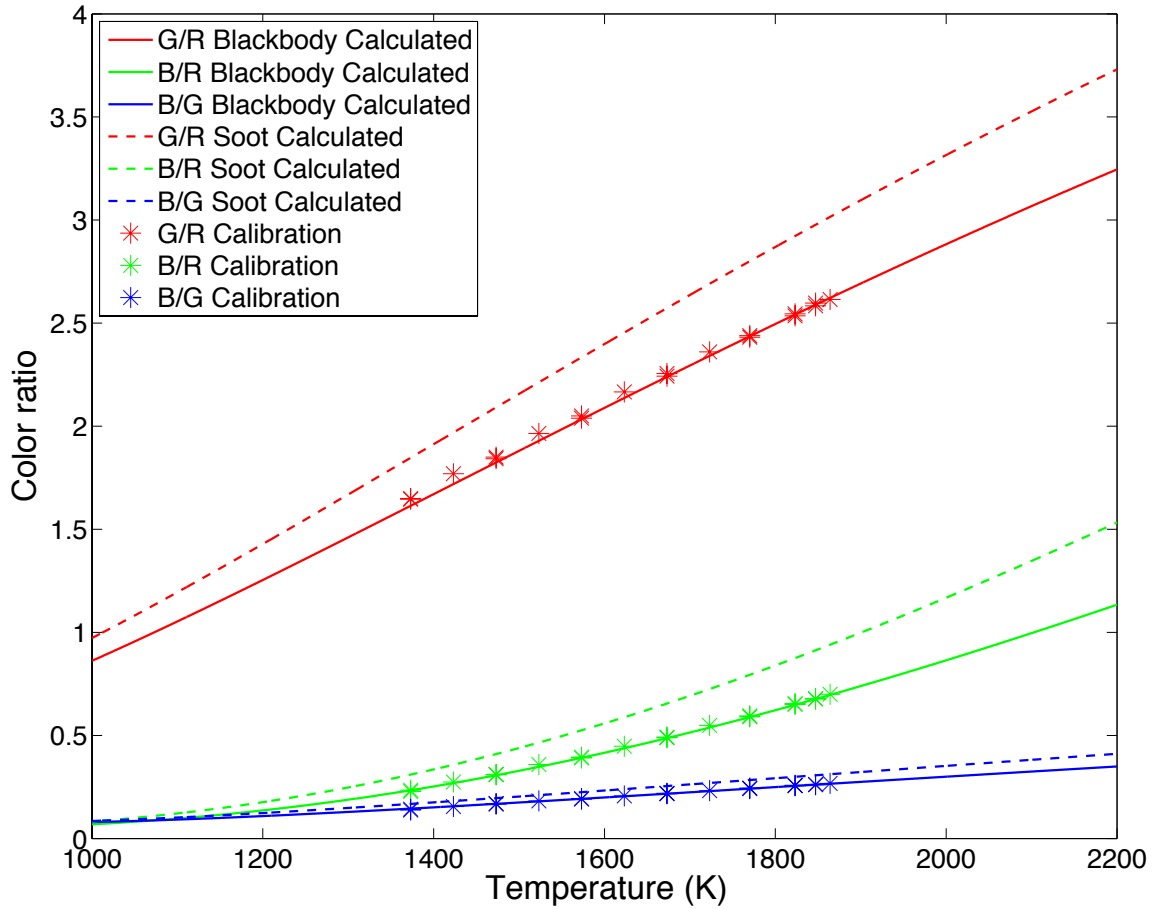
Fig. 2.5. D70 signal ratios vs. temperature lookup table for a blackbody or greybody (solid lines) and soot (dashed lines), validated by an independent blackbody calibration. Individual dots show the results of the blackbody calibration.
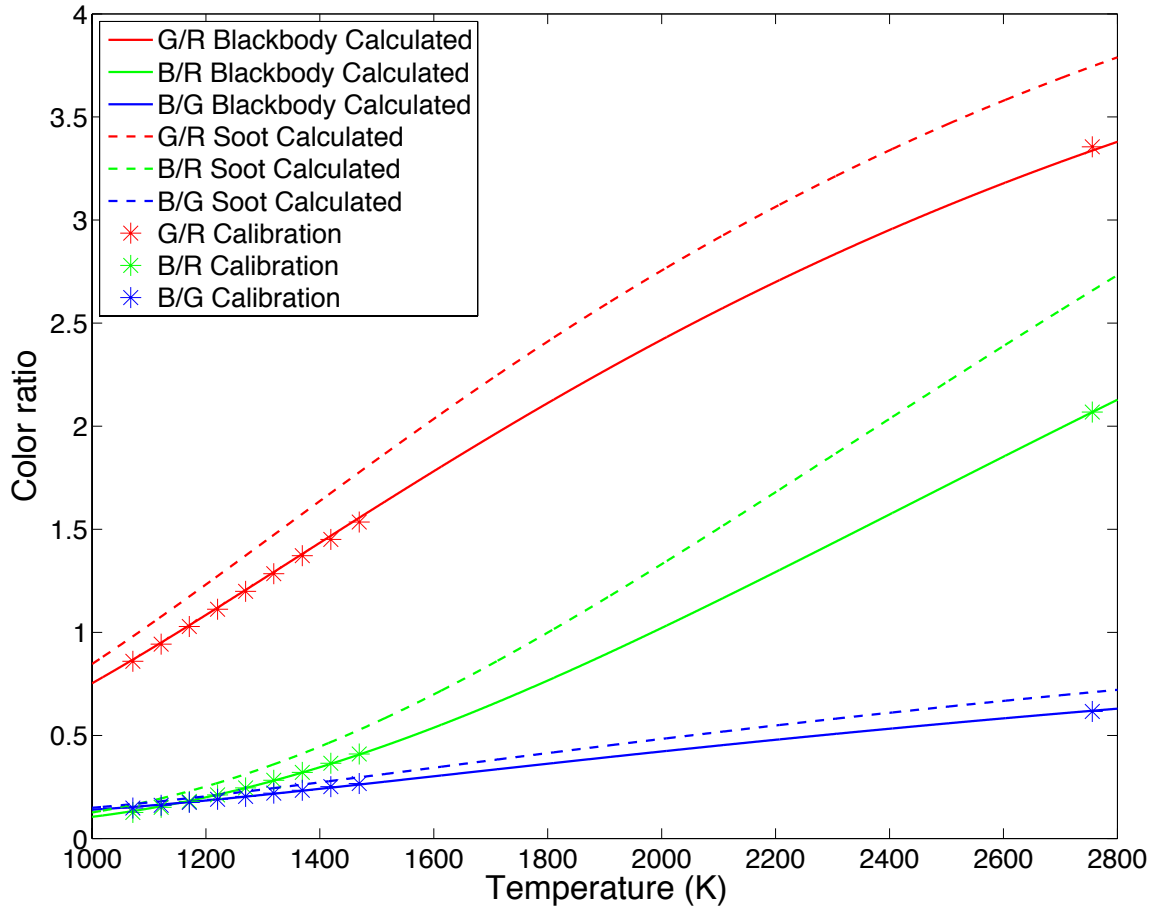
Fig. 2.6. D90 signal ratios vs. temperature lookup table for a blackbody or greybody (solid lines) and soot (dashed lines), validated by an independent blackbody calibration. Individual dots show the results of the blackbody calibration.
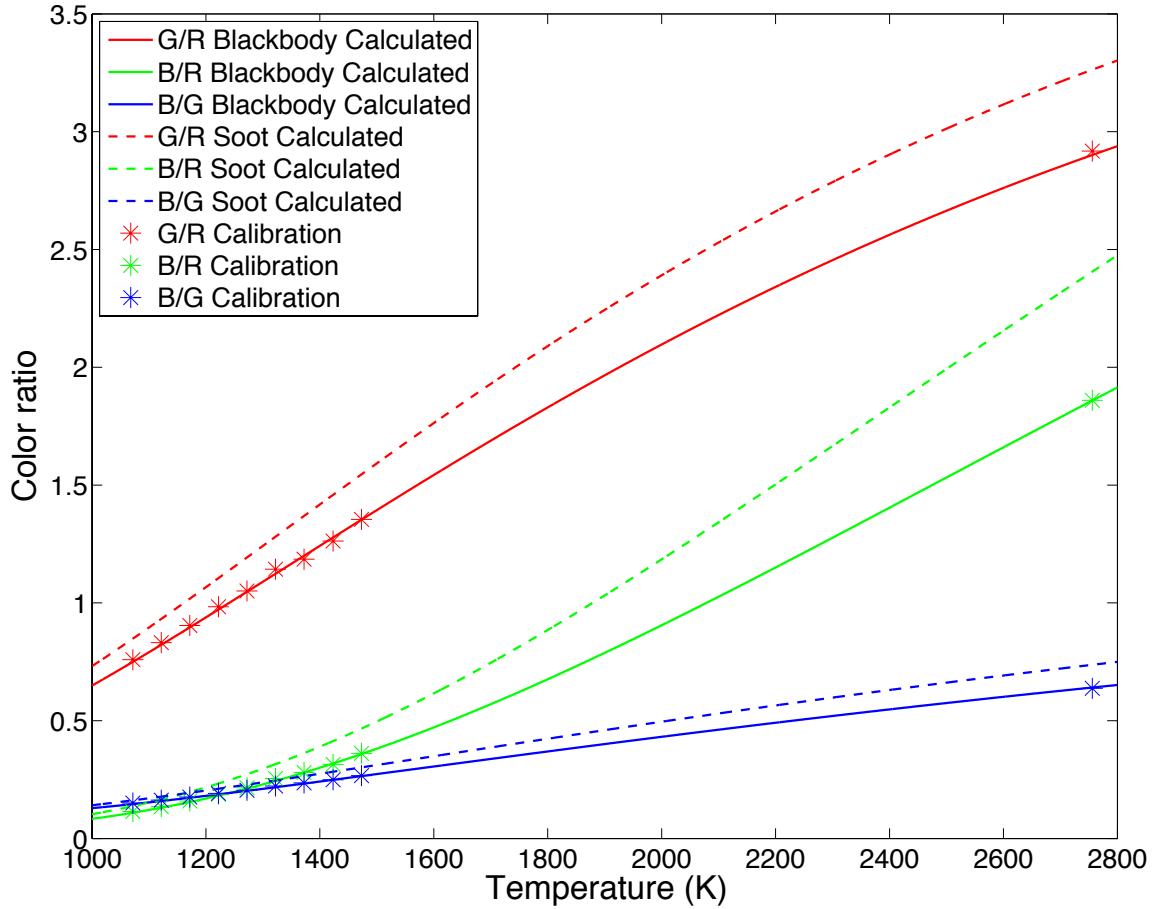
Fig. 2.7. D300s signal ratios vs. temperature lookup table for a blackbody or greybody (solid lines) and soot (dashed lines), validated by an independent blackbody calibration. Individual dots show the results of the blackbody calibration.

2.2.4 Thin-filament measurement of gas temperature

Following the detector characterization, gas temperatures were measured in nonsooting regions of sooting, axisymmetric, laminar ethylene diffusion flames, with varying degrees of fuel dilution by nitrogen. The burner used in this study is the Yale standard coflow laminar diffusion flame burner as shown in Fig. 2.8. The burner consists of a 0.4 cm inner diameter vertical fuel tube, surrounded by a 7.4 cm coflow.
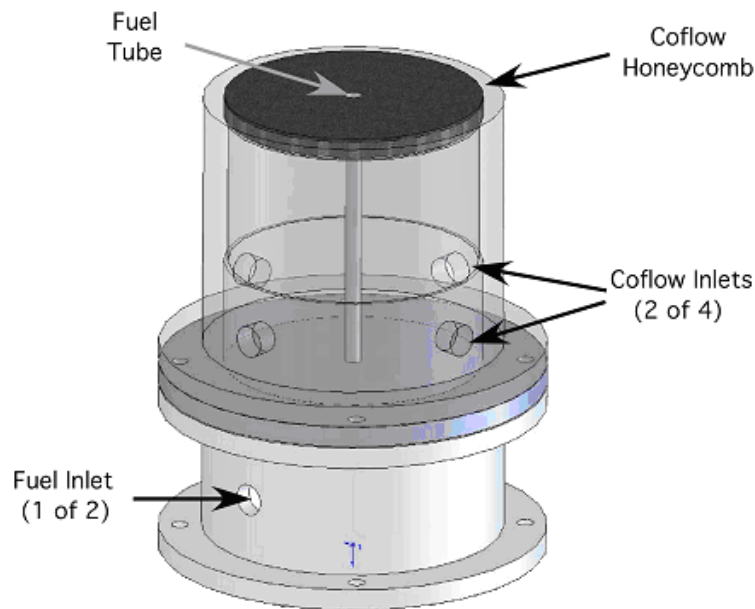
Fig. 2.8. Burner configuration

Flames with different fuel mixtures were studied with ethylene concentrations of 32%, 40%, 60%, and 80%, by volume. For all flames, the fuel velocity at the burner surface had a parabolic profile and the air coflow was plug flow produced by the honeycomb on top, both with an average velocity of 35 cm/s. This configuration has been studied previously as part of an ongoing experimental and computational collaboration

[Smooke 2005]. A description of the computations used here for the temperature and soot volume fraction comparisons is described in Section 2.2.6 for completeness.

The flames were imaged through the BG glass filter at f/16 with an 85 mm focal length lens, offset from the camera body with an extension ring. The lens configuration was chosen to approximate parallel ray collection, which is a necessary assumption for the Abel inversion required for the soot pyrometry described in the next section [Dasch 1992; Walsh 2000a]. The filament, with a length of ~ 7 cm and diameter of 15 μm as measured with an optical microscope, was attached with tape to metal rods and placed horizontally in the flame. Measurements were made at 30.0 mm, 39.0 mm, 59.6 mm and 83.9 mm above the center of the burner for the 32%, 40%, 60% and 80% flames, respectively. These locations were well beyond the sooty region to avoid interference from soot emission.

For each filament temperature measurement, two NEF images, with and without the filament above the flame, were obtained. The one without the filament served as background and was subtracted pixel by pixel. With a perfect imaging system, the image of the fiber on the detector would be smaller than the width of one pixel (by factors of 4.4 and 3.2 for the D70 and D90, respectively) but aberrations in the imaging system resulted in the fiber image being spread over several pixels. A region surrounding the filament is selected to include all RGB pixels containing filament radiation and the intensities are integrated along the axial direction in this region. Dividing the RGB integrated intensities by each other yielded three ratios, and three consistent temperatures were obtained from the ratios by applying the appropriate blackbody lookup table (Fig. 2.5 - Fig. 2.7).

The maximum variation of the temperatures obtained from the three ratios is

~ 20 K, while the average temperature is almost the same with the temperature lookup by the B/R ratio, with a maximum difference around 3 K. Fig. 2.9 shows the filament temperatures above each of the four flames as measured by the D90 camera. The fluctuations along the profile come from the imperfection of the filament and variation of pixels. Because of the rapid drop-off in intensity at lower temperatures, filament temperatures lower than ~ 1400 K became dominated by noise. It should be noted that when a new filament was positioned above the flame, the RGB intensity and derived temperatures were not initially stable and should be aged for at least 10 minutes before using. A more comprehensive and quantitative examination of the fiber aging behavior is available in Chapter 3.

The filament is heated by convective heat transfer from the surrounding hot gases and cooled by radiation transfer with the ambient environment and axial heat conduction along the filament. Therefore the filament temperature is always lower than the gas phase temperature and a correction process is needed to obtain gas temperature. The corrections are dependent on gas properties, velocity, composition, and temperature. The computations for the four N_2 diluted flames showed that N_2 occupies more than 70% volume downstream at the filament position. Therefore, gas properties used here can be based on pure N_2, for simplicity, without losing too much accuracy. The correction procedure followed the analysis of Maun et $al.$ [Maun 2007]. A more in-depth discussion on the radiation correction is available in Chapter 3.
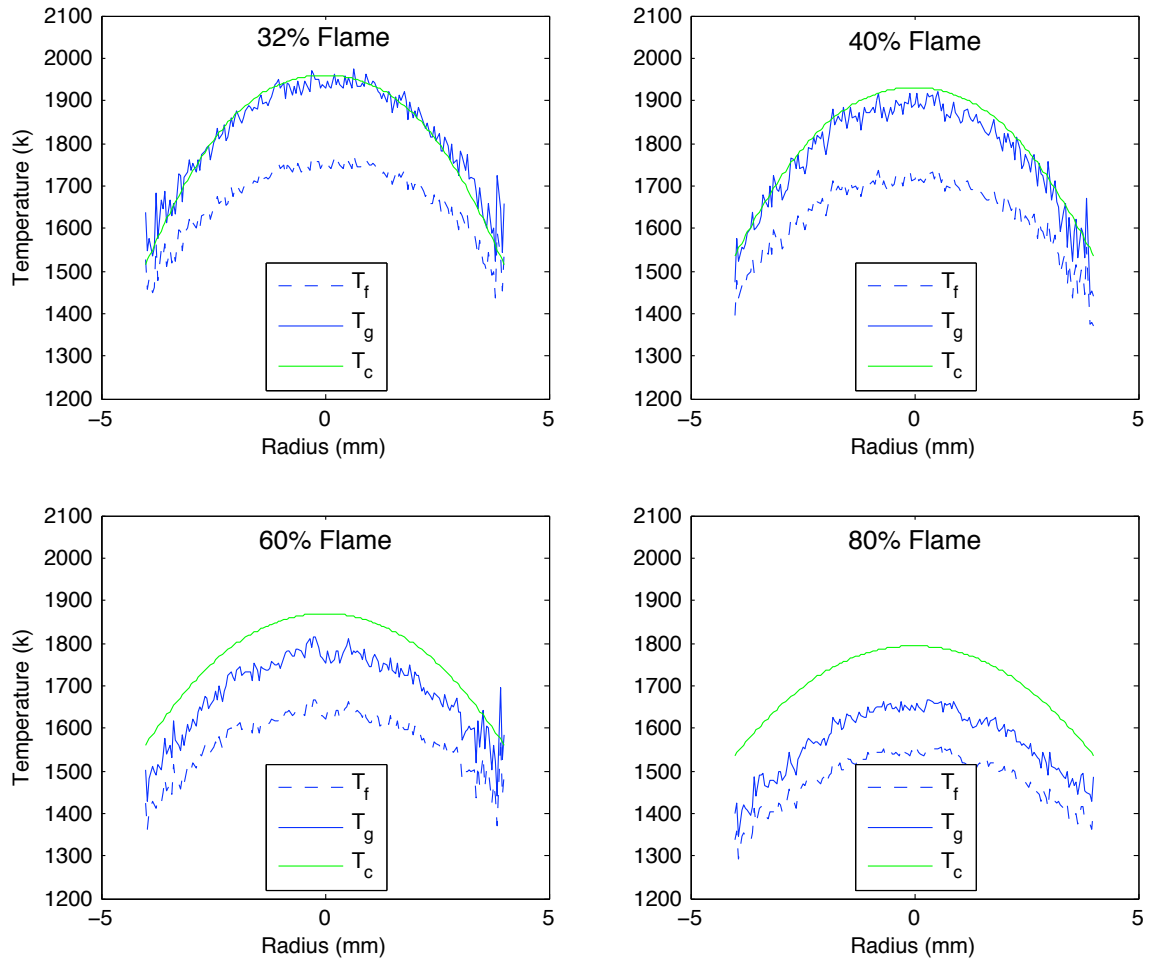
Fig. 2.9. Filament temperature T_f, filament-derived gas temperature T_g (both measured with the D90) and calculated gas temperature T_c from four nitrogen-diluted ethylene flames. Measurements were made downstream of the luminous region of the flame at 30.0, 39.0, 59.6 and 83.9 mm above the center of the burner for the 32%, 40%, 60% and 80% flames, respectively.

As shown in Fig. 2.9, T_f is the filament temperature, T_g is the derived gas phase temperature while T_c is the computational result. The derived gas temperature is in good agreement with the computational results for the 32% and 40% flames. For the higher fuel concentration flames, the computed temperature is seen to be higher than the measured temperatures. This difference may be attributed to less radiation loss in the computations, since the computational results predict a lower soot volume fraction than is measured.

2.2.5 Soot temperature and volume fraction in four sooting laminar flames

Soot temperature measurements were performed in the same setup as the filament temperature measurement. Each flame image was separated into three RGB images and then converted to radial profiles using an Abel inversion. Prior to the Abel inversion, the image of the full flame must be divided into a half image, with the symmetry axis on one side of the half image. Best results were obtained by considering each radial slice of the image (i.e., one row of pixels), finding the centroid of the row, and folding the intensities about that centroid. This makes use of both halves of the image, resulting in less noise in the final Abel-inverted profile, and eliminates any need for manual cropping of the image. Dividing the radial profiles by each other to determine the measured signal ratios and applying the soot lookup table gives three soot temperature profiles, with a maximum variation of ~ 30 K. The final temperature is an average of the three. Fig. 2.10 (top) shows the measured soot temperatures from each of the flames obtained with the D90. As might be expected, the peak temperature decreases as the fuel concentration increases, due to increased soot loading and the resultant radiative heat loss. Since soot pyrometry can only measure temperature where soot is present, the calculated temperature profiles

shown in Fig. 2.10 (bottom) have been cropped to show only those regions where soot was calculated to be nonzero. While the computational model gives a somewhat different prediction of the sooting region, (which in turn results in a different shape of the cropped temperature profile) the same general trends are seen in both measurement and computation, with peak temperatures decreasing as the soot loading increases.
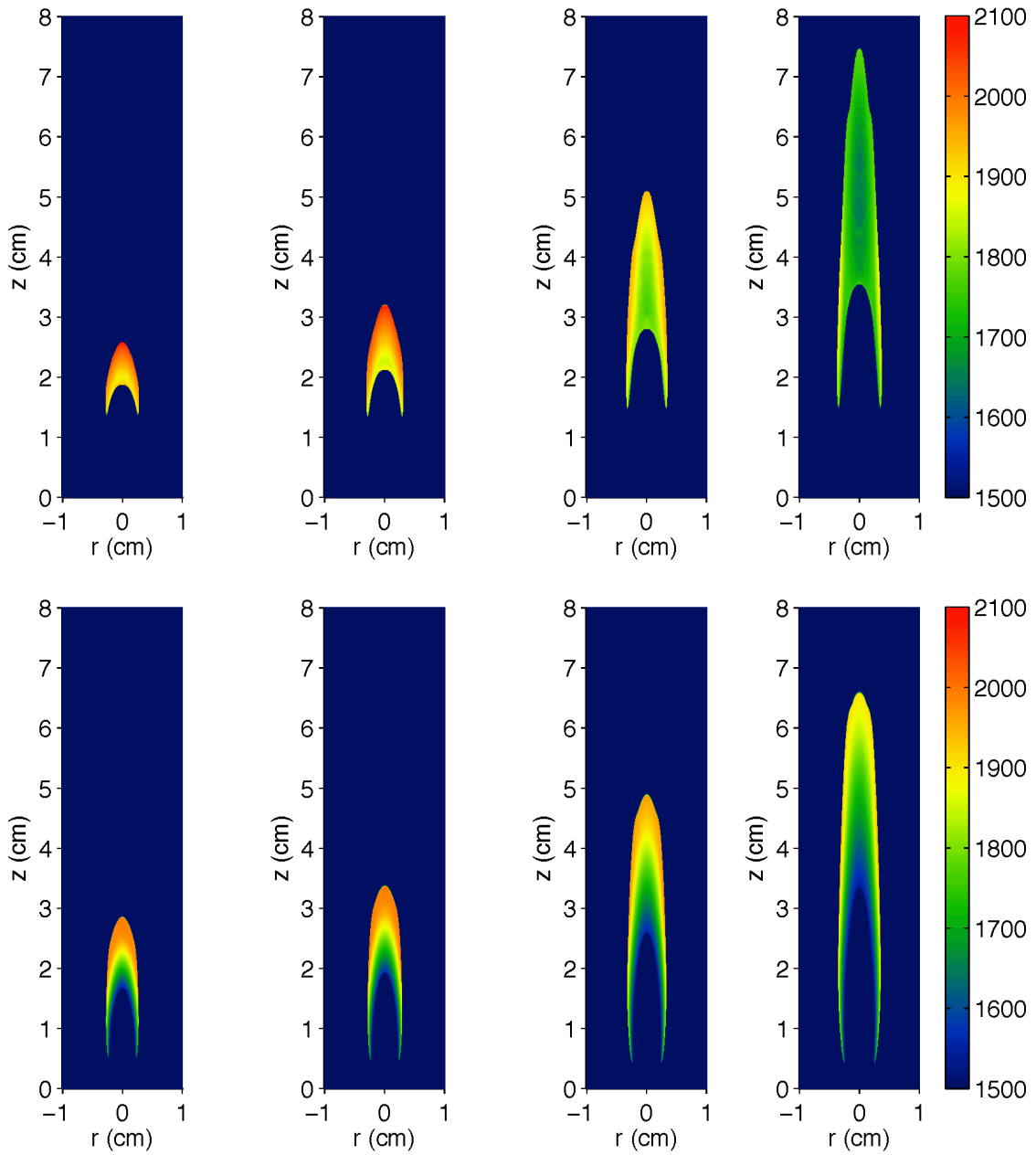
Fig. 2.10. Measured (top) and calculated (bottom) soot temperatures from four nitrogen-diluted ethylene flames with fuel concentrations (from left to right) of 32%, 40%, 60% and 80% C_2H_4.

Once the soot temperature is known, the soot volume fraction, f_v, can be determined if an absolute intensity calibration is available for the specific optical configuration used. Following the formulation of Cignoli, *et al.* [Cignoli 2001] this can be expressed as

$$f_v = -\frac{\lambda_S}{K_{ext}L}\ln\left\{1 - \varepsilon_L(\lambda,T_L)\frac{\tau_S}{\tau_L}\frac{S_{S\lambda}}{S_{L\lambda}} \times \exp\left[-\frac{hc}{k\lambda_S}\left(\frac{1}{T_L}-\frac{1}{T_S}\right)\right]\right\} \qquad (2.2.4)$$

where λ_S is the effective filter wavelength at the soot temperature, K_{ext} is the dimensionless extinction coefficient, L is the absorption length (the dimension of one binned pixel), $\varepsilon(\lambda,T_L)$ is the emissivity of the calibration source, and τ, S_λ, T are detector parameters, signal intensity and temperature, respectively, with subscripts L and S corresponding to the calibrated light source and soot, respectively. K_{ext} was taken as 8.6 here, which is consistent with values given by Krishnan *et al.*, [Krishnan 2000] and matches the value used in the LII experiment that the soot volume fraction results are compared against [Smooke 2005]. The effective filter wavelength, λ_S, is the wavelength at the maximum value of the product of the camera filter response (see Fig. 2.3) and the Planck blackbody intensity evaluated at the particular soot temperature.

A blackbody calibration source or other calibrated light source can be used for calibration, as long as the optical configuration is not changed. A more convenient source of absolute intensity calibration, however, is available from the image of the filament discussed above. As long as the emissivity is known, this measurement provides a temperature (higher than that available from common blackbody sources) and an absolute RGB light intensity correlation. This has the advantage of being simple to implement,

since the filament and soot measurements are performed in the same experimental configurations and the geometric factors therefore cancel. The ratio of optical parameters $\dfrac{\tau_S}{\tau_L}$ simply accounts for any difference in exposure times and the ratio of the length imaged onto a pixel to the filament diameter. It should be noted that thermal radiation is highly dependent on temperature. Therefore the uncertainty of the measured SiC fiber temperature will be amplified in the uncertainty of calculated spectral radiance and hence the soot volume fraction via Eq. (2.2.4). An effective method to reduce such uncertainty is to minimize the uncertainty of the calibration source temperature. This gave birth to the idea of using S-type thermocouples, a standard for measuring temperature, as a calibration source for highly accurate absolute light calibration. The method will be discussed in Section 2.3.

Fig. 2.11 (top) shows the soot volume fraction measurements obtained in the four flames using the D90 and Fig. 2.11 (bottom) shows the soot volume fraction measured in the same flames using laser-induced incandescence (LII) and reported previously [Smooke 2005]. Agreement between the two measurement techniques is very good.
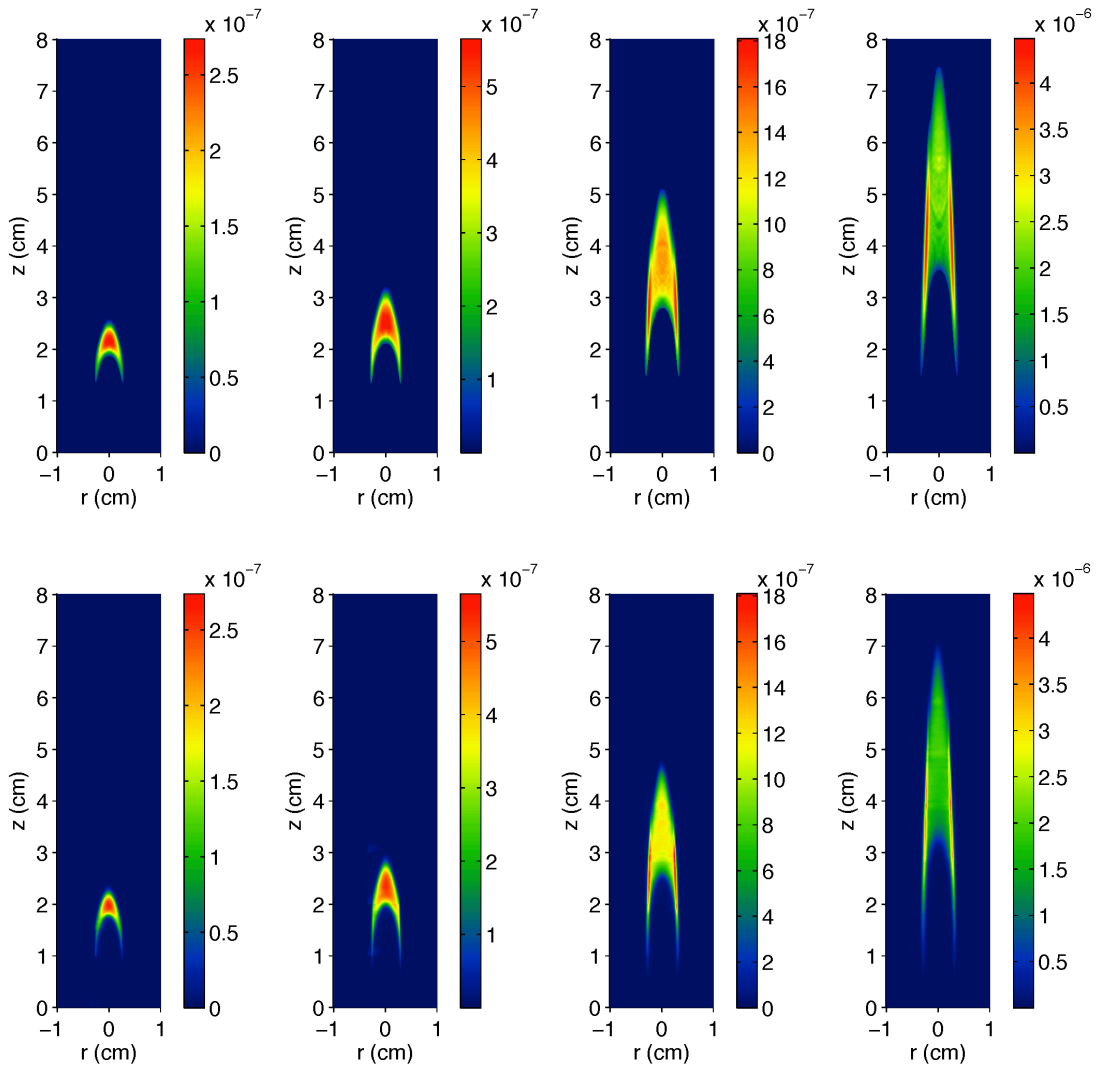
Fig. 2.11. Soot volume fraction measured using pyrometry (top) and LII (bottom) from four nitrogen-diluted ethylene flames with fuel concentrations (from left to right) of 32%, 40%, 60% and 80% C_2H_4.

2.2.6   Computational modeling

The numerical simulation was performed by Professor Smooke and his group. The model used here is similar to those employed in the previous works (see, for example, [Bennett 2000]). Specifically, the gaseous mixture is assumed to be Newtonian, and the diffusion of each species is approximated as Fickian. The flow's small Mach number implies that pressure P can be approximated as being independent of location in the flame, and mixture density ρ can be directly obtained from the ideal gas law. To evaluate the divergence of the net radiative flux, the model includes an optically thin radiation submodel [Edwards 1976; Hall 1993; Hall 1994] with three radiating species (H_2O, CO, and CO_2).

The soot temperature and volume fraction were predicted using a sectional representation as discussed in greater detail in [Gelbard 1980a; Gelbard 1980b; Hall 1997] and has been employed in a number of flame studies (e.g., [McEnally 1998; Smooke 1999; Smooke 2004; Smooke 2005; Dworkin 2009]). It assumes that soot particles can be approximated as carbon spheres and that they exist in the free molecular limit (i.e., the mean free path of the gaseous mixture is much larger than the largest soot spheroid). The approach specifies a minimum and maximum particle mass and divides the spheroid sizes logarithmically into N_{sec} bins or sections. A further assumption is that within a given section, spheroids of varying diameter do not exhibit vastly differing aerosol dynamical qualities. This assumption holds as long as N_{sec} is sufficiently large. In the computations presented herein, a total of 30 soot sections were employed. The surface growth model used in the numerical simulations was based on the premixed flame data of Harris-Weiner [Harris 1983] where we assumed an activation energy of E_s = 31.8

31

kcal/mole [Hura 1989]. However, unlike in previous studies, the nominal Arrhenius factor was not increased by a factor of two (see also [McEnally 1998; Smooke 1999; Smooke 2004; Smooke 2005]).

The chemical mechanism was derived from one of the more comprehensive and well-validated sets available for ethylene [Sun 1996]. The resultant mechanism contains 476 reactions and 66 chemical species. The result is a model that requires a total of 100 dependent variables to be solved at each grid point. The system is closed with the ideal gas law and appropriate boundary conditions are applied on each side of the computational domain. All thermodynamic, chemical, and transport properties are evaluated by the CHEMKIN [Kee 1980; Kee 1987] and TRANSPORT [Kee 1983; Kee 1986] subroutine libraries, parts of which were optimized for greater speed [Giovangigli 1988]. The sectional thermophoretic velocities in the free molecule regime are given in [Hall 1997] as are the sectional diffusion velocities written with a mass-weighted mean diffusion coefficient for each size class. The governing conservation equations are solved on a two-dimensional mesh by combining a Newton-based steady-state and a time-dependent solution method [Smooke 2004]. A time-dependent solution is first obtained on a coarse grid and then grid points are inserted adaptively to increase the resolution in regions of high spatial activity. Computations were performed on a 3.0 GHz Intel Xeon processor system with 8 cores per node and 16 GB RAM per node.

2.3 Absolute light calibration

2.3.1 Introduction

In almost all optical measurements, the directly measured signals are normally expressed as voltage readings or detector counts. They are useful to provide relative

intensity information, for example higher signals normally correspond to greater emission. However, absolute information such as number of photons is not readily available. The measured signal is not only determined by the emitted radiation, it is also affected by many other parameters. For example, the collection angle of the optical systems determines how much light is collected over the 4π solid angle; the optical transmission of the optics and atmosphere determines how much light is transmitted along the optical path from the light source to the detector; the spectral response of the detection system accounts for the quantum efficiency of the detector and A/D conversion. Absolute light calibration can be used to quantify these parameters and establish the correlation between measured signals and the quantitative radiation, i.e., number of photons. The calibration should be performed in the same setup with a light source of known spectral radiance. By measuring the signal from the known light source, the calibration of the measured signal and its corresponding known spectral radiance can be established. Such calibration can be used to trace an unknown spectral radiance from their corresponding signals in subsequent measurements. The spectral radiance often relates to physical quantities of diagnostic interest; therefore by quantifying the spectral radiance, absolute number density of certain species can be determined. For example, absolute light calibration is desired in determining the absolute concentration of species through fluorescence or chemiluminescence, or absolute soot volume fraction.

Traditional calibration methods normally employ, for example, Rayleigh scattering and commercially available blackbody furnaces or calibrated tungsten lamps. The Rayleigh scattering calibration requires a relatively complex procedure; blackbody furnaces normally do not give enough signal in the blue range of light due to their low

operating temperature; and calibrated blackbody furnaces and tungsten lamps are relatively expensive and require re-calibration after a certain time of operation. More importantly, restrictions apply when the calibration needs to be simple and robust, for example, when calibration is needed in a closed volume as in the case of the SLICE project that will be discussed in Chapter 4. Briefly, the SLICE jet flame to be measured is stabilized in a rectangular duct, where there is no optical access for a laser beam and the volume is so small that no commercial calibration sources such as a tungsten-halogen lamp could fit. A low-cost, simple and high-accuracy method to do absolute light calibration using S-type thermocouples is developed [Ma 2013] to enable calibration in small volumes. The details of this approach are described in Section 2.3.3 following a brief introduction of more traditional approaches such as Rayleigh scattering based calibration and blackbody furnace/tungsten lamp based calibration.

2.3.2   Calibration using Rayleigh scattering

Rayleigh scattering is not only useful in temperature measurement, but it has also been proven to be a useful approach to perform absolute light calibration [Luque 1996a; Luque 1996b]. Rayleigh scattering is an elastic scattering process used to describe scattering from molecules, small particles and clusters that are much smaller than the wavelength of the illumination light. The scattered light has the same central wavelength as the probing laser beam, and the intensity can be expressed by Eq. (2.3.1).

$$S_{scatt} = nV\left(\frac{\partial \sigma}{\partial \Omega}\right)\Omega \varepsilon \eta I \quad (2.3.1)$$

where n is the number density of scatterers, V is the sample volume, $\dfrac{\partial \sigma}{\partial \Omega}$ is the Rayleigh

34

cross-section and I is the laser fluence. The parameters Ω, ε and η specify the collection angle, efficiency of the collection optics and the response of the detection system respectively. The number density n can be correlated to temperature T through ideal gas law, where $n = P/RT$, which provides the basis for temperature measurement using Rayleigh scattering. For absolute light calibration, it is desired to determine the product $\Omega\varepsilon\eta$ that is the so-called optical constant and is setup specific. The calibration must be performed under well-known conditions and the laser fluence I have to be accurately measured. The calibration should be performed at known temperature and pressure. The calibration gas can be nitrogen or other gases with well-known Rayleigh cross-section. The sample volume should also be measured by determining the spatial projection. In Section 2.3.3, a comparison between calibration using Rayleigh scattering and thermocouple luminosity will be shown.

2.3.3 Calibration using a standard blackbody furnace and a tungsten lamp

Absolute light calibration can be performed by multiple methods. A common way is to use a blackbody furnace or tungsten lamp with known spectral radiance. Such instruments are mature products that are commercially available. A blackbody furnace consists of a cavity emitter with high emissivity of ~ 0.99 or greater and an electronically stabilized furnace. The emitter is embedded in the furnace and is heated to the desired temperature by the heating elements. The spectral radiance output can be calculated using the blackbody radiation law with errors of ~ 1% or smaller. Depending on the design of the furnace, the high temperature range is normally 800 – 1450 °C while the medium and low temperature ranges are normally 200 – 1050 °C and 50 – 450 °C respectively. Sophisticated electronics are designed to stabilize the temperature and ± 0.5 K or better

temperature fluctuation is typically achieved. However, the time required to heat up and stabilize the furnace to the desired temperature is rather long and normally ranges from 30 minutes to 2 hours. The current market price of such equipment is beyond $10 K. While performing experiments in a small chamber, it is very likely that the blackbody furnace is too large to fit, prohibiting calibration in such experiments. Given the relatively low temperature range, blackbody furnaces provide more signals at longer wavelengths such as the near-IR than at shorter wavelengths such as the visible blue light. Another commonly used calibration source is the tungsten lamp. The tungsten filament acts as an electronic resistor and is heated by the Joule effect. The spectral radiance output is calibrated at a particular lamp current that is highly regulated by a constant current power supply to ensure repeatability. The tungsten filament is housed in a bulb filled with inert gas to prevent tungsten evaporation. For normally used tungsten-halogen calibration lamps, a small amount of an active halogen gas such as Bromine is also added to reduce the amount of tungsten that plates the interior wall of the lamp . Such approaches are meant to increase the lifetime of the lamp. Nevertheless, an annual calibration for the calibrated lamps is often recommended by the vendors. Compared to blackbody furnaces, tungsten-halogen lamps operate at a much higher apparent temperature of ~ 2700 K, thus, providing more signals at shorter wavelengths. While the temperature of blackbody furnaces is tunable within the working range, tungsten-halogen lamps only work at a particular calibrated current. The cost of the calibrated lamp is also high and is normally above $5 K at the current market price. The size is smaller compared to a blackbody furnace, however it may be still too bulky to fit in certain experimental setups.

2.3.4   Calibration using S-type thermocouples

A low-cost, simple and high-accuracy method to do absolute light calibration using S-type thermocouples has been developed [Ma 2013]. S-type thermocouples, a standard for temperature measurement, are made by joining platinum (Pt) and platinum–10% rhodium (Pt–10%Rh) wire. The temperature of the welded junction is correlated to voltage produced by the Seebeck effect. The correlation has been calibrated into a standard Thermocouple Database and fitted to a polynomial expression that provides high accuracy in a specified temperature range.

In the work described here, a flame-heated, glowing S-type thermocouple is treated as the light source, for which the source temperature can be readily and accurately obtained from the thermocouple reading. The thermocouple is also proven to be a stable light source by inspecting its spectral radiance over more than one hour of aging in a flame. The stability over time provides the basis for the Pt and Pt–10% Rh wire to serve as a transferrable calibration source. Specifically, if the wire diameter, temperature, and spectral emissivity are known, the spectral radiance of the wires can be readily calculated by Planck's law. The spectral emissivity of Pt was previously measured, but mostly in the infrared region. In this work, measurements of spectral emissivities of Pt and Pt–10% Rh were extended to the visible range. Measurements were conducted by two independent methods using a spectrometer and four interference filters.

The experimental setup, emissivity measurement methodology, and measurement consistency will be described in the following sections. The absolute light calibration method was used to determine quantitatively the number density of CH* in a lifted, coflow laminar diffusion flame of methane and the soot volume fraction in coflow

37

laminar diffusion flames of ethylene with varying amounts of nitrogen dilution. The results will be compared with previous measurements.

2.3.4.1 Experimental setup

The schematic of the setup used to measure the spectral emissivities of Pt and Pt-10% Rh is shown in Fig. 2.12. A straight section of the thermocouple wire was mounted horizontally above a stable flat premixed CH_4/air flame (5 cm in diameter) with equivalence ratio of 0.9. The glowing thermocouple then becomes a line emitter as shown in Fig. 2.13. The flat flame temperature distribution is uniform in the 1 cm central region. The incandescence of the heated thermocouple wire was imaged by an 85 mm focal length Canon camera lens into the horizontal slit of a spectrometer (Jarrell-Ash MonoSpec 27) with a 150 groove/mm grating. The f-number of the lens was matched to that of the spectrometer to reduce stray light. The width of the slit is 550 μm, which is just wide enough to pass all the thermocouple incandescence into the spectrometer without clipping the signal. A ground glass diffuser (DG20-1500) was aligned at the focal plane of the spectrometer on which an image of the spectrum was formed. The image was then demagnified and imaged onto an interline CCD camera (Cooke SensiCam with superVGA sensor) to capture wavelengths from 400 - 700 nm while filling the entire image sensor to maximize the spectral resolution. The wavelength was calibrated by a mercury-vapor lamp. The horizontal axis and vertical axis of the two-dimensional image retained the spatial and spectral information respectively.
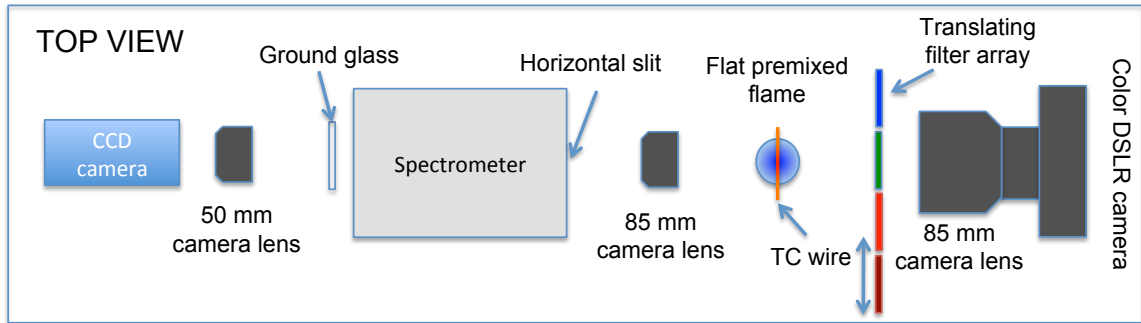
Fig. 2.12. Experimental setup for S-type thermocouple spectral emissivity measurements

On the other side, the incandescence was filtered by one of four 10 nm narrowband interference filters with central wavelengths at 431, 532, 600 and 700 nm, and then imaged by a DSLR camera (Nikon D300s). The interference filters were mounted on a stepper motor for fast and automatic transition from one to another. The D300s utilizes a CMOS sensor (23.6 mm × 15.8 mm) with 13.1 million pixels (2848 x 4288). This camera has been fully characterized, as described in Section 2.2.2. For the spectral emissivity measurement, the camera is used as a monochromatic camera. The acquired incandescent thermocouple wire raw images were converted to grayscale images by summing up red, green and blue signals in post-processing. The absolute spectral response of the spectrometer/CCD system and the interference filter/DSLR configuration were calibrated by replacing the burner and thermocouple with a calibrated light source (Gamma Scientific RS-10D). The surface of the calibrated light source was placed at the same location previously occupied by the thermocouple, and faced first toward the spectrometer and then toward the DSLR camera.

The junctions of commercial thermocouples are usually nearly spherical with a slightly larger size compared to the wires. The difference in size and geometry potentially introduces a temperature difference between the junction and its adjoining wires. In order to minimize the temperature difference, special care was taken by welding the Pt and Pt-10% Rh wire together as a cylindrical junction. The wires were welded using an acetylene/oxygen micro welding torch with 0.154 mm orifice diameter tip (Smiths little torch size 2 tip) under a digital microscope. A nearly ideal cylindrical junction can be made without too much difficulty. [A video showing the procedure is included in the supplemental material of [Ma 2013].] The diameter of the thermocouple wire was

measured to be 200 μm and agrees very well with the manufacturer's specification. The junction also showed no difference in size compared with the adjoining wires as shown in Fig. 2.13. By doing this, we can assume that the temperature reading represents the junction temperature as well as the adjacent wire temperature given the fact the flame temperature distribution is also flat.
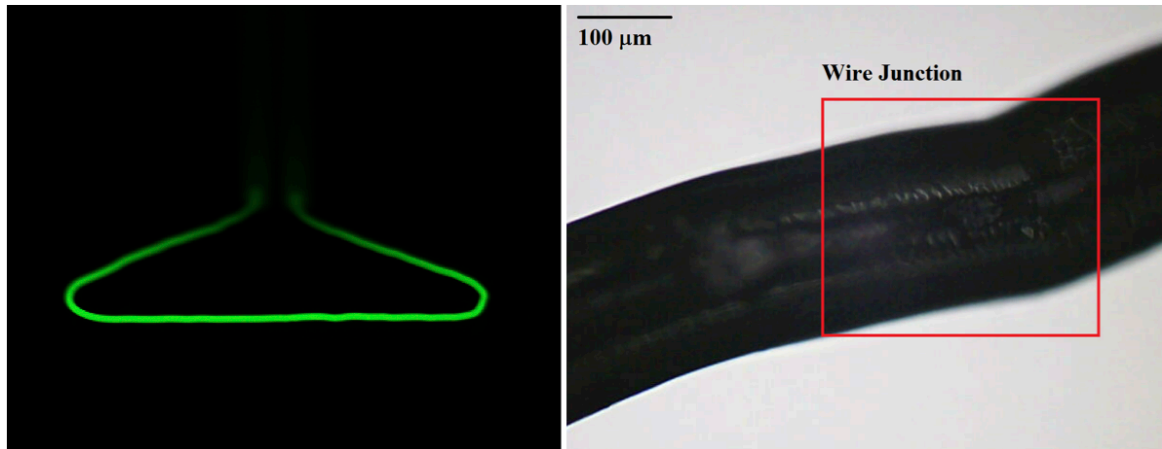
Fig. 2.13. A color image of the incandescent thermocouple in a premixed CH4/air flat flame, filtered through a 532 nm interference filter (left) and the welded cylindrical junction under a digital optical microscope (right).

2.3.4.2 Spectral emissivity measurements

The 5 mm central region of the wire was imaged with the welded junction in the middle, and Pt and Pt-10% Rh wire on the two sides of the junction. The image captured by the DSLR camera showed that the intensity distribution was flat over the region, with the variation between the two wires smaller than 1%. This indicates that the emissivities of Pt and Pt-10% Rh are very close, which is in accordance with previous work [Neuer 1998] that demonstrated Pt and Pt-20% Rh have very close spectral emissivities. Based on the close emissivity of Pt and Pt-10% Rh, a nearly ideal cylindrical junction and the flat temperature distribution, the central 5 mm region of the wire was treated as a uniform filament light source with temperature measured by the thermocouple itself. The following measurements were all carried out within this region.

The thermocouple was aged on the stable flat flame for 80 minutes to examine the stability of its emission over time. The temperature was measured every minute and the maximum variation was shown to be smaller than 1.2 K. The spectra of the thermocouple wire were measured every minute and results are superimposed in Fig. 2.14, which shows very good stability over the inspected time.
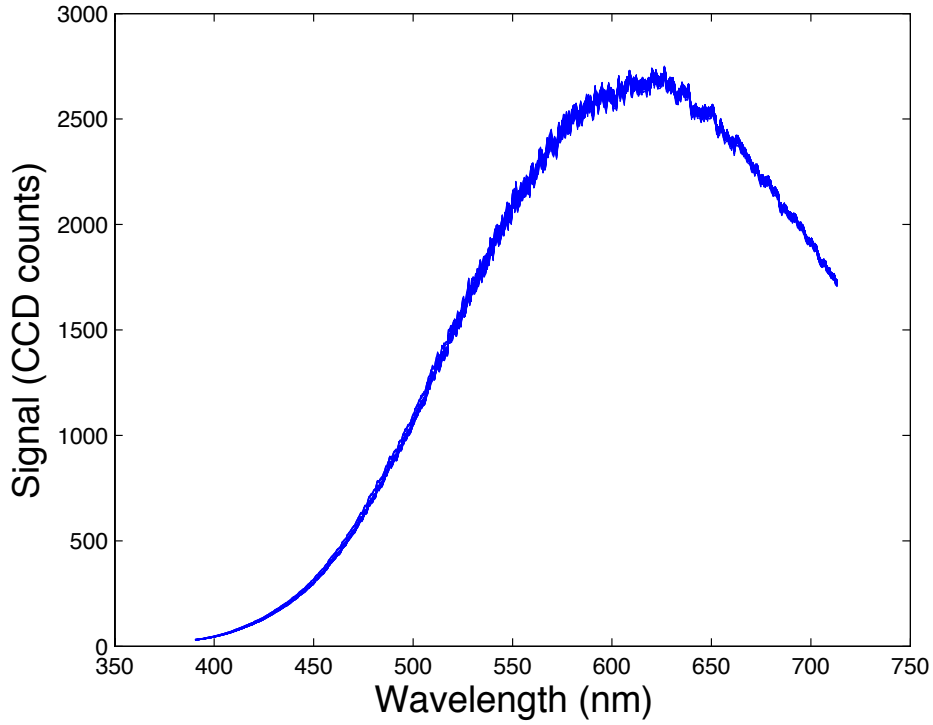
Fig. 2.14. Superposition of 80 measured spectra acquired at one-minute intervals.

The spectral emissivity of the wire was measured by the spectrometer and discrete interference filters independently. From the spectrometer, the emissivity, $\varepsilon(\lambda)$, is obtained from Eq. (2.3.2),

$$\varepsilon(\lambda) = \frac{Spec_{TC}(T_{TC}, \lambda) / \tau_{TC} / D_{TC}}{BB(T_{TC}, \lambda) \times \eta(\lambda)} \qquad (2.3.2)$$

where $Spec_{TC}(T_{TC}, \lambda)$ is the thermocouple wire spectra averaged over the uniform area of the spectral image recorded by the interline CCD camera. The signal is normalized to unit time by dividing by the exposure time τ_{TC}. The wire is considered to be a Lambertian emitter, and the signal intensity is also normalized by the measured wire diameter D_{TC}. T_{TC} is the measured thermocouple wire temperature and $BB(T_{TC}, \lambda)$ is the blackbody

44

spectral radiance calculated by Planck's equation as shown in Eq. (2.3.3),

$$BB\left(T_{TC}, \lambda\right) = \frac{2hc^2}{\lambda^5} \frac{1}{\exp\left(hc / \lambda k T_{TC}\right) - 1} \qquad (2.3.3)$$

with h, c, and k being Planck's constant, the speed of light, and the Boltzmann constant, respectively. $h(\lambda)$ is the combination of the spectral throughput of the spectrometer and the spectral response of the CCD camera, which is determined using the calibrated light source by Eq. (2.3.4).

$$\eta(\lambda) = \frac{Spec_{LS}(\lambda) / \tau_{LS} / D_{LS}}{Rad_{LS}(\lambda)} \qquad (2.3.4)$$

$Spec_{LS}(\lambda)$ is the measured spectrum of the calibrated light source, which is normalized by τ_{LS} and D_{LS}, where τ_{LS} is the exposure time used while acquiring the light source spectrum and D_{LS} is the height of the source area that was imaged through the spectrometer slit as determined by the slit size and the demagnification ratio of the imaging lens. $Rad_{LS}(\lambda)$ is the spectral radiance data supplied by the light source manufacturer.

The spectral emissivity at selected wavelengths can also be obtained by imaging the thermocouple wire incandescence through different interference filters. The images were captured by the DSLR camera in raw format and the color images were converted to grayscale images by summing up the red, green, and blue (RGB) channels. The camera spectral response curves were also converted to grayscale by summing up the RGB spectral response curves. The image of the thermocouple wire was cropped around the

45

junction into a rectangle 115 pixels wide and 40 pixels high. The width corresponds to 2.5 mm spatially, in which the wire temperature distribution is flat and can be indicated by the thermocouple-measured temperature with small uncertainty. The height is made big enough to include all the thermocouple incandescence projected onto the sensor. The cropped image was then integrated vertically into a one-dimensional array. Each element corresponds to the collected signal at positions along the thermocouple, expressed as CCD counts. The distribution of the array intensity is flat, and its average value was used as the thermocouple signal value to get better signal-to-noise ratio. The average is expressed as $S_{TC}(T_{TC}, \lambda_f)$ in Eq. (2.3.5), which is used to calculate the spectral emissivity.

$$\varepsilon\left(\lambda_f\right) = \frac{S_{TC}\left(T_{TC}, \lambda\right) / \tau_{TC} / D_{TC}}{C\left(\lambda_f\right) \int BB\left(T_{TC}, \lambda\right) \times SR\left(\lambda\right) \times IF_{\lambda_f}\left(\lambda\right) d\lambda} \quad (2.3.5)$$

λ_f is 431 nm, 532 nm, 600 nm and 700 nm, corresponding to the center wavelengths of the interference filters. $C(\lambda_f)$ is the optical constant that accounts for geometric factors of the setup and transmission efficiency of the optics, $SR(\lambda)$ is the grayscale spectral response of the DSLR camera, and $IF_{\lambda_f}\left(\lambda\right)$ is the transmission profile of the interference filter being considered. The optical constant can be determined using the calibrated light source from Eq. (2.3.6),

$$C\left(\lambda_f\right) = \frac{S_{LS}\left(\lambda_f\right) / \tau_{LS} / D_{LS}}{\int Rad_{LS}\left(\lambda\right) \times SR\left(\lambda\right) \times IF_{\lambda_f}\left(\lambda\right) d\lambda} \quad (2.3.6)$$

where $S_{LS}(\lambda_f)$ is the vertically integrated and horizontally averaged signal (i.e., processed the same way as for the thermocouple) of the calibrated source filtered by the

46

corresponding interference filter. t_{TC}, D_{TC}, τ_{LS}, and D_{LS} are all as previously defined. It should be noted that for narrowband interference filters, $IF_{\lambda_f}(\lambda)$ is much narrower than features in either the detector response or the light source distributions. In this case, the detector response does not need to be characterized, but it is included here for completeness.

The emissivity measurements were carried out at five thermocouple temperatures equally spanned between 1597 K and 1730 K. The thermocouple temperature was tuned by changing the distance between the burner and the thermocouple, as well as the stoichiometric ratio of the premixed flame. The measured emissivity between 431 nm and 700 nm at the five temperatures are shown in Fig. 2.15. The red curves are continuous emissivity measured by the spectrometer while the blue dots are discrete emissivity measured by interference filters. The measured emissivities at different temperatures are close, indicating that the emissivities depend on temperature weakly in the investigated range.
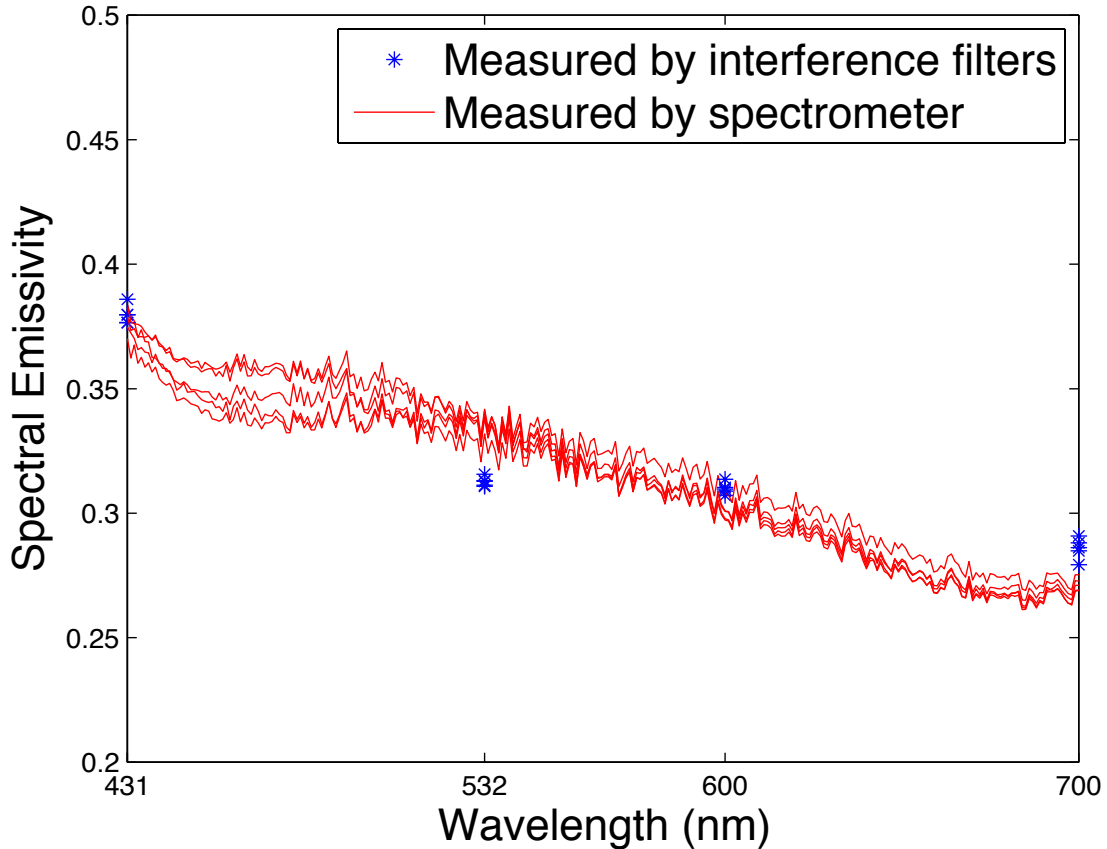
Fig. 2.15. Measured spectral emissivities from 1597 K to 1730 K.

The measurement was repeated six times. The thermocouple wire was initially purchased new and then became aged in experiments, the total in-flame aging time is estimated to be at least six hours. The measured emissivities do not have significant variation, which again indicates the wires are relatively resistant to aging. A 50 μm diameter thermocouple with cylindrical junction was also fabricated and used in the experiments following the same procedure. The measured emissivity agrees very well with experiments on the 200 μm thermocouple. Based on multiple measurements, the relative standard deviations of these measurements are found to be smaller than 2.7%. A second order polynomial fit was then made to facilitate emissivity lookup in the visible

range from 400 nm to 700 nm as described by Eq. (2.3.7), where λ is the wavelength with units of nm.

$$\varepsilon(\lambda) = 1.2018 \cdot 10^{-6} \times \lambda^2 - 1.7167 \cdot 10^{-3} \times \lambda + 0.9017 \qquad (2.3.7)$$

The measured data are shown in Fig. 2.16 and comparison is made against previous experiments [Worthing 1926]. Good agreement is achieved. It should be noted that although the emissivity measurements were done in a relatively narrow temperature range that is mainly limited by the heating flame, the measured emissivity values should be valid for a broader range as indicated by [Worthing 1926], in which a much broader temperature range (1200 K -1800 K) was utilized and small variations were found.
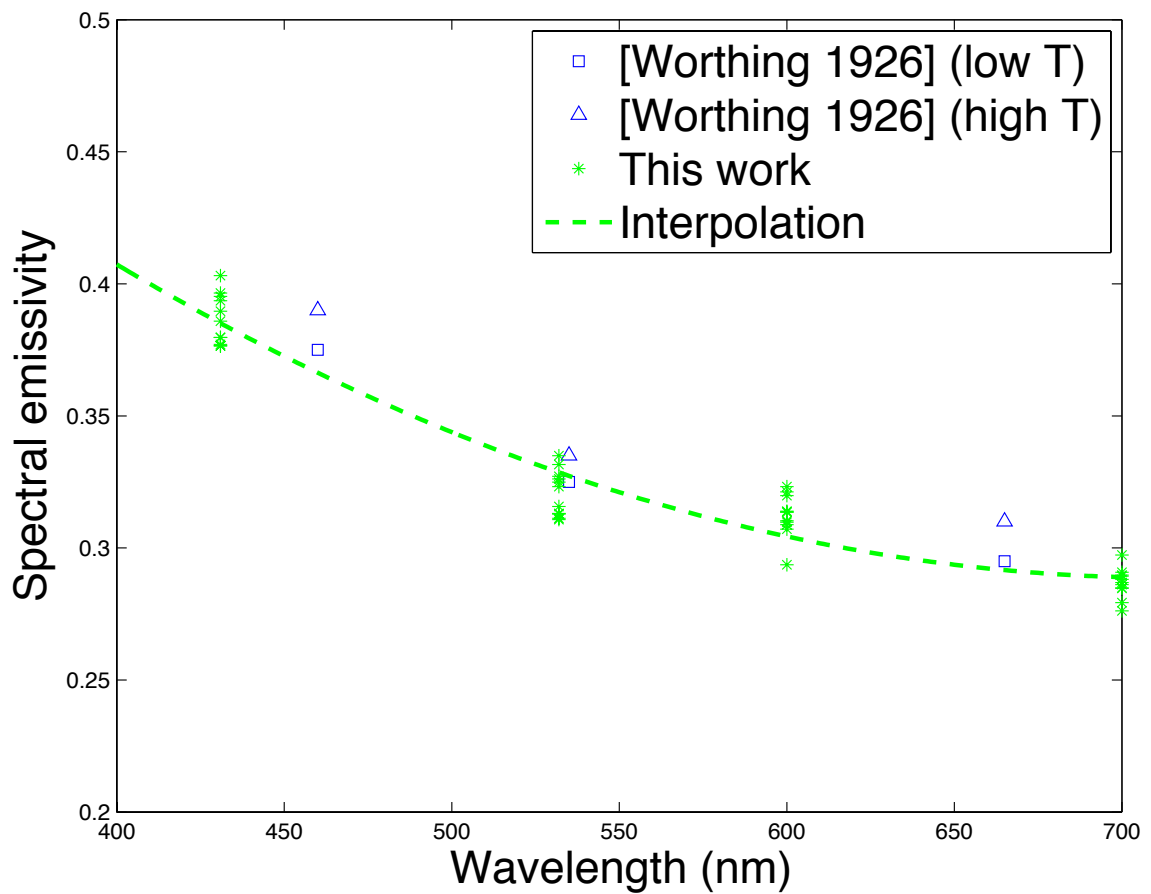
Fig. 2.16. Measured emissivities from this work (Green asterisks) and an interpolated curve (Green dashed line). Comparisons were made with previous work done by [Worthing 1926] (Blue squares and triangles). For the data from Worthing, low T and high T refer to the temperature range for each wavelength; all temperatures are higher than 1200K.

2.3.4.3 Use of S-type thermocouples as an absolute light calibration source

Once the spectral emissivity is known, the S-type thermocouple can be placed into the target experimental setup and serve as an absolute light calibration source. As a demonstration of the suitability of the thermocouple as an absolute light calibration source, the absolute number density of CH* was measured on a stable lifted coflow laminar diffusion flame. The fuel flow is 65% CH_4 diluted by 35% N_2 by volume with a constant velocity of 35 cm/s; it is surrounded by a 35 cm/s air coflow. Flame emission intensity measurements are line-of-sight-integrated and the two-dimensional, in-plane intensity distribution is recovered with an Abel deconvolution [Walsh 2000a]. The emission signal, S_{em}, from this steady-state concentration for a specific electronic transition between an excited state, u, and a ground state, g, during the time interval τ is given by Eq. (2.3.8)

$$S_{em} = A_{ug} n_{exc} V_{em} \tau \frac{C(\lambda_f)}{4\pi} \int \overline{E}(\lambda) \times SR(\lambda) \times IF_{\lambda_f}(\lambda) d\lambda \quad (2.3.8)$$

where A_{ug} is the Einstein's emission coefficient of the observed vibrational band (s^{-1}), n_{exc} is the steady-state number density of excited species (cm^{-3}), V_{em} is the observed volume and τ is the exposure time. $\overline{E}(\lambda)$ is the spectral radiance of CH* simulated by LIFbase [Luque] at 1900 K and normalized to one photon energy. $SR(\lambda)$ is the spectral response of the detector, $IF_{\lambda_f}(\lambda)$ is the transmission of the interference filter centered at λ_f. The factor $C(\lambda_f)$ is the absolute calibration factor appropriate for the specific experimental configuration being used. For these CH* measurements, $SR(\lambda)$ is essentially constant over the narrow wavelength range where $IF_{\lambda_f}(\lambda)$ and $\overline{E}(\lambda)$ are nonzero and can thus be

neglected.

Previous work on the same flame used Rayleigh scattering for absolute intensity calibration, which then allowed determination of the absolute CH* concentration [Luque 2000]. Here the S-type thermocouple calibration method was used to obtain the absolute calibration. The thermocouple was mounted horizontally above the flame where the incandescence of the wire has no interference from flame chemiluminescence, and the thermocouple was heated to 1658 K as indicated by the thermocouple reading. The optical emission from CH* and the thermocouple were measured on a CCD camera (SBIG ST-402 ME) with a Nikkor 50 mm camera lens using a narrow bandpass filter (10 nm FWHM at 431 nm). The image processing procedure is the same as in measuring the spectral emissivity. The cropping region for the thermocouple calibration was made smaller (15 pixels wide and 40 pixels high) for better temperature accuracy since the temperature distribution is less flat compared with the flat flame case. The optical constant $C(\lambda_f)$ was determined by Eq. (2.3.6), using the interpolated spectral emissivity value of 0.385 at 431 nm. The Abel-inverted CH* distribution is shown in the upper right corner of Fig. 2.17. To facilitate quantitative comparison with previous measurements [Luque 2000], the CH* number density was integrated across the flame front. The integration volume is 100 μm along the jet axis by 100 μm effective measurement thickness by 1 cm (from the jet axis) in the radial direction. The large radial distance in the integration volume ensures that all of the CH* at a given downstream location is included in the sum. Results are shown in the main part of Fig. 2.17 for this measurement and for measurements calibrated with Rayleigh scattering in [Luque 2000]. The agreement of two measurements is excellent, and the calibration procedure based on the

S-type thermocouple is much simpler.
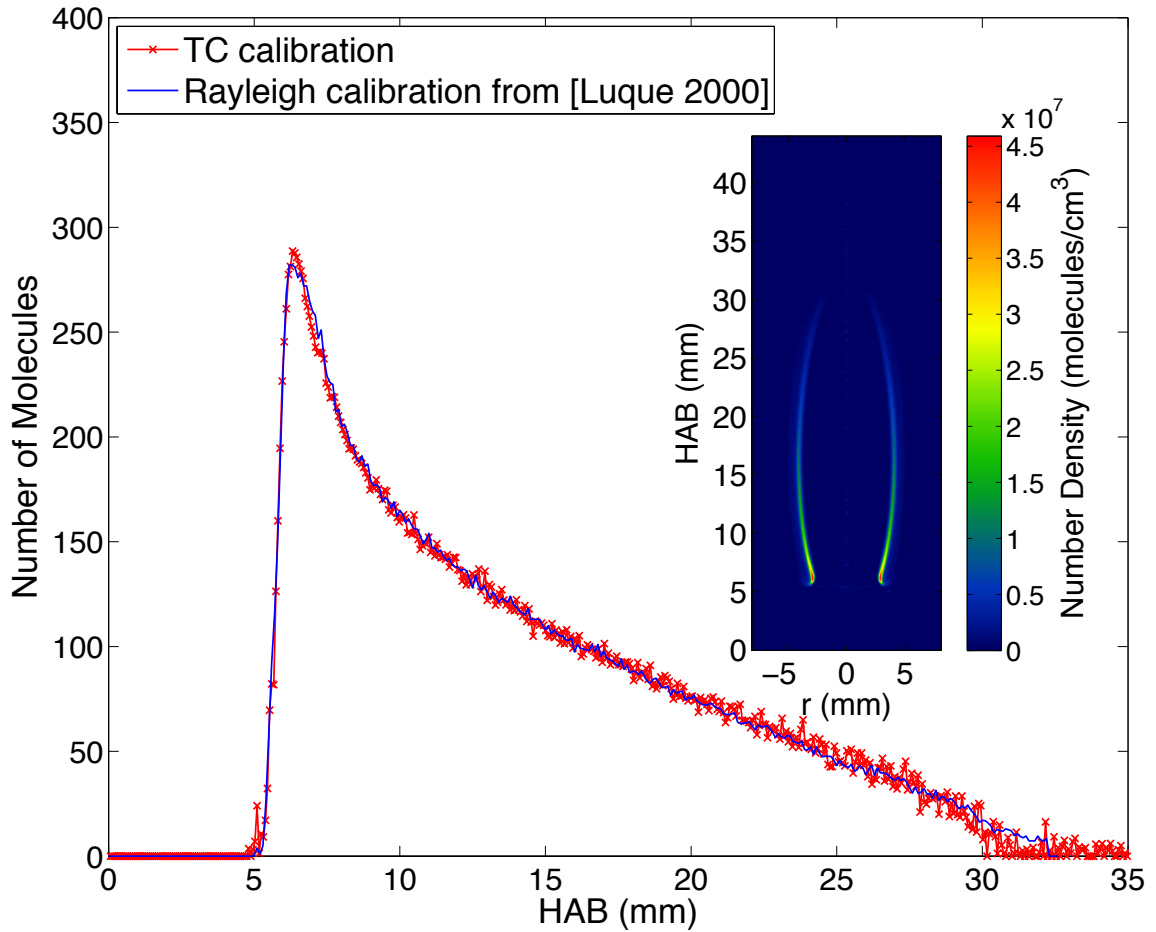
Fig. 2.17. Integrated, steady-state CH* versus height above the burner (HAB), calibrated by S-type thermocouple (red line) and Rayleigh scattering calibration (blue line) from [Luque 2000]. The inset shows the CH* number density with units of molecules/cm^3.

The S-type thermocouple calibration method was also used to determine the absolute soot volume fraction in sooting ethylene diffusion flames. The Nikon D300s has been fully characterized following the method described in Section 2.2.2 and also in [Kuhn 2011], which enables the camera to serve as a two-color ratio pyrometer. Based on the best knowledge of soot spectral emissivity, a look up table for soot temperature can be made as shown in Fig. 2.7. Details of the temperature measurement method are described in Section 2.2.5 and also in [Kuhn 2011]. Once the soot temperature is known, the soot volume fraction, f_v, can be determined if an absolute intensity calibration is available for the specific optical configuration used. Following the same formulation of Eq. (2.2.4), the thermocouple is used as the calibration source instead of the SiC fiber, a slightly modified equation as shown in Eq. (2.3.9) is used to determine f_v.

$$f_v = -\frac{\lambda_s}{K_{ext}L}\ln\left\{1 - \varepsilon_{TC}(\lambda_s)\frac{\tau_s}{\tau_{TC}}\frac{S_S}{S_{TC}} \times \exp\left[-\frac{hc}{k\lambda_s}(\frac{1}{T_{TC}} - \frac{1}{T_S})\right]\right\} \qquad (2.3.9)$$

where all the parameters are the same as described in Eq. (2.2.4), with subscripts *TC* and *S* corresponding to the thermocouple and soot, respectively. The effective filter wavelength, λ_S, is the wavelength at the maximum value of the product of the camera filter response and the Planck blackbody intensity evaluated at the particular soot temperature. The green channel of the color image is used to calculate soot volume fraction. The effective filter wavelength is calculated to be around 533 nm; therefore $\varepsilon_{TC}(\lambda_s)$ is interpolated to be 0.33. The derived soot volume fraction agrees well with previously published measurements using laser-induced-incandescence [Smooke 2005] as shown in Fig. 2.18.
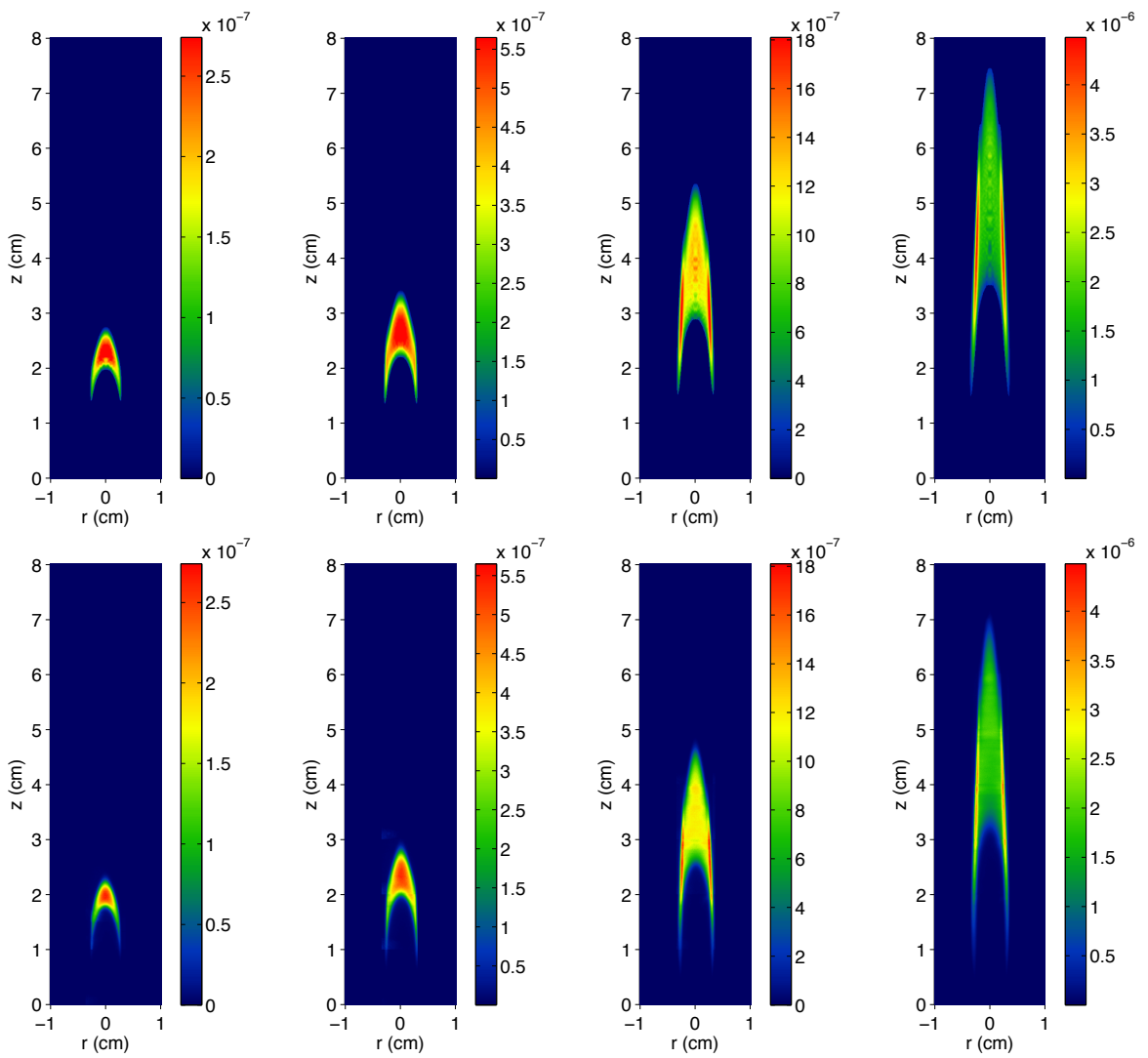
Fig. 2.18. Soot volume fraction measured using pyrometry with thermocouple calibration (top) and LII (bottom) [Smooke 2005] from four nitrogen-diluted ethylene flames with fuel concentrations (from left to right) of 32%, 40%, 60% and 80% C_2H_4.

Another useful application of S-type thermocouples is to validate the measured spectral response curves obtained previously. The measured camera spectral response (shown in Fig. 2.3) and the spectral emissivity of S-type thermocouples (as shown by Eq. (2.3.7)) can be used together to calculate a color ratio/temperature lookup table based on Eq. (2.2.3) as shown by the solid curves in Fig. 2.19. Thermocouple images at various temperatures can then be taken. The temperature readings and the color ratios around the junction are plotted as asterisks in Fig. 2.19 to validate the calculated curves. The excellent agreement between the calculated curves and the calibration points are shown to be comparable with blackbody calibrations as shown in Fig. 2.5 - Fig. 2.7.

In the above case, the S-type thermocouple is used as a calibrated light source to validate camera spectral response. Taking the reverse approach, where the camera is considered as a well-characterized pyrometer and the spectral emissivity model of S-type thermocouples is known, the temperatures can be obtained from ratio pyrometry. A test was performed in the same flat flame with varying equivalence ratios. Both thermocouple color images and thermocouple readings were recorded simultaneously. Temperatures can be measured using the captured color images based on the color-ratio pyrometry technique as discussed in Section 2.2.3. The pyrometry-derived temperatures at different flame conditions are plotted in Fig. 2.20, together with the corresponding thermocouple readings. It is shown that agreement is very good and the maximum difference between the two independent measurements is ~ 3 K. This provides another good way, similar to SiC fiber thin-filament pyrometry but with a different emissivity model, to measure temperatures by using bare platinum wires even without junctions. However, the catalytic

effects and the lower melting point of platinum might preclude its popularity as compared with SiC fiber based thin-filament pyrometry.
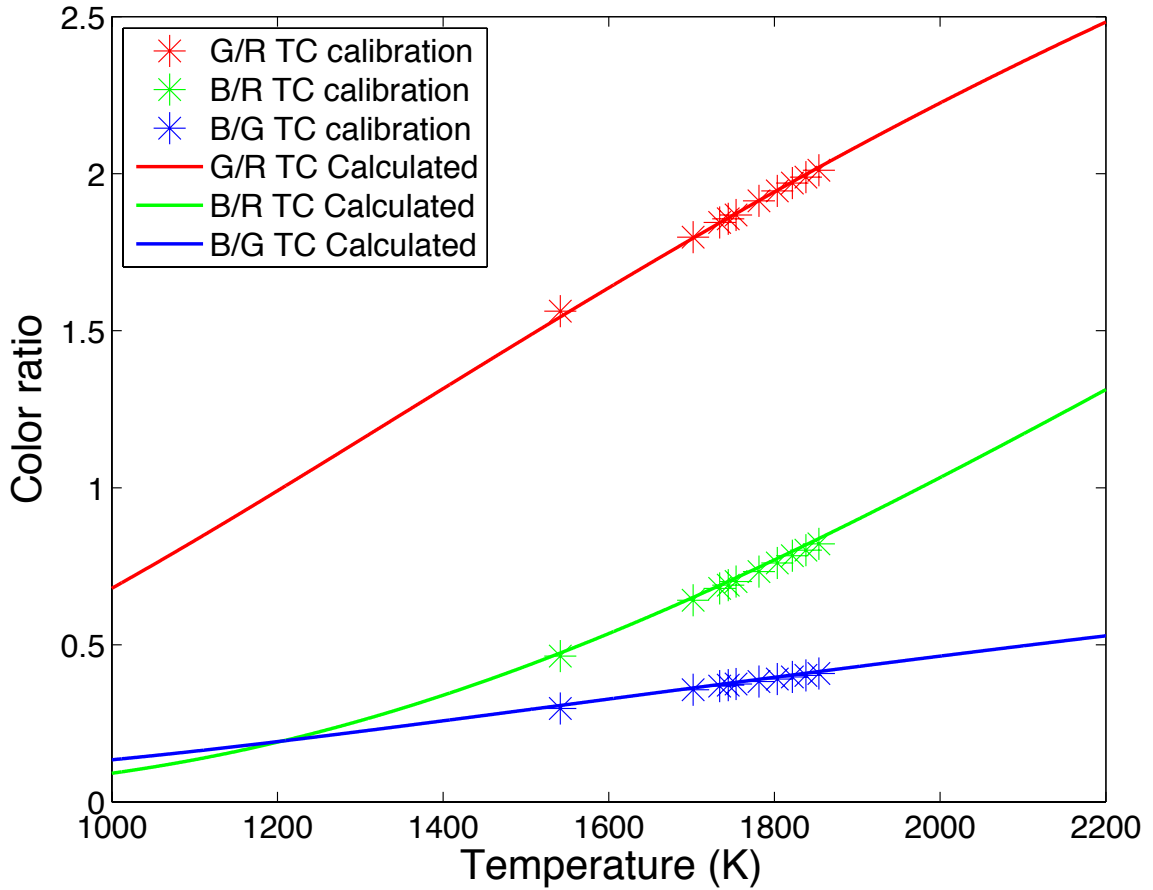
Fig. 2.19. Validation of the measured camera spectral response by comparing calculated and measured color ratios from S-type thermocouples at different temperatures.
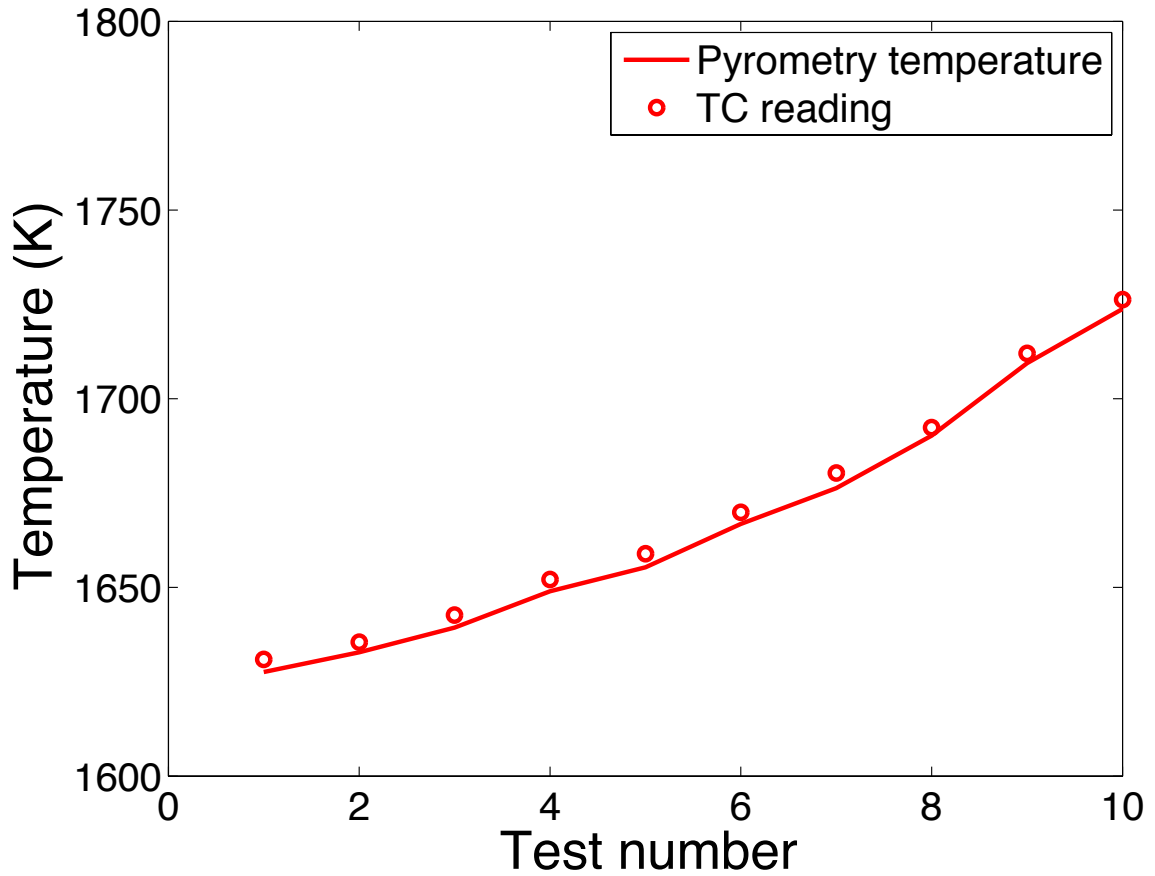
Fig. 2.20. Comparison of pyrometry-derived thermocouple temperature and thermocouple readings

The application of the method is not limited to the cases considered above. It could be potentially useful in small volume experiments (e.g., a combustion chamber) where ordinary calibration sources such as tungsten lamps are too big. While utilizing the method, the thermocouple temperature should not exceed the thermocouple's working range or be so low as to yield insufficient incandescence signals. The thermocouple temperature can be optimized by changing the distance between the thermocouple and the flame front, or even changing the flame temperature itself. The calibration should be

valid as long as the optical setup is unchanged.

2.3.4.4 Thermocouple aging

When putting materials into a hostile environment such as a flame, there is always the possibility of certain degrees of aging. A similar spectral emissivity measurement was performed on the same thermocouple roughly one year after the original measurements shown in Section 2.3.4.2. The thermocouple was continuously used in various experiments in that period of time and the total in-flame time is expected to be at least 10 hours. The new measurements yield a new empirical equation to infer spectral emissivity as shown by Eq. (2.3.10).

$$\varepsilon(\lambda) = 1.0670 \cdot 10^{-6} \times \lambda^2 - 1.5375 \cdot 10^{-3} \times \lambda + 0.8581 \quad (2.3.10)$$

The original curve shown by Eq. (2.3.7) and the further aged curve are both plotted in Fig. 2.21 for comparison. The maximum difference is 5.5% at 700 nm; while for blue light near 400 nm, the difference is only 1.6%.

Care should always be taken to reduce such aging effects, for example by placing the thermocouple at a post-flame location where the chemical reaction is less active but still hot enough to heat the thermocouple to glow, and also minimizing the total thermocouple aging time. Nevertheless, the difference shown in Fig. 2.21 provides an estimate of the calibration uncertainty. The spectral emissivities have not changed significantly after one year of use.
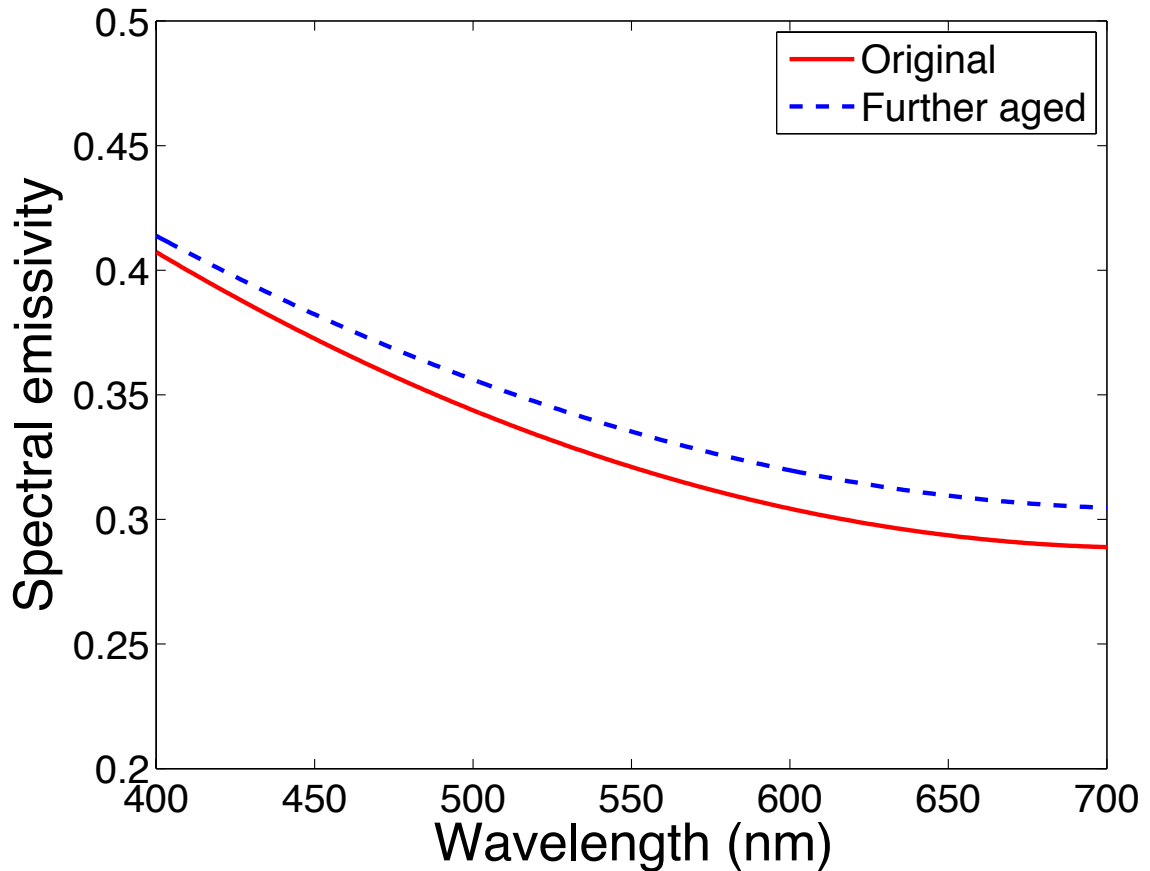
Fig. 2.21. A comparison of the spectral emissivities of a relatively new and aged thermocouple.

2.4 Conclusions

A color-ratio pyrometry technique using consumer DSLRs has been developed. Three consumer DSLRs, (one based on a CCD detector, the others with CMOS sensors) have been fully characterized as ratio-pyrometers with single-shot measurement capabilities. The technique was found to work well for ratio pyrometry of SiC fibers and soot. Measurements of gas temperature, soot temperature and volume fraction have been made in four C_2H_4 flames with varying levels of N_2 dilution, and compared with numerical simulations. Soot volume fraction was originally calibrated using SiC fiber incandescence. A better approach to perform absolute light intensity calibration using S-

60

type thermocouples was developed to improve the accuracy. The spectral emissivity of the Platinum wire has been measured in the visible range. The thermocouple temperature is readily obtained from thermocouple reading. The spectral radiances of a flame-heated thermocouple can then be calculated using Planck's equation and serve as a light intensity calibration source. Examples of using the approach are also provided to demonstrate the applications.

3   Intensity-ratio and color-ratio thin-filament pyrometry

3.1   Introduction

Thin-filament pyrometry (TFP) has been proven to be a useful approach to measure flame temperature. It offers one-dimensional temperature measurement along the length of the filament. In the most common usage, TFP involves placing a thin filament, typically Silicon Carbide (SiC) fibers, in hot gases and determining the fiber temperature from the incandescence of the glowing fiber. The local gas temperature is then derived from the fiber temperature after radiation correction. Compared to laser-based techniques, the TFP approach has the advantages of low-cost and simplicity, and it is useful in situations in which laser-based techniques are difficult to apply (e.g., in high pressure environments where laser-based techniques suffer beam steering problems and spectroscopic issues). Compared to thermocouple measurements, SiC fibers were found to have better resistance to oxidation and catalytic effects [Struk 2003]. The higher melting temperature (~ 2673 K) [Vilimpoc 1989] of SiC enables the fibers to survive in most flames. The TFP approach also offers line measurements as opposed to point measurements by thermocouple.

The TFP approach for measuring temperature has been investigated and applied in a number of studies over the last decades. Vilimpoc *et al*. [Vilimpoc 1989] first demonstrated the feasibility of measuring temperature using the TFP intensity-ratio approach with a 15 μm SiC fiber, and they estimated the temporal response to be ~ 1 ms and the spatial resolution along the fiber (based on thermal conductivity) to be ~ 100 μm. Bedat *et al*. [Bédat 1994] performed TFP measurements in a weakly turbulent flame at a rate of 2500 Hz in the infrared and extended the lower temperature limit to 550 K. In

their experiments, fiber greybody behavior was assumed. Temperature was measured from a calibrated spectral signal using a tungsten filament and a blackbody light source. Pitts *et al*. applied TFP in flickering laminar diffusion flames [Pitts 1996], and also investigated the effects of finite time response and soot deposition [Pitts 1998]. The intensity-ratio approach was employed for temperature measurements in their studies with temperature calibrated in a steady calibration flame. Struk *et al*. [Struk 2003] performed TFP measurements in a steady diffusion flame using a spectrometer based on the greybody assumption, and compared the results with thermocouple measurements. The temperature uncertainty is shown to be ±38 K. Maun *et al*. [Maun 2007] performed TFP measurements in a steady diffusion flame with temperature calibration performed with a butt-welded type B thermocouple. The derived gas temperature uncertainty was estimated to be ±60 K. Blunck *et al*. [Blunck 2009] applied the TFP intensity-ratio approach in unsteady hydrogen flames with temperature calibration performed in a McKenna burner. The fiber temperature uncertainty was estimated to be 6% at 1000 K and 10% at 2400 K. Kuhn *et al*. [Kuhn 2011] developed a color-ratio approach based on a greybody assumption, and utilized a digital color camera for single-shot measurements. Dambach *et al*. [Dambach 2012] applied TFP to estimate the temperature in the near-flame field resulting from hypergolic ignition. The same temperature calibration was performed as in [Blunck 2009]. Fiber temperature uncertainty was estimated to be 5% at 1000 K and 8% at 1500 K. Some studies [Struk 2003; Maun 2007] evaluated TFP accuracy by comparison to thermocouple measurements, and some [Pitts 1998] compared with Rayleigh scattering measurements.

Despite numerous studies and applications of TFP, there are still open questions

and implementation challenges. All TFP approaches are based either on a temperature calibration or a greybody assumption. However the accuracy of thermocouple calibration, or more generally thermocouple temperature measurement, is affected by the thermocouple junction geometry and radiation correction. In this work, an effective method for manufacturing thermocouples with a cylindrical junction has been used to reduce thermocouple measurement uncertainty. The spectral emissivity of the SiC fiber has also been directly measured in the visible range and the greybody assumption is verified for certain kinds of SiC fibers. Fiber aging behavior, which causes the fiber spectral emissivity to change over time, was found to affect the measurement accuracy and has not been investigated in detail in previous studies. In this work, fiber aging behaviors were studied for six kinds of SiC fibers and the results can be used to effectively reduce the measurement uncertainty. Previous TFP measurements were normally assessed by thermocouple measurements that suffer from uncertainties associated with radiation correction. In this study, well-calibrated flames available at Sandia National Laboratories were used as accurate temperature references to directly assess the accuracy of thermocouple-based and TFP-based temperature measurements. In order to facilitate better usage of TFP approaches and address their uncertainties, the work reviews and discusses current TFP approaches, identifies and investigates their associated error sources, and directly assesses different TFP approaches against N_2 CARS measurements in well-calibrated flames. Finally, results of uncertainty analysis are presented along with suggestions on ways to reduce measurement uncertainty.

3.2 Experimental approaches

Thin-filament pyrometry does not measure gas phase temperature directly. Instead,

fiber surface temperature is determined in the first step, followed by a radiation correction to calculate the difference between the gas and fiber temperature. This second step is accomplished by solving the energy conservation equation on a segment of the fiber. For determination of the fiber temperature, two approaches, based on intensity-ratio and color-ratio, will be discussed. This section focuses on reviewing the physical background of the experimental approaches.

3.2.1 Intensity-ratio approach

The intensity-ratio approach has been widely used in the past decades since the first use of TFP [Vilimpoc 1989]. The signal of the glowing fiber is correlated to temperature using Planck's law. The intensity ratio, I_R, is defined as the ratio of signal at a measured temperature over the signal at a reference temperature. The ratio can be numerically determined by integrating Planck's equation over the spectral response of the detection system [Vilimpoc 1989; Pitts 1996; Struk 2003]. Constant emissivity over the spectral window (greybody behavior) is normally assumed and knowledge of the detector's spectral response is needed if wideband detection is employed. In the current study, narrowband interference filters were used to restrict the measurement to a narrow spectral window. With narrowband filters, knowledge of the detector spectral response and fiber spectral emissivity are not required, since both can be considered as constants. This simplifies the experiment and reduces potential error associated with uncertainties in the detector response or emissivity model. The intensity ratio, I_R, at different temperatures can be calculated as

$$I_R = \frac{\varepsilon I_b(\lambda, T)}{\varepsilon I_b(\lambda, T_0)} = \frac{e^{\frac{C_2}{\lambda T_0}} - 1}{e^{\frac{C_2}{\lambda T}} - 1} \approx e^{\frac{C_2}{\lambda}\left(\frac{1}{T_0} - \frac{1}{T}\right)} \qquad (3.2.1)$$

where $I_b(\lambda, T)$ is the spectral radiance calculated by Planck's equation at the central

wavelength λ of the interference filter and fiber temperature T. T_0 is the reference fiber

temperature and $C_2 = 14387.86$ μm·K. Assuming the aging effect is small within a

relatively short measurement time of one hour, the fiber spectral emissivity ε at

wavelength λ is assumed to be a constant over the spectral region and is canceled out by

taking the ratio (see Section 3.3 for discussion of these assumptions). A lookup table

correlating the signal ratio and temperature can be calculated using Eq. (3.2.1) and is

shown in Fig. 3.1. The red circle on the curve is the reference point with $I_R = 1$ and $T =$

T_0. Other fiber temperatures can be determined from the relative signals by applying the

calculated lookup table. The reference temperature T_0 is normally obtained through a

calibration procedure that associates a known fiber temperature with its measured signal

to quantify the optical throughput of the setup. It should be noted that such calibration is

setup specific; once the setup is changed, a new calibration must be performed. The

accuracy of the measurement is dependent on the accuracy of calibration (determination

of T_0). In the ideal case, the calibration should be performed at a well-characterized flame

condition where the gas temperature, velocity and species concentrations are known.

These quantities are used in conjunction with a radiation loss calculation to determine T_0.

Any uncertainties associated with the gas properties will adversely affect the accuracy of

T_0. In the less ideal and more common case, the flame temperature is unknown and a

thermocouple (along with a separate radiation correction) is used to infer the flame

temperature. The accuracy of the thermocouple measurement and radiation correction as well as the approaches that can be adopted to reduce uncertainties will be discussed in Sections 3.3 and 3.5.
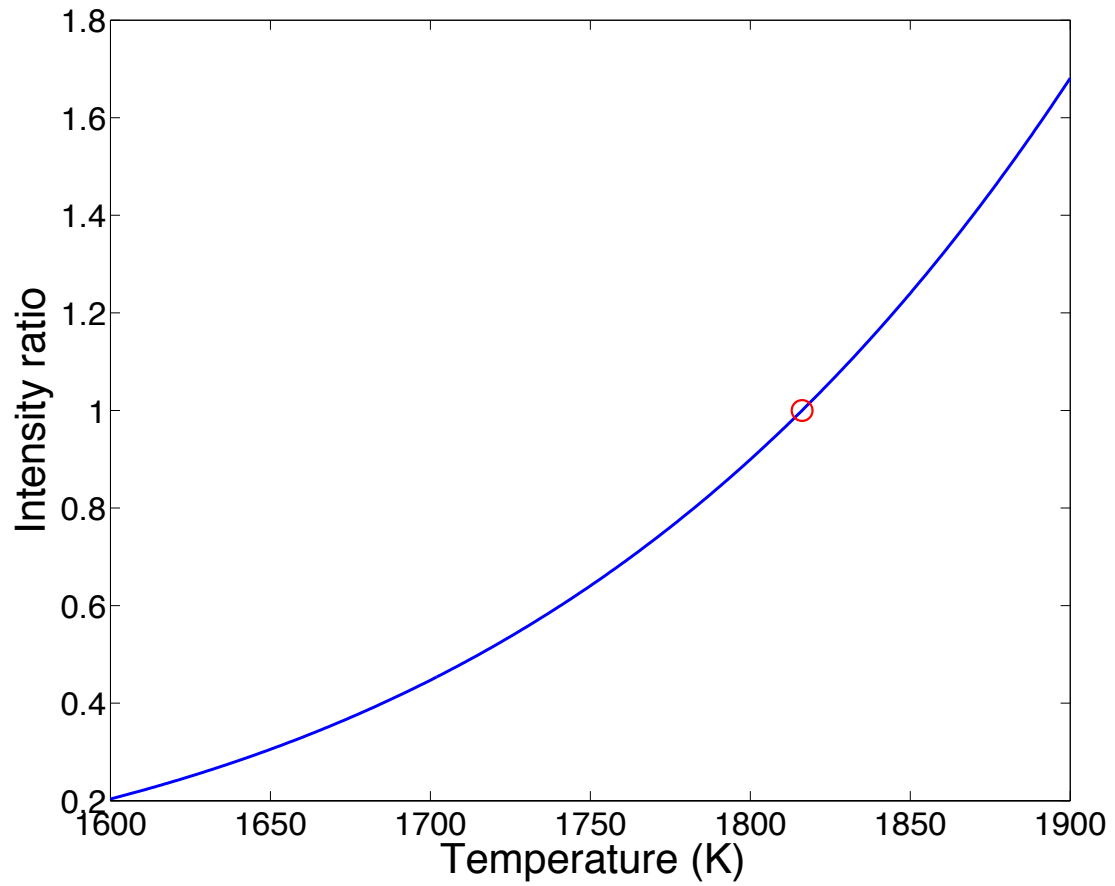
Fig. 3.1. Calculated lookup table with one calibration point at $T_0 = 1820$ K.

3.2.2 Color-ratio approach

As an alternative to the intensity-ratio approach, a color-ratio approach was recently developed for measuring the fiber surface temperature. The details of this approach is described in Chapter 2 and [Kuhn 2011]. Compared with the intensity-ratio approach, the color-ratio approach directly determines the fiber temperature and does not rely on a temperature calibration. It is also less setup dependent and requires no frequent calibration if the setup is changed. In this study, a Nikon digital single lens reflex camera (Nikon D300s) was used. A color glass filter was also used to balance the intensity in the red, green, and blue (RGB) channels for better signal to noise when taking ratios. The spectral response of the camera and filter was experimentally measured [Kuhn 2011] and is shown in Fig. 2.3. The SiC fiber is normally assumed to be a greybody (see Section 3.3). The color ratio, C_R, of any two channels among the RGB channels can be calculated by integrating Planck's equation over the spectral response curve and the lookup table is shown in Fig. 2.7.

3.2.3 Radiation correction

As outlined above, a radiation correction is needed to determine the temperature difference ΔT between the gas temperature and the fiber surface temperature. It is a classic heat transfer problem as the fiber is heated by its surrounding hot gas and cooled by radiation loss. By considering the energy balance equation over a small volume of the fiber and neglecting the trivial heat conduction along the fiber [Vilimpoc 1989; Bédat 1994; Struk 2003; Maun 2007; Kuhn 2011], the gas temperature can be obtained by Eq. (3.2.2).

$$T_g = \frac{\varepsilon \sigma \left(T_f^4 - T_\infty^4\right)}{h} + T_f \quad (3.2.2)$$

where T_g, T_f and T_∞ are the gas phase temperature, fiber temperature and ambient environment temperature, respectively. ε is the total emissivity of the fiber and σ is the Stefan-Boltzmann constant. h is the convective heat transfer coefficient which can be calculated as

$$h = \frac{Nu\, k_{gas}}{D_f} \quad (3.2.3)$$

where Nu is the Nusselt number, k_{gas} is the gas thermal conductivity, and D_f is the fiber diameter.

Review of the literature suggests multiple empirical Nusselt correlations have been used in different experiments [Vilimpoc 1989; Bédat 1994; Struk 2003; Maun 2007; Blunck 2009]. In this work, the correlation from [Rohsenow 1988] as expressed by Eq. (3.2.4) was chosen.

$$Nu = C \times Re^m \quad (3.2.4)$$

where C = 0.800 and m = 0.280 for 0.09 < Re < 1 and C = 0.795 and m = 0.384 for 1 < Re < 35. This correlation covers a wide range of Reynolds numbers, and gives good agreement on gas temperature with independent N_2 CARS measurements, as will be shown in Section 3.4.

3.3   Error sources

Several assumptions are frequently made in TFP measurements. For example the fiber is considered to be optically stable. However, to the best of our knowledge, no detailed study has been published on fiber aging behavior that may cause changes in fiber spectral emissivity over time. Aging could affect the accuracy of both the intensity-ratio and color-ratio approaches and detailed aging tests for several kinds of SiC fibers were performed in this study. Another common assumption is that SiC fibers exhibit greybody behavior, i.e., $\varepsilon(\lambda)$ is a constant. To check this, spectral emissivity measurements in the visible range were also carried out. Another source of error in intensity-ratio measurements is the temperature calibration error associated with thermocouple measurement and radiation correction. Thermocouples are often used to infer the flame temperature that is then used to calibrate TFP intensity-ratio measurements. However, ill-defined thermocouple junction geometry often brings errors in the radiation correction. An approach to reduce thermocouple measurement/calibration uncertainties will also be discussed.

3.3.1   Fiber aging tests

Fiber aging tests were performed on six different types of SiC fibers as summarized in Table 3.1. They are the 12 – 14 μm Ceramic Grade (CG) Nicalon, Hi-Nicalon and Hi-Nicalon type S fibers distributed by COI Inc. [Kook 2012], and the 75 μm SCS-9A, 140 μm SCS-6 and 140 μm SCS-Ultra from SCS specialty materials [Patton 2012]. The smaller fibers are less intrusive and have been used in many lab scale flames during the past decades. The larger fibers are much stronger mechanically and are more likely to survive in harsh flame conditions.

Table 3.1. Summary of SiC fibers evaluated in this study TFP experiments.

SiC fibers	Ø (µm)	Vendor	Aging test results
CG Nicalon	14	COI Inc	Stable
Hi-Nicalon	14	COI Inc	Unstable
Hi-Nicalon-S	12	COI Inc	Stable but fragile
SCS-9A	75	Specialty Materials	Stable
SCS-6	140	Specialty Materials	Unstable
SCS-Ultra	140	Specialty Materials	Unstable
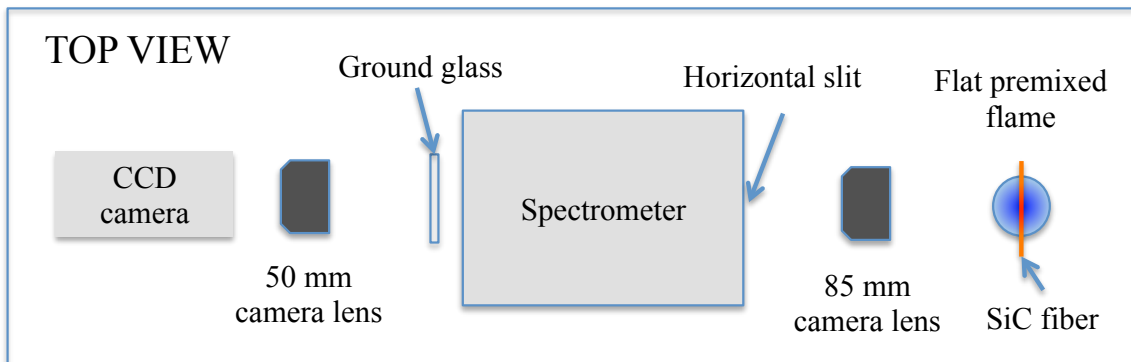
Fig. 3.2. Experimental setup for the fiber aging test and spectral emissivity measurement.

The schematic of the aging setup is shown in Fig. 3.2. The SiC fiber was mounted horizontally above a stable flat premixed CH_4/air flame (5 cm in diameter) at equivalence

71

ratio of 0.9. Tension was applied to the fiber by hanging a small weight (0.5 g) on one end to prevent sagging. The incandescence of the heated SiC fiber was imaged by an 85 mm focal length Canon camera lens into the horizontal slit of a spectrometer (Jarrell-Ash MonoSpec 27) with a 150 groove/mm grating. The f-number of the lens was matched to that of the spectrometer to reduce stray light. The width of the slit is 550 μm, which is wide enough to pass all the fiber incandescence into the spectrometer without clipping the signal. A ground glass diffuser (DG20-1500) was aligned at the focal plane of the spectrometer on which an image of the spectrum was formed. The image was then demagnified and imaged onto an interline CCD camera (Cooke SensiCam with super VGA sensor) to capture wavelengths from 400 to 700 nm while filling the entire image sensor to maximize the spectral resolution. The wavelength was calibrated by a mercury-vapor lamp. The aging behaviors of the six fibers are plotted in Fig. 3.3. The figure shows the normalized intensities at four wavelengths (431, 532, 600 and 700 nm denoted by blue dots, green asterisks, magenta plus and red circles respectively) recorded over a 60-minute time frame from 10 minutes to 70 minutes. The fibers are normally much more unstable during the initial ~ 10 minutes. Therefore the initial period is avoided in the testing and should be avoided in any TFP measurements. The aging time of one hour is limited by the relatively short lifetime of 12 and 14 μm fibers. Larger SCS fibers were tested up to seven hours without breaking in the flame. For the larger fibers, the fiber intensities did not completely stabilize at times greater than one hour; maximum intensity variations up to 30% were observed. Therefore, only the first 60 minutes of aging is used to evaluate the stableness of the fiber and the calibration and measurement should be

performed within a relatively short time of ~ 60 minutes to reduce measurement error due to fiber aging.
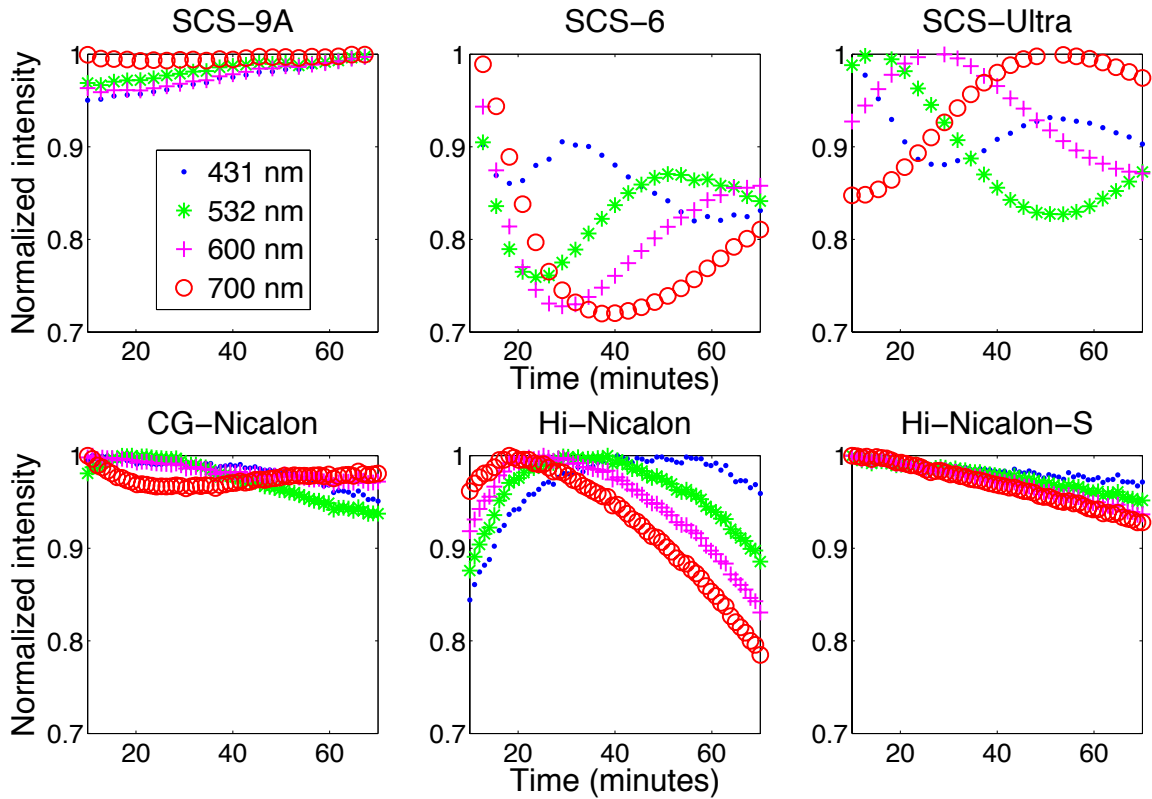
Fig. 3.3. Fiber aging behaviors of six tested fibers.

As can be seen in Fig. 3.3, the 75 μm SCS-9A, 14 μm CG-Nicalon, and 12 μm Hi Nicalon type S fibers have a maximum signal variation of 5 % over 60 minutes. The Hi-Nicalon, SCS-6 and SCS-Ultra fibers are less stable with maximum signal variation up to 22 %. The flame temperature is verified to be stable with maximum temperature variation of 3 K as indicated by thermocouple measurements over a two-hour period. Therefore the signal variation can be attributed to the spectral emissivity variation over time, which is the so-called aging behavior. It should also be noted that greybody behavior is not

maintained for the unstable fiber over time, as the normalized signals at different wavelength do not change in phase with each other. For the stable fibers, greybody behavior is relatively well maintained given the small variation over time (see Section 3.3.2). The effect of aging for both the intensity-ratio and color-ratio approaches will be discussed in Section 3.5. Despite its stable optical properties, the 12 μm Hi-Nicalon type S fiber was found to be more fragile than the other two kinds of stable fibers when in the flame. Therefore only CG-Nicalon fibers and SCS-9A fibers will be used in the following measurements.

3.3.2 Fiber spectral emissivity measurement

Greybody behavior is normally assumed for SiC fibers and is used in the color-ratio approach. To check the validity of this assumption, spectral emissivity measurements were carried out for the CG-Nicalon fiber and the SCS-9A fiber. The measurements were performed in the same setup as shown in Fig. 3.2 and simultaneously with the aging test. The heated glowing fiber was imaged into the spectrometer and its spectral signals were recorded by the cooled CCD camera. The fiber temperature was calibrated against a thermocouple in conjunction with radiation correction (see Section 3.3.3). A standard light source (Gamma Scientific RS-10D) with known spectral radiance was used to calibrate the spectral response of the setup. The spectral emissivities of the SiC fibers were then measured according to Planck's law, as shown in Eq. (3.3.1),

$$\varepsilon(\lambda) = \frac{Spec(T_f, \lambda)/\tau/D}{BB(T_f, \lambda) \times \eta(\lambda)} \qquad (3.3.1)$$

74

where T_f, λ, τ, D and η are fiber temperature, wavelength, exposure time, fiber diameter and calibrated spectral response of the imaging system respectively. *Spec* and *BB* are the measured spectrum and calculated blackbody spectral radiance at the corresponding T_f and λ. More detailed information on the methodology of the spectral emissivity measurement can be found in [Ma 2013].

As can be seen in Fig. 3.4, the spectral emissivity of both the CG-Nicalon fiber (blue dashed curve) and the SCS-9A fiber (red solid curve) over the visible range are relatively constant between 0.8 and 0.9. Due to the relatively low fiber temperature and small spectral response at wavelengths less than 450 nm, the measured spectral emissivities in this range are considered to be less accurate and are not shown. Since the fiber temperature is calibrated against thermocouple measurements carried out at the same location above the flame, the uncertainty of the fiber temperature is subject to the accuracy of the thermocouple reading and the radiation correction. The thermocouple reading is considered to be accurate and catalytic effects are neglected since the measurements were performed at a post-flame location. The major source of uncertainty is considered to be the radiation correction and is estimated to be $\pm$ 15 K according to the direct assessment of thermocouple measurements against N_2 CARS as shown in Fig. 3.6. A corresponding error bar is added on the spectral emissivity to account for the temperature uncertainty. It should be noted that Planck's equation is highly dependent on temperature, thus a small uncertainty on temperature could result in relatively large uncertainty in the determined spectral emissivity. It should also be pointed out that the spectral emissivity measurements were carried out at 40 minutes of aging (see Fig. 3.3). As discussed in the previous section, the spectral emissivity was found to change over

time. However, for the two fibers mentioned here, the overall variation over 60 minutes was small and the greybody assumption holds within certain errors introduced by the aging effect. The uncertainty of the determined fiber temperature based on the greybody assumption will be discussed further in Section 3.5.
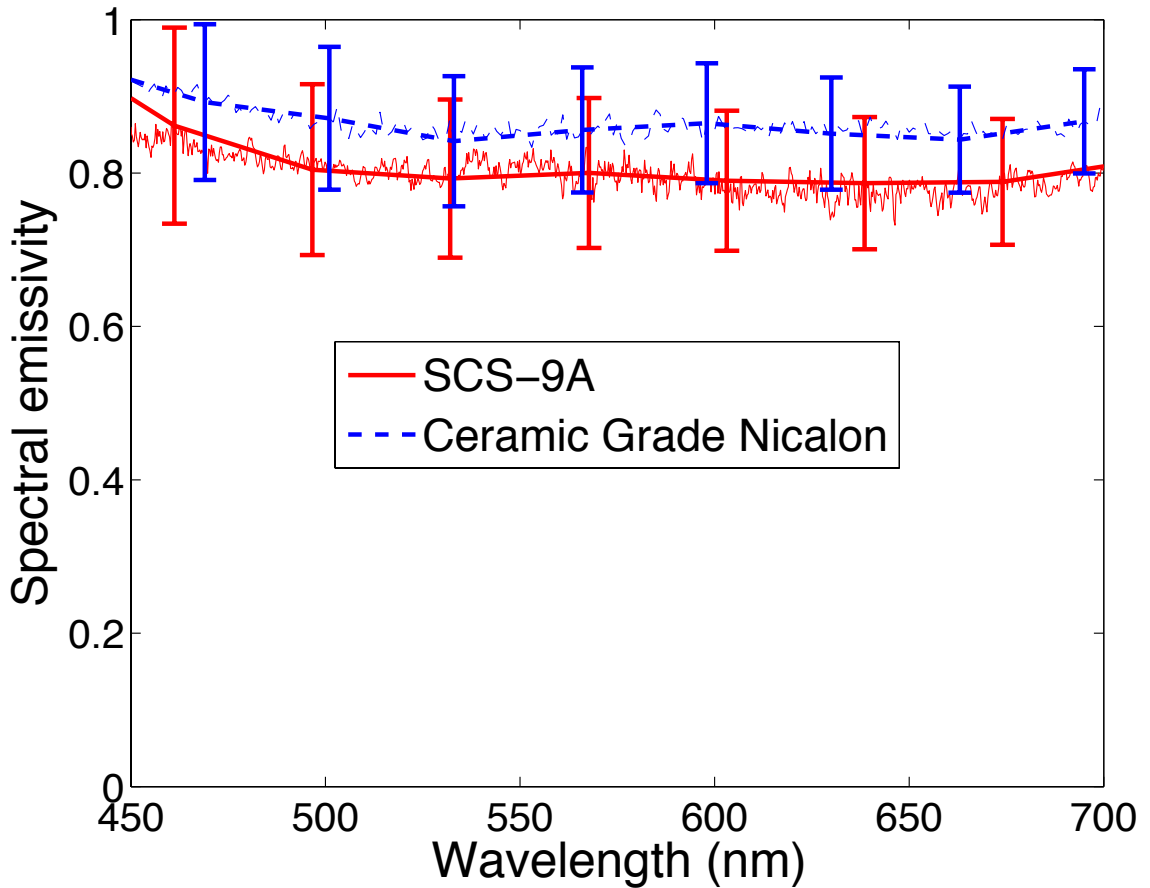
Fig. 3.4. Spectral emissivity of SCS-9A and CG-Nicalon fibers. Error bars correspond to uncertainties in emissivity due to a ± 15 K uncertainty in the fiber temperature.

3.3.3   Thermocouple radiation correction

Thermocouples are often used for flame temperature measurements and calibration of TFP measurements when the intensity-ratio approach is employed. The accuracy of the measured gas temperature is systematically dependent on the calibration uncertainty. Commercial thermocouple junctions may possess an ill-defined geometry that could vary from one thermocouple to another. Errors are likely to be introduced by assuming the junction geometry to be a specific shape such as a cylinder, sphere or spheroid, and using the corresponding Nusselt number correlation for radiation correction. To examine and reduce such uncertainties, thermocouples with well-defined cylindrical junctions were manufactured, and compared with commercial bead and butt-welded thermocouples. Detailed information on the comparison is available in the Appendix. More detailed procedures and a video showing the fabrication of the cylindrical junction can be found in [Ma 2013].

3.4   Direct assessment of measurement accuracy using calibration flames

The accuracy of both TFP approaches as well as that of the radiation correction have been assessed in a well-calibrated CH_4/Air premixed flat flame available at Sandia National Laboratories. Flame temperatures at 3 cm height above the burner of eight conditions from fuel lean to rich were used as calibration points. The temperatures have been measured by N_2 coherent anti-Stokes Raman scattering (CARS), using methods described in [Gordon 2009], and were found to be 35 K below adiabatic equilibrium on average, with an overall uncertainty of $\pm$ 30K. The calibration burner is operated such that all of the flames are slightly lifted above the burner surface, so the temperature

deficit is believed to be due mainly to gas phase radiation. Because the true flame temperatures are expected to follow a smooth curve across the eight flow conditions, the reference conditions of temperature and species concentrations for Raman/Rayleigh calibrations and for the present TFP comparisons are taken from non-adiabatic equilibrium calculations at 35 K below the adiabatic equilibrium temperature for each nominal value of equivalence ratio. It is important to note that there is uncertainty of ~ 2% in the equivalence ratio of the actual calibration flames due to uncertainty in flow controller calibrations.

The intensity-ratio approach was first tested using an SCS 9-A fiber (Table 3.1) in the Sandia calibration flame. A narrowband interference filter centered at 673 nm (FWHM = ~ 10 nm) was used. The flame temperature of 2197 K at equivalence ratio of 1.012 was chosen as the reference point. The fiber temperature at this point was determined to be 1820 K as T_0 in Eq. (3.2.1) through the inverse radiation correction process. The fiber signal at this condition was recorded as the reference signal. To measure gas temperatures at the other seven equivalence ratios, intensity-ratios were first measured with normalization against the reference signal. Such intensity-ratios can be used to determine the fiber temperature through Eq. (3.2.1) or Fig. 3.1 as shown by the blue asterisks in Fig. 3.5. Radiation corrections were then performed to determine gas temperatures as shown by the red squares. In performing the radiation corrections using Eq. (3.2.2)-(3.2.4), the total emissivity of the SiC fiber was taken as 0.88. Fiber diameter was measured to be 75 μm. Given the simplicity of the flat premixed flame, the hot gas velocity was estimated by multiplying the unburned gas velocity by the ratio of flame temperature over unburned gas temperature. In the normal case where flame temperatures

were not known initially, estimation or numerical simulation of velocity should be made. The estimation adds some uncertainty in Nusselt number and its effect on derived gas temperature will be discussed in Section 3.5. All gas transport properties were calculated using online software [Böhm 2011] using major species concentrations for each equivalence ratio as input. In this ideal case where the accuracy of the radiation correction is maximized, the TFP-derived gas temperatures were shown to agree very well with the reference temperatures based on CARS measurements (see Fig. 3.5). The error bars in temperature correspond to the overall uncertainty of ± 30 K in the CARS measurements. Error bars of 2% in equivalence ratio are shown around the TFP-derived gas temperatures.
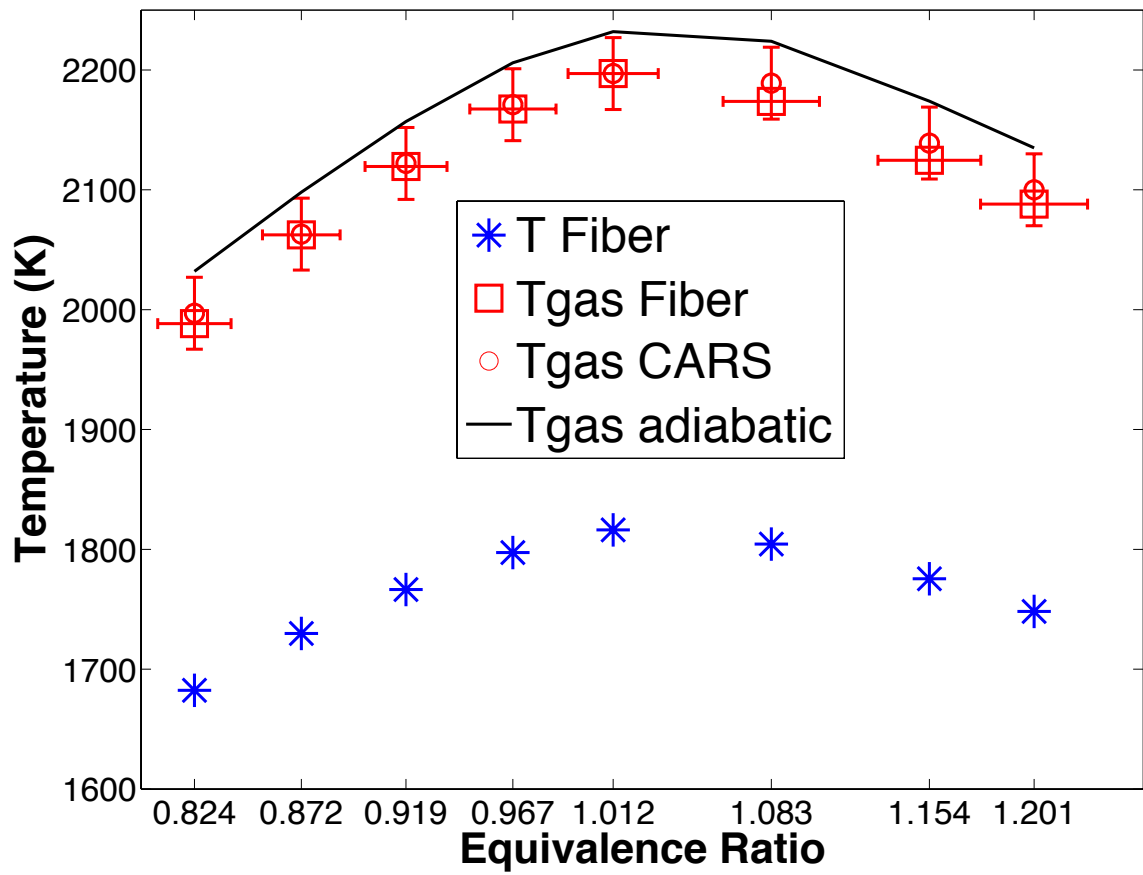
Fig. 3.5. Comparison of intensity-ratio TFP and CARS measurements.

In less ideal cases where the flame temperatures are not known initially, thermocouples can be used to infer the flame temperature. In this study, the measurement accuracy of thermocouples with cylindrical junctions was directly compared with the calibration reference temperatures based on CARS measurements. For a consistency check, two S-type thermocouples with 50 μm and 200 μm cylindrical junctions were manufactured and used to measure the calibration flame temperatures. The thermocouple temperatures were measured over 50 samples in ~ 3 minutes; the maximum temperature variation was ~ 20 K for the small thermocouple and ~ 5 K for the larger thermocouple. The temperature variation was mainly due to flame fluctuation and thermocouple voltage readout noise. The average temperature over 50 samples was used for the comparison. The gas phase temperatures were derived from radiation correction in a similar way as for the SiC fibers. The total thermocouple wire emissivity was chosen to be 0.2 [Maun 2007]. The temperature readings from the 200 μm and 50 μm thermocouples are plotted as blue asterisks and magenta crosses respectively in Fig. 3.6. The derived gas temperatures after radiation correction are shown as blue squares and magenta triangles. The 50 μm diameter thermocouple cannot survive flame temperatures higher than 2000 K; therefore only three temperatures from this thermocouple are shown. Error bars of ± 30 K in the CARS-based reference temperatures and ± 2% in equivalence ratio are included. Good agreement was achieved between the radiation-corrected thermocouple measurements and CARS measurements.
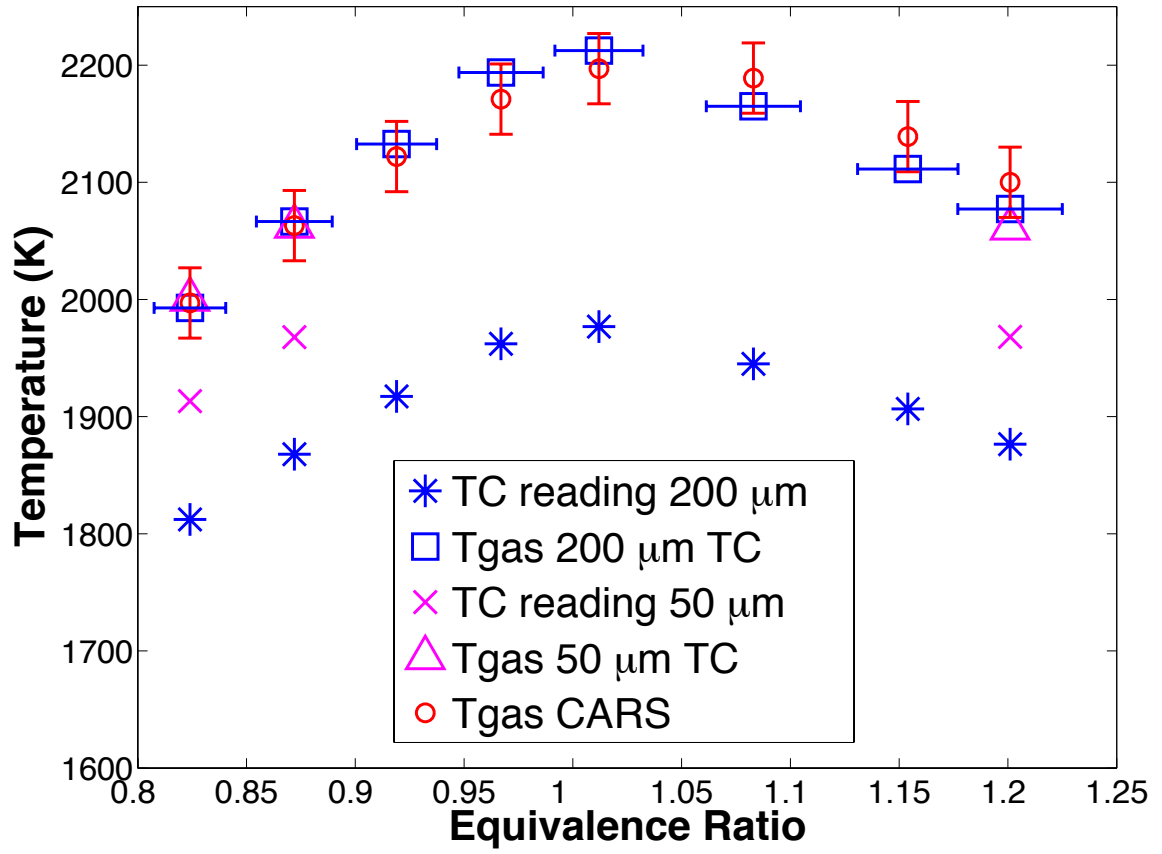
Fig. 3.6. Comparison of thermocouple measurements and CARS measurements.

Color-ratio TFP was also assessed in the calibration flame. Color images of the glowing SCS-9A fiber at eight equivalence ratios were taken. Signal ratios were determined from the three color channels through post processing and used to infer temperature. In Fig. 3.7, the measured fiber temperatures are shown as blue asterisks, the derived gas temperatures after radiation correction are shown as red squares. They agree very well with the CARS measurements as shown by the red circles.
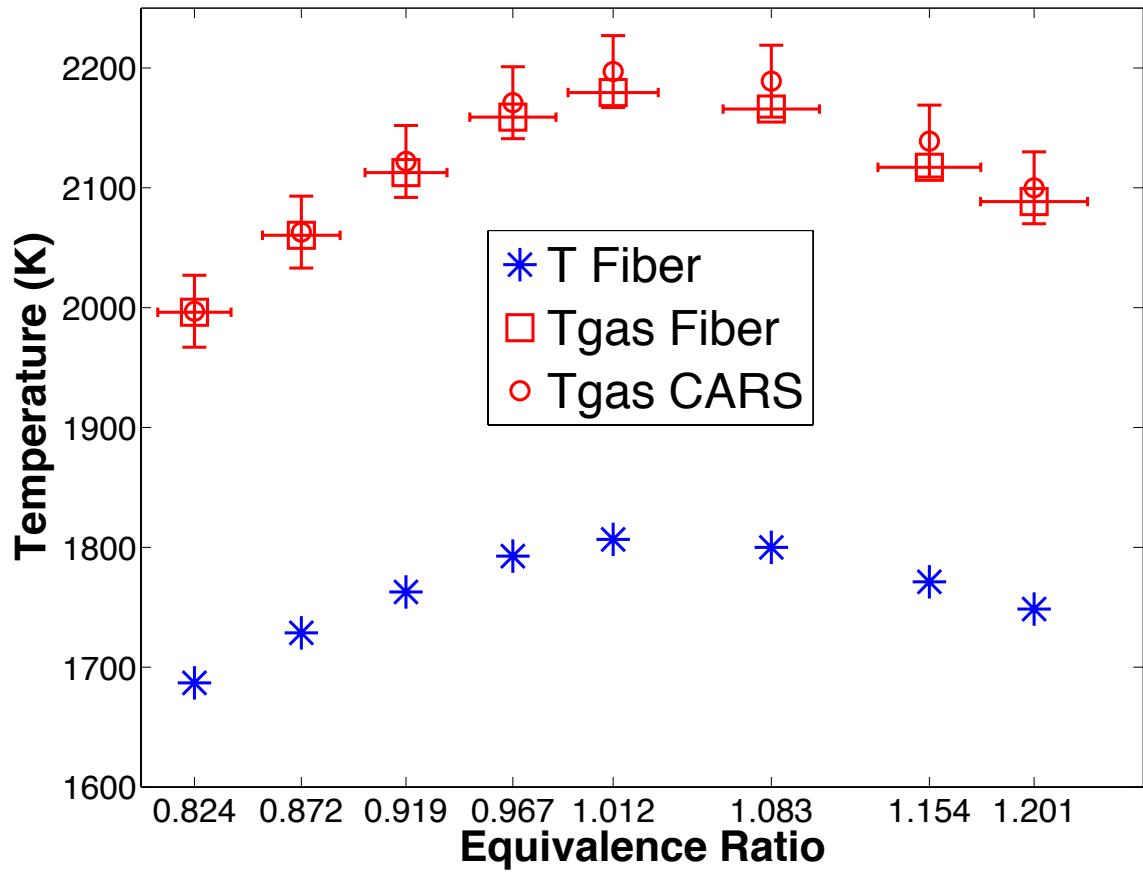
Fig. 3.7. Comparison of color-ratio TFP and CARS measurements.

3.5 Uncertainty analysis

Uncertainty analysis has been performed and can serve as an effective guide to interpreting results and reducing errors. In particular, the uncertainties of both T_f and ΔT were considered. T_f uncertainty was analyzed for both intensity-ratio and color-ratio approaches. For the intensity-ratio approach, after rearranging Eq. (3.2.1), T_f can be obtained by Eq. (3.5.1). The accuracy of T_f is dependent on the accuracy of the calibration temperature T_0 and the intensity-ratio I_R. Error propagation was used to estimate the T_f uncertainty as shown by Eq. (3.5.2). The T_0 uncertainty δT_0 is largely dependent on the quality of calibration. In particular, it relates to how well the calibration flame is characterized and how well the thermocouple is manufactured if it is used for temperature calibration. Under an ideal case such as the calibration condition presented in this work, $\delta T_0/T_0$ can be estimated to be $\sim 1\%$. The I_R uncertainty $\delta I_R/I_R$ is dependent on the aging behavior and, to a lesser extent, the measurement noise of the detector. From the aging test, $\delta I_R/I_R$ was seen to be as large as 22% for an unstable fiber and as small as 5% for a stable fiber. Under the condition where the reference temperature $T_0 = 1820$ K and detection wavelength $\lambda = 673$ nm, by using a stable fiber rather than an unstable fiber, the overall δT_f based on the intensity-ratio approach is improved to ~ 15 K from ~ 32 K.

$$T_f = \left(\frac{1}{T_0} - \frac{\lambda}{C_2} \ln I_R \right)^{-1} \qquad (3.5.1)$$

$$\delta T_f = \sqrt{ \left(T_0 \frac{\partial T_f}{\partial T_0} \frac{\delta T_0}{T_0} \right)^2 + \left(I_R \frac{\partial T_f}{\partial I_R} \frac{\delta I_R}{I_R} \right)^2 } \qquad (3.5.2)$$

For the color-ratio approach, the accuracy is mainly dependent on how well the fiber behaves as a greybody, as the greybody assumption is used to calculate the color ratio and temperature lookup table. From the aging test and spectral emissivity measurements, the 75 μm SCS-9A and 14-μm ceramic grade fiber showed relatively good greybody behavior and stability. By measuring the fiber temperature above the stable flat premixed flame using the color-ratio approach, the SCS-9A showed ~ 30 K variation over 7 hours and the ceramic grade fiber showed ~ 50 K variation over 90 minutes. The change in temperature is due to the change of greybody behavior. Thus, the uncertainty δT_f is estimated to be ~ 30 K and ~ 50 K for SCS-9A fiber and ceramic grade fiber respectively. It should be noted that larger variations are expected for unstable fibers.

Beyond fiber temperature, the uncertainty of the radiation correction must also be considered. The radiation correction ΔT can be calculated by Eq. (3.5.3) and its associated uncertainty is expressed by Eq. (3.5.4) from error propagation. The notations for each item have been previously explained in Eq. (3.2.2)-(3.2.4) and are not repeated here. For error propagation, only parameters containing the largest uncertainties are considered. Fiber diameter and ambient temperature in lab conditions can be accurately measured and are not considered in the error analysis.

$$\Delta T = T_{gas} - T_f = \frac{1}{Nu}\frac{\sigma\varepsilon(T_f^4 - T_a^4)D_f}{k_{gas}} \quad (3.5.3)$$

$$\delta\Delta T = \sqrt{\left(k_{gas}\frac{\partial\Delta T}{\partial k_{gas}}\frac{\delta k_{gas}}{k_{gas}}\right)^2 + \left(Nu\frac{\partial\Delta T}{\partial Nu}\frac{\delta Nu}{Nu}\right)^2 + \left(T_f\frac{\partial\Delta T}{\partial T_f}\frac{\delta T_f}{T_f}\right)^2} \qquad (3.5.4)$$

For k_{gas} and Nu estimation, hot gas velocity, gas composition and temperature need to be estimated or numerically simulated. Fiber surface temperature uncertainty δT_f is generally better than $\sim$ 30 K if a stable greybody fiber is used. Given the conditions T_f = 1700 K, T_a = 298 K, Nu = 1, D = 75 μm, k_{gas} = 0.15 W/(m·K) and ε = 0.88, with an estimation of $\delta k_{gas}/k_{gas}$ and $\delta Nu/Nu$ to be 10%, $\delta T_f/T_f$ to be 1.8%, $\delta\Delta T$ is calculated to be $\sim$ 33 K. Considering the contribution of uncertainties of both fiber temperature and radiation correction as shown by Eq. (3.5.5), the overall intensity-ratio- and color-ratio-based flame temperature uncertainties are estimated to be 36 K and 45 K respectively.

$$\delta T_{gas} = \sqrt{\delta T_f^2 + \delta\Delta T^2} \quad (3.5.5)$$

It should be noted that the above uncertainty analysis is meant to set up a framework and provide estimation based on the conditions specified above. For other measurements, uncertainty should be analyzed for the specific conditions. Nevertheless, the above analysis could still provide certain insight on reducing measurement uncertainties. For example, there seems to be more room to reduce ΔT uncertainties than T_f uncertainties. As can be seen from Eq. (3.5.3), ΔT is proportional to $1/Nu$ and fiber diameter D_f. Therefore, by using smaller D_f and bigger Nu, ΔT and its associated uncertainty can be effectively reduced. A simulation has been performed to show the effect of Nusselt number and fiber diameter on the calculated ΔT as shown in Fig. 3.8.

For measurements in a one-atmosphere lab scale flame, the Nusselt number is of unity order, ΔT is as large as 300 K as seen in both the previous measurements and the simulation. However, at high Nusselt number, where the pressure and gas velocity are high, the radiation correction and its uncertainty are much smaller. This indicates that the TFP approach potentially has better accuracy and may be a promising technique for temperature measurement at high-pressure, high-speed environments. Similarly, using smaller fibers also yields a small radiation correction as indicated by the simulation. However in real situations, small fibers are less able to survive in harsh environments than larger ones and tradeoffs must be made in choosing the proper fibers.
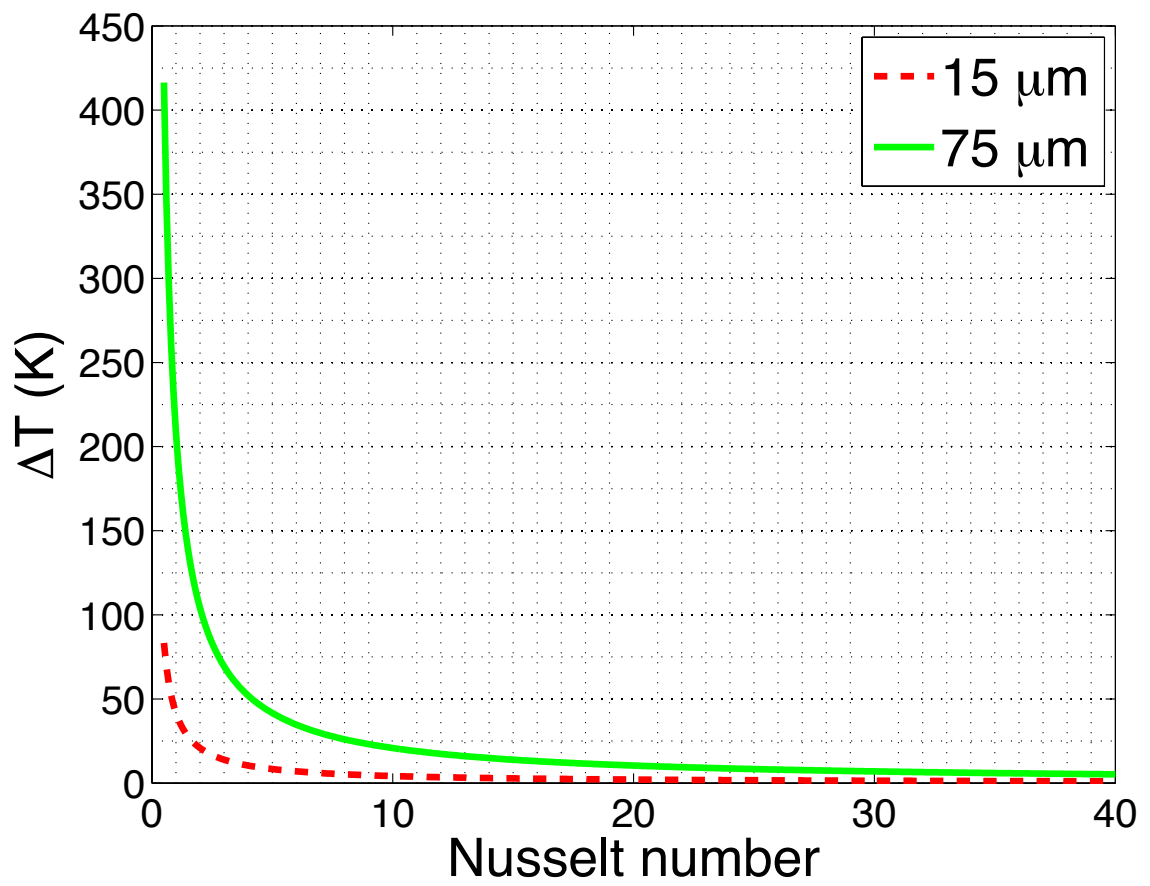
Fig. 3.8. A simulation of Nusselt number and fiber diameter vs. calculated ΔT

3.6 Conclusions

Recent developments on thin-filament pyrometry have been discussed. The physical backgrounds of intensity-ratio and color-ratio approaches have been reviewed and discussed, along with the radiation correction procedure. Associated error sources have been identified and investigated in detail. Fiber aging tests and spectral emissivity measurements have been conducted on six different types of SiC fibers, including frequently used ~ 14 μm fibers and new fibers with diameter above 75 μm; two kinds of fibers (14 μm CG-Nicalon and 75 μm SCS-9A) were found to have better optical stability and greybody behavior, and are recommended for use in TFP measurements. Thermocouples with cylindrical junctions were also manufactured and are recommended for the intensity-ratio approach calibration, and temperature measurements in general. Confidence in thermocouple measurements in relatively simple flames was established through direct comparison with reference temperatures based on CARS measurements. The intensity-ratio and color-ratio approaches to determine fiber temperature and radiation correction procedure have also been directly compared with reference temperatures based on CARS measurements, and very good agreement has been achieved under well-characterized conditions. TFP measurement errors have also been analyzed through uncertainty analysis. It is suggested that for high-pressure, high-speed flows, the radiation correction can be performed with much smaller uncertainty compared to one-atmosphere lab scale conditions, and therefore, the TFP approach could be a promising tool for temperature measurement in high Nusselt number conditions.

4   The microgravity projects SLICE and CLD flame

4.1   Introduction

While normal gravity combustion studies can provide important information on combustion processes, conducting the experiment in a microgravity environment has the advantage that buoyancy effects are eliminated, which simplifies the interpretation of both computational and experimental results. In addition, the microgravity environment will enable the stabilization of flames with increased levels of dilution and will help generate flames that have increased soot residence times compared to normal gravity facilities. In general, microgravity is an ideal condition to eliminate complexities and provide 'cleaner' tests to refine the current computational model. Yale is responsible for two International Space Station- (ISS) based microgravity combustion projects, namely Structure and Liftoff In Combustion Experiments (SLICE) and Coflow Laminar Diffusion (CLD Flame). My work is involved in preparing and conducting the SLICE project that was completed in March 2012 and preparing for the CLD Flame project that will take place in 2016, by utilizing the newly developed optical techniques described in Chapters 2 and 3.

As a precursor to the CLD Flame project, the goal of SLICE was to investigate coflow laminar flames under a wide spectrum of dilution from near extinction to heavily sooting conditions. The results can provide a test case for developing the computational model and soot sub-model, and also can be used to minimize risk and maximize the scientific return of the CLD Flame experiment. The SLICE project was completed on board the ISS. Collectively, over 100 tests were conducted and over 4,000 high-

resolution digital photographs were taken. Those 14-megapixel photos included roughly 700 bracketed sets of flames photos. The data quality was high with the exception that the flame images revealed a flow asymmetry, presumably in the coflow (and not the fuel flow) that caused the lifted flames to be always tilted. The discussion of SLICE will be covered in Section 4.2.

Our CLD Flame experiment is one of the four investigations that make up Advanced Combustion via Microgravity Experiments (ACME). The experiments in ACME are currently in development for conduct within the Combustion Integrated Rack (CIR) on the ISS. Due to the limitations of the facilities onboard the ISS, the CLD Flame experiment in the Combustion Integrated Rack (CIR) cannot be actively vented during burning. Therefore, the combustion process will undergo an increasing pressure, which will complicate the interpretation of gravitational effects and computational modeling, unless this pressure effect is understood and quantitatively characterized. Pressure plays an important role in many practical devices (e.g., internal combustion engines and rocket engines), and it is also an important factor that controls the combustion process with fundamental scientific research interest. The previous studies in our lab were all conducted under atmospheric pressure and the ability to model combustion process under elevated pressure has not been examined. Given the importance and the insufficient knowledge of the pressure effect, quantitative measurements of temperature and flame structure are highly desired. Therefore an experimental and computational combined study has been carried out for our coflow laminar diffusion flame in an elevated-pressure chamber. The details are given in Section 4.3.

4.2   The SLICE project

4.2.1   Soot formation in microgravity

Microgravity is a unique environment in which to study combustion. The absence of buoyancy results in a simplified flow field that can serve as a "cleaner" test case to develop computational models. Highly diluted flames that extinguish in normal gravity can be stabilized in microgravity, which enables study of flames near extinction. Sooty flames with enhanced residence time can be also generated, which can be used to study soot formation mechanisms. In general, the contrasting effects in normal and microgravity provide an excellent test case for developing an improved understanding of the factors that affect flame lift-off distance, extinction, and soot formation mechanisms. To better understand the factors that affect flame extinction and particulate formation, flames were investigated in the SLICE experiment on board the ISS. Although the SLICE experiment studied flames with a wide dilution spectrum from weak to highly sooting flames, the work described here emphasizes the sooting behaviors of coflow jet flames in microgravity and normal gravity. The effect of gravity on soot formation has been studied over the past few decades. Experimentally, Greenberg *et al.* [Greenberg 1997b] conducted a reduced-gravity experiment in a 2.2 s drop tower, and reported the first 1-g and 0-g comparison of soot volume fraction for laminar acetylene and nitrogen-diluted acetylene jet diffusion flames. A factor of 2 to 4 increase in peak soot volume fraction was reported from 1-g to 0-g. Walsh *et al.* [Walsh 2000b] found that the laser induced incandescence (LII) signal of a methane coflow laminar diffusion flame increased by a factor of 15 during a parabolic flight. Jeon and Choi [Jeon 2010] studied the buoyancy effect on soot formation in a gas-jet diffusion flame in partial gravity conditions from

0.3-g to 1-g. The soot volume fraction was measured by extinction and found to increase with reduced gravity level. Riemann *et al.* [Reimann 2010] performed LII in a drop tower, measuring both soot concentration and primary particle size. In microgravity, the soot is concentrated in small bands and the maximum particle size is roughly double compared to the 1-g case. Diez *et al.* [Diez 2009] studied the properties of non-buoyant, laminar jet diffusion flames during Space Shuttle Columbia flights and showed the existence of a soot property-state relationship for such flames. Computationally, Kaplan *et al.* [Kaplan 1996] simulated an ethylene-air diffusion flame and found that the peak soot volume fraction increased by a factor of 10 from 1-g to 0-g. Their simulation did not reach steady-state conditions until approximately 3 s of microgravity. This result indicates that flames may not become stabilized in short-duration drop tower experiments. Kong and Liu [Kong 2009] recently simulated laminar coflow methane/air diffusion flames and studied the effects of air coflow velocity. The peak soot volume fraction in microgravity was found to be about twice that in normal gravity [Kong 2010]. Liu *et al.* [Liu 2011] computed the influence of heat transfer and radiation on the structure and soot formation characteristics of a coflow laminar ethylene/air diffusion flame and showed that radiation heat loss plays a major role in the flame structure in microgravity. Charest *et al.* [Charest 2011] recently simulated the influence of gravity on a laminar coflow methane/air diffusion flame, demonstrating that the 0-g flame has a lower gas temperature, thicker soot regions and higher soot volume fractions than the 1-g flame.

Although significant experimental efforts have been made on studying gravitational effects on soot formation, there are some uncertainties and complications

associated with experiments. For example, flames in short-duration drop tower experiments are often not fully stabilized; on the other hand, the gravitational-jitter in parabolic flight can disturb low-momentum flames, affecting the accuracy of the measurements. Furthermore, the experimental results are quite limited due to the sheer cost of microgravity experiments. Previous computational work has been done, but no direct comparison between experiment and computation for microgravity flames was available. The SLICE experiment is a joint experimental and computational study. The microgravity experiment was conducted in the Microgravity Science Glovebox (MSG) on board the ISS, which provides a stable microgravity environment for conducting long-duration experiments, by crewmember Dr. Donald R. Pettit in 2012. The normal gravity SLICE experiment was performed at Yale, using an engineering unit, which is a replica of the SLICE flight hardware. Detailed near-field velocity measurements performed on the engineering unit guided the boundary conditions used in the computations. In the following sections, two-dimensional comparisons of 1-g and 0-g soot temperature and volume fraction are presented from both experiment and computation.

4.2.2   SLICE experimental setup

The SLICE experimental setup was housed in the MSG and a fish-eye view is shown in Fig. 4.1. A digital single lens reflex camera (Nikon D300s), an analog video camera and the SLICE hardware and their associated control box and cables can be seen. A close up photograph of the SLICE hardware is shown in Fig. 4.2. It was originally used in the Enclosed Laminar Flames (ELF) investigation [Brooker 1999] to study the effect of buoyancy on the stability of coflow gas-jet diffusion flames during the STS-87 Space Shuttle mission. A schematic drawing of the SLICE burner inside the hardware is shown

95

in Fig. 4.3. The duct has a 76 mm × 76 mm square cross-section with rounded corners and is 174 mm tall. The central fuel jet tube has a threaded base that allows five nozzles with 0.4064, 0.764, 1.600, 2.100 and 3.200 mm inner diameter to be attached. The fuels investigated in the SLICE experiment included 100% CH_4, 70% CH_4, 40% CH_4, and 20% C_2H_4 (by volume) diluted with N_2. High purity CH_4 and C_2H_4 were used. The fuel flow rate was controlled by a mass flow controller and could be adjusted manually in the range of 0-500 sccm N_2 equivalent flow. These test conditions cover a wide range of flame conditions from weak, lifted flames near extinction to strongly sooting flames.
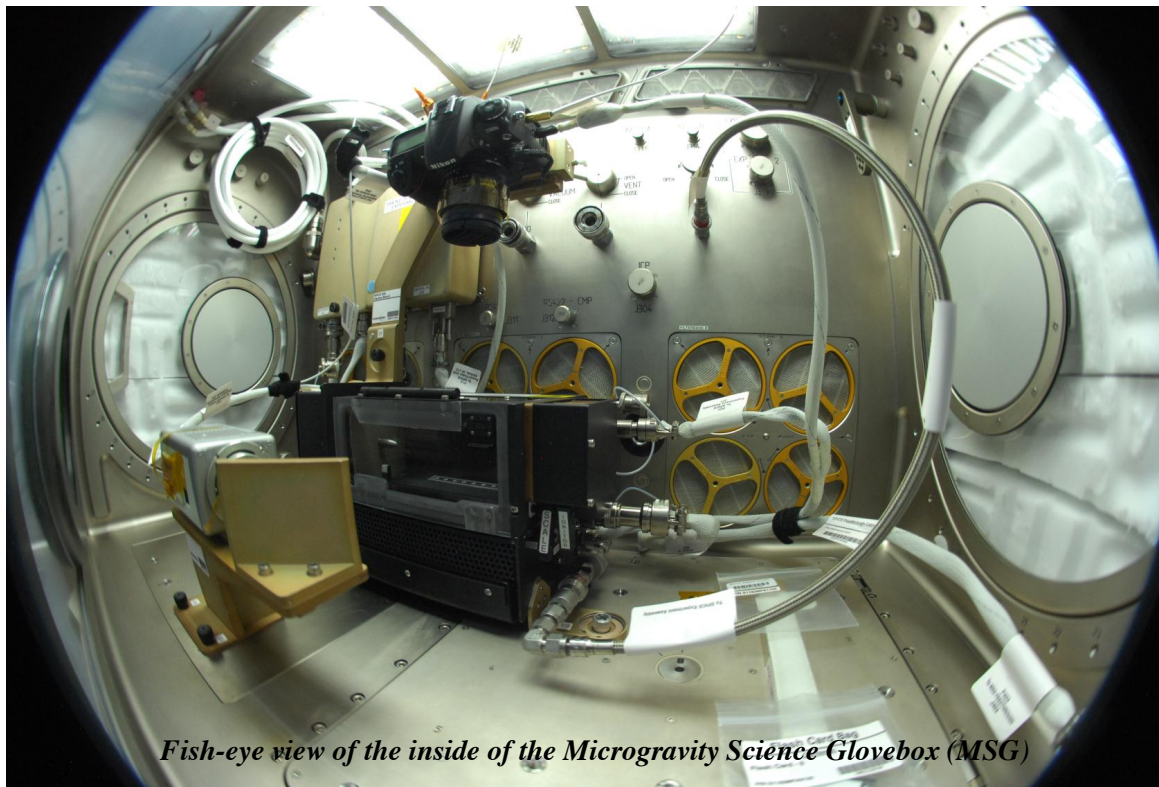
Fish-eye view of the inside of the Microgravity Science Glovebox (MSG)

Fig. 4.1. A fish-eye view of the SLICE experimental setup in the microgravity science glovebox on board the international space station.

96

Fig. 4.2. A photograph of the SLICE hardware
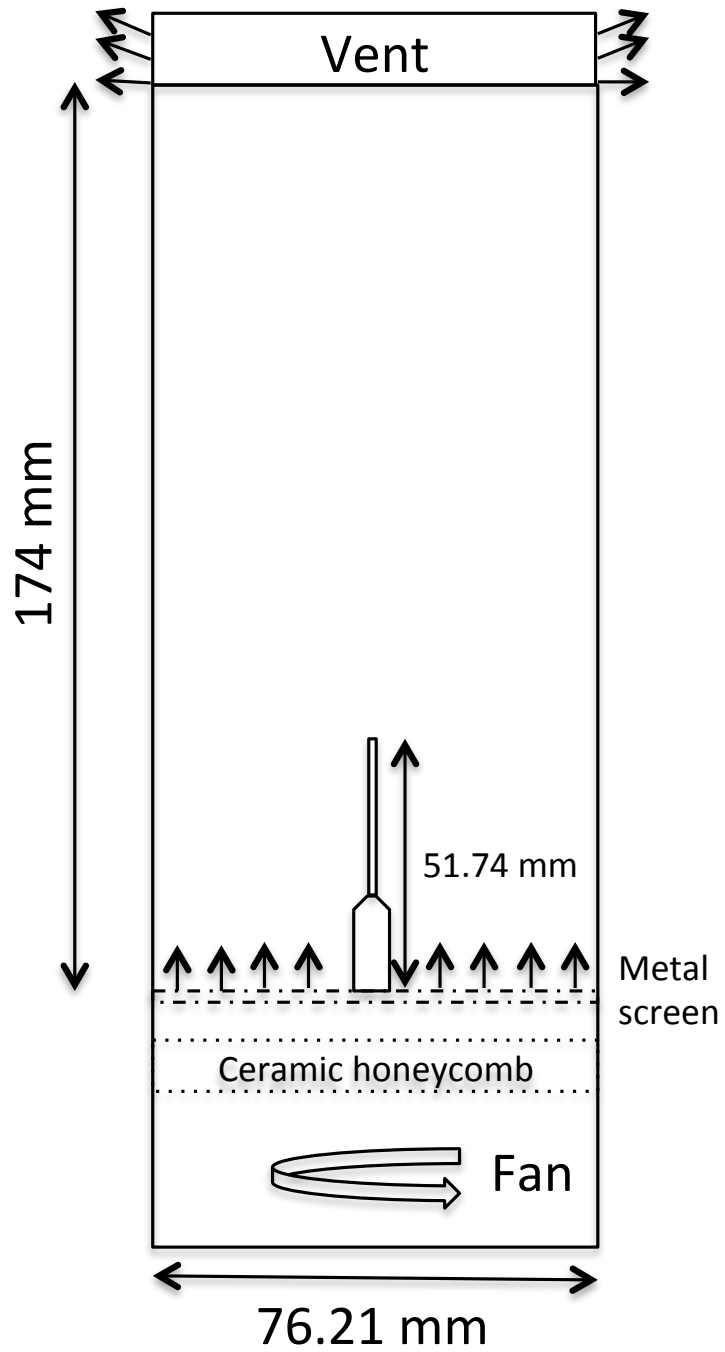
Fig. 4.3. SLICE burner configuration.

As shown in Fig. 4.3, coflow air is supplied by a DC fan located at the upstream end of the duct. The coflow air passes through a honeycomb and a mesh screen to straighten the flow and flatten the velocity profile before entering the duct. The coflow air velocity can be varied by changing the fan voltage. A calibrated hot-sphere anemometer was placed between the honeycomb and the mesh screen to monitor the local air velocity. The flow field of coflowing air has been measured at different fan voltage levels using a thin (~ 3.8 μm) hot-wire anemometer 1 mm above the fuel nozzle by scanning through the radius of the duct. The scanning step is 2 mm at far field where the coflow velocity gradient is small and 0.5 mm close to the burner where the gradient is large. The measured velocity profiles are shown in Fig. 4.4. Due to imperfections in the setup, the coflow near the fuel nozzle is not strictly symmetric. The measurement on the engineering unit was used to establish the boundary condition for the computations. Although the flight and engineering units are very similar and steps were taken to match conditions as closely as possible between the two, differences in the details of the velocity profiles of the two pieces of hardware are possible. In comparing results between normal gravity and microgravity, as well as between measurements and computations, these uncertainties should be kept in mind.
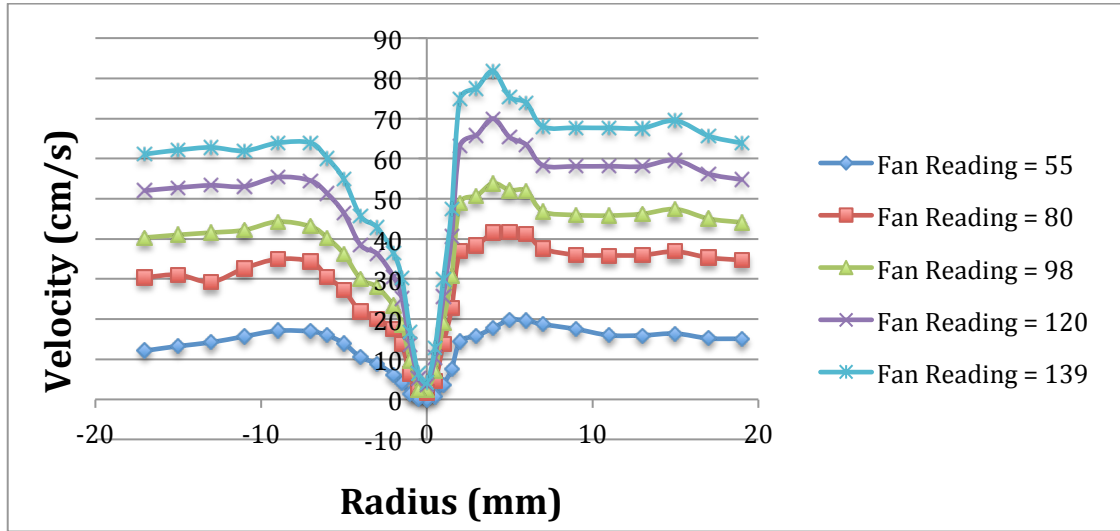
Fig. 4.4. Velocity profile of coflowing air at various fan settings.

An analog color video camera was used to monitor the flame behavior. The test conditions including fuel flow rate, fan setting, anemometer reading and a timer were superposed on the video as shown in Fig. 4.5. Still images were taken by a digital single lens reflex camera (Nikon D300s) with a 2 mm BG-7 filter attached in front of the lens. The filter was used to balance the red, green, and blue (RGB) channels of the acquired color images. The test procedure involved manually setting the desired flow conditions and taking images in bracket mode of 5 or 7 frames to ensure unsaturated images were obtained. The camera exposure time and f number were set according to the test matrix, which is made based on the experience accumulated through several ground tests before the actual experiment. Given the large amount of data and relatively long-time experimental operation, an optical character recognition algorithm was used to analyze the video to automatically obtain the flow conditions and time from the video display.

The algorithm analyzed the region where there is a character, and determined the characters by finding the maximum 2-D correlation with comparison of target character images stored in the library. For each still image captured by the Nikon camera, the test conditions were determined by matching the video time to the image time available in the EXIF (EXchangeable Image Format) data, which can be read out by OMA. As shown in Fig. 4.6, the data images were organized by their fuel types, burner sizes and flow conditions in an excel spreadsheet, where other information such as the maximum signal values in each of the RGB channels, the flame images, and their corresponding soot temperature and volume fraction are also available for preview.

Fig. 4.5. SLICE real-time flame monitor screen and display of experimental conditions

F #	Rmax	Gmax	Bmax	Fuel	Air	Fan	Rad	Frame #	Saturation	Burner	BG filtered Images	Temperature (T =[1400 2000])	055_forHSV_splice_images
7.1	3818.91	16150.8	7984.98	135	23	75	0.85	9967	0	2.1			
5	7191.63	30014.1	14869.4	136	23	75	0.81	9998	0	2.1			
2.5	27941.1	61533.9	57029.5	136	23	75	0.81	9998	1	2.1			
2	51556.5	62885.5	65535	136	23	75	0.81	9998	1	2.1			
2	51739.1	62886.4	65535	134	23	74	0.81	10023	1	2.1			
3.5	15131.1	61648	30627.2	202	35	95	1.35	15779	1	2.1			
11	1444.21	6004.27	2915.53	202	34	94	1.35	15804	0	2.1			
8	3304.11	13890.3	6812.9	202	34	94	1.35	15804	0	2.1			
5.6	6851.24	28132.2	13810.7	202	34	95	1.35	15835	0	2.1			
2.5	27689	61537.8	55629.4	202	34	95	1.35	15835	1	2.1			
2	53686.2	62890.6	65535	202	34	95	1.35	15835	1	2.1			
2	54514.4	62890.1	65535	196	34	95	1.25	15867	1	2.1			
4	16032.7	62237.5	33829.7	181	34	95	1.05	16318	1	2.1			
11	1708.38	7300.26	3621.05	181	34	95	1.05	16318	0	2.1			
7.1	3918.55	16664.6	8327.26	181	34	95	1.05	16349	0	2.1			
5.6	7606.58	31837.8	15954.2	181	34	95	1.05	16349	0	2.1			
2.5	31880.5	61537.4	65033.8	180	34	95	1.05	16374	1	2.1			
2	61411.9	62890.5	65535	180	34	95	1.05	16374	1	2.1			
2	59341.9	62889.8	65535	180	34	95	1.05	16374	1	2.1			
4.5	9911.66	41208	20593.9	258	46	122	1.65	17728	0	2.1			
13	1043.23	4390.18	2132.98	257	46	122	1.75	17760	0	2.1			
9	2503.59	10527.1	5168.4	257	46	122	1.75	17760	0	2.1			
6.3	5241.09	21772	10756.5	257	46	122	1.75	17760	0	2.1			
3.2	18813.5	62682.3	38030.7	258	46	121	1.65	17785	1	2.1			
2.2	49619.2	62441.2	65535	258	46	121	1.65	17785	1	2.1			
2	58453	62892.8	65535	258	46	121	1.65	17785	1	2.1			
4.5	14053.7	59467.6	30740.7	211	46	123	1.15	18180	0	2.1			
13	1294.98	5661.62	2896.01	211	46	122	1.15	18205	0	2.1			
9	3210.18	13820.4	7083.93	211	46	122	1.15	18205	0	2.1			
6.3	6342.04	27199.6	13948.8	211	46	122	1.15	18205	0	2.1			
3.2	23728.8	62681	52152	209	46	122	1.15	18236	1	2.1			
2	65535	62890.1	65535	209	46	122	1.15	18236	1	2.1			
2	65535	62884.6	65535	209	46	122	1.15	18236	1	2.1			

Fig. 4.6. A screen shot of the test conditions organized in a spreadsheet for quick preview.

4.2.3 Soot diagnostics

The measurement of soot temperature used a ratio-pyrometry approach. Detailed information can be found in Chapter 2 and [Kuhn 2011], with only a brief description presented here for completeness. In order to obtain quantitative temperature data, the Nikon D300s is fully characterized as a ratio pyrometer as discussed in Chapter 2. The soot emissivity was assumed to vary as $\lambda^{-1.38}$ to calculate the temperature/color-ratio lookup table. The data analysis was performed by the open source image-processing software OMA [Kalt 2013]. Each flame image was separated into three RGB images and then converted to radial profiles using an Abel inversion. Dividing the radial profiles by each other to determine the measured signal ratios and applying the soot lookup table gives three soot temperature profiles, with a maximum variation of ~ 30 K. The final temperature is an average of the three. Once the soot temperature is determined, the soot volume fraction can be obtained through an absolute light intensity calibration. Absolute light intensity calibration is used to quantify the geometric factors and optical transmission associated with the specific setup. While the traditional calibration sources such as a blackbody source or a tungsten lamp cannot fit in the SLICE duct due to their size, a small S-type thermocouple can be placed into the duct above the flame. The incandescence of the flame-heated thermocouple with known emissivity model and measured temperature was used as a calibration source. The details of the calibration procedure is available in Chapter 2 and [Ma 2013].

4.2.4 Computational approach

The numerical simulation was performed by Professor Smooke's group. The computational model used here is similar to the one as discussed in Section 2.2.6.

Specifically, the sectional soot model is included to simulate soot in the 70% CH_4 and 100% CH_4 flames. The gas-phase chemistry employed here is the GRI 3.0 mechanism [Smith 1999] with all nitrogen-containing species (except N_2) removed. In order to simulate sooting process, a series of reactions related to the formation and oxidation of benzene and related species were included (see Table 1 of [Hall 1997]), with the resulting mechanism having 42 species and 250 reactions.

A new mass-conserving, smooth vorticity-velocity formulation [Cao in preparation] of the governing equations is adopted, which consists of the elliptic radial velocity equation, an updated elliptic axial velocity equation, given by

$$\frac{\partial^2 v_z}{\partial r^2} + \frac{\partial^2 v_z}{\partial z^2} = -\frac{\partial \omega}{\partial r} - \frac{\omega}{r} - \frac{1}{r}\frac{\partial v_z}{\partial r} - \frac{\partial}{\partial z}\left(\frac{v \cdot \nabla \rho}{\rho}\right) \qquad (4.1)$$

the vorticity transport equation, the energy conservation equation, and $N_{species}$ balance equations for the mass of each gaseous species. To ensure that the mass fractions sum to unity, the species equation for nitrogen is replaced by $Y_{N_2} = 1 - \sum_{n \neq N_2} Y_n$.

The square duct was approximated as an axisymmetric coaxial tube with an identical cross-sectional area. Each flame is assumed to be axisymmetric despite certain asymmetry at the base of the flame, so a two-dimensional computational domain is employed, extending radially to r = 4.288 cm and axially to z = 12.2 cm. The grid on the axisymmetric domain is a non-uniform tensor product mesh initially containing 67 points in the r direction and 75 points in the z direction. After solving the flames on a series of finer grids, the grid used in all results presented here is a 186 × 206 mesh. The grid points

are clustered towards the burner surface and the centerline in order to capture the sharp gradients in these regions. Specifically, the mesh is uniformly spaced with $\Delta r = 0.01$ cm for $0 \le r \le 1.5$ cm, with increasingly larger spacing for $1.5 < r \le 4.288$ cm; it is also uniformly spaced with $\Delta z = 0.03$ cm for $0 \le z \le 5.1$ cm, with increasingly larger spacing for $5.1 < z \le 12.2$ cm.

The governing equations and boundary conditions were then discretized on this tensor product grid via standard nine-point finite difference stencils, which are second-order accurate in the regions of the grid that are equispaced and are between first- and second-order accurate elsewhere. The resulting set of fully coupled, highly nonlinear equations is then solved simultaneously at all grid points using a damped modified Newton's method [Deuflhard 1974; Smooke 1983] with a nested Bi-CGSTAB linear algebra solver [Van der Vorst 1992]. To aid in convergence of Newton's method, pseudo-transient continuation is performed until the adaptively chosen pseudo-time step exceeds a cut-off value, after which the steady-state equations are finally solved to a Newton tolerance of 10^{-5}. The first flame to be modeled is a 65% CH_4 flame under normal gravity, because it was studied in our previous investigations (e.g., [Walsh 2000b; Walsh 2005; Bennett 2008]). The converged solution of this flame is then employed in a continuation technique whereby the inlet conditions and the gravitational acceleration are slowly changed. After each incremental change in the flame parameters, the governing equations and boundary conditions are re-solved, ultimately producing converged solutions for the flames at microgravity and/or having different N_2 dilution levels.

4.2.5 Results and discussion

A 100% CH_4 flame using 3.2 mm ID nozzle with average fuel velocity of 46 cm/s

and air coflow of 15 cm/s was measured at 1-g and 0-g. The measured soot temperature and volume fraction are shown in the top row of Fig. 4.7. In 0-g, a taller and wider flame was produced and the peak soot volume fraction increased by a factor of 6. The enhanced soot production resulted in increased thermal radiation losses and hence reduced flame temperatures. The peak soot temperature in 0-g is shown to be ~ 200 K lower than its 1-g counterpart. From 1-g to 0-g, the peak of soot volume fraction was also redistributed from the flame centerline to the wings. The soot growth mode is believed to change from an inception-dominated mode to a surface-growth-dominated mode [Smooke 2005]. A preliminary computational simulation was also carried out for the flame. The simulated soot temperature and volume fraction of the same flame are shown in the bottom row of Fig. 4.7. From 1-g to 0-g, the flame becomes taller and wider with increased soot volume fraction. This trend agrees with the experimental observation. On the soot volume fraction map, residence time contours are also superimposed. The residence time in milliseconds is determined based on the simulated axial and radial velocities as shown in Fig. 4.8. Due to the buoyancy effect, the hot flow under 1-g is accelerated and the maximum velocity is up to ~ 200 cm/s at the far downstream location, while the 0-g counterpart is only ~ 90 cm/s at the upstream location around the tip of the burner. The reduction in axial velocity results in longer residence times as can be seen from Fig. 4.7. This allows more time for soot particles to grow and results in enhanced soot volume fraction. The preliminary simulation qualitatively captures the trend. However, the agreement on the absolute quantities between experiment and computation is not very good.
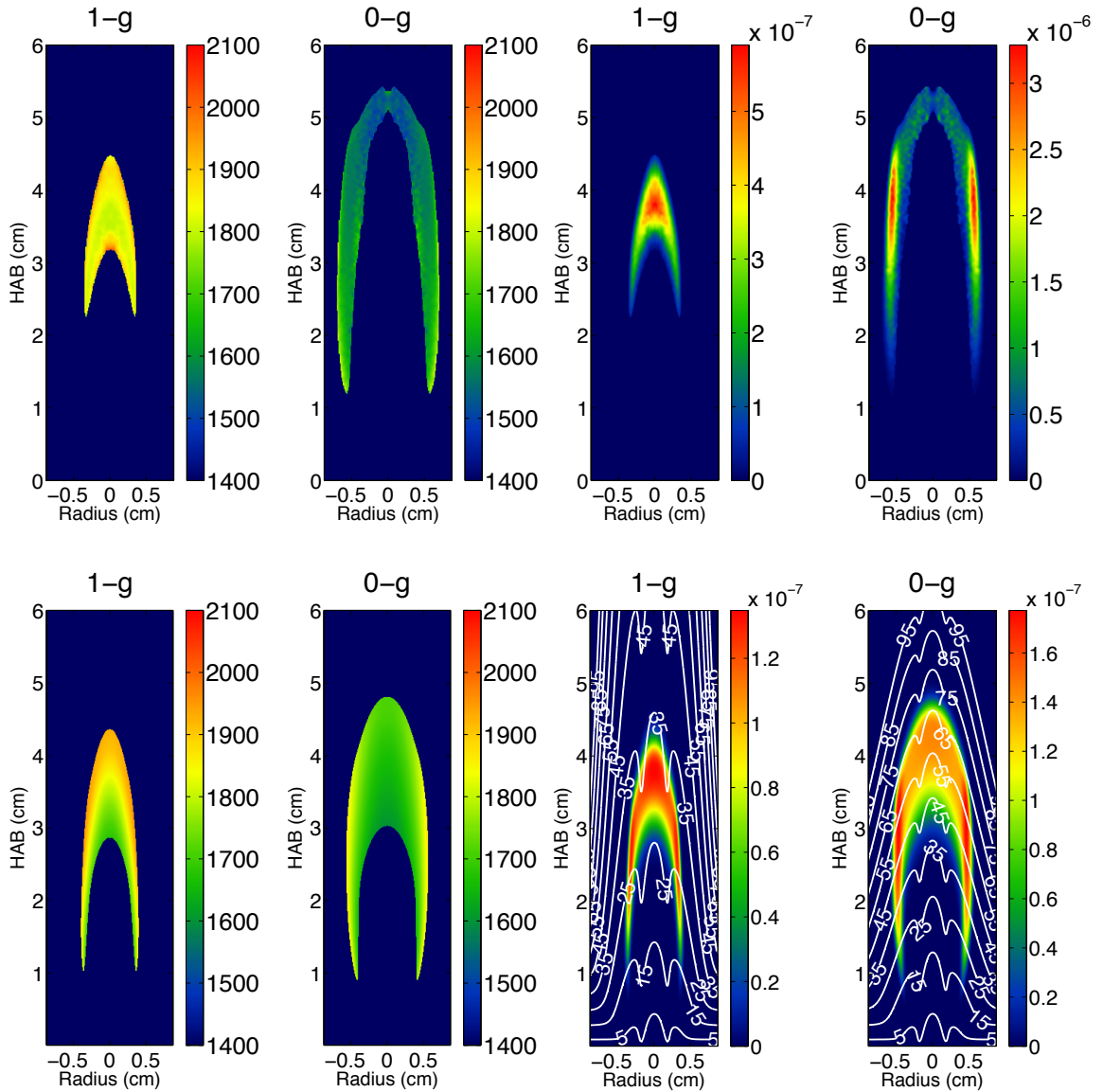
Fig. 4.7. 1-g and 0-g measured (top) and computed (bottom) soot temperature comparison (left) and soot volume fraction comparison (right). 100% CH$_4$ flame with 3.2 mm ID nozzle. Average fuel speed is 46 cm/s and coflow speed is 15 cm/s. Residence time contours (milliseconds) are superimposed on the calculated soot volume fraction maps.
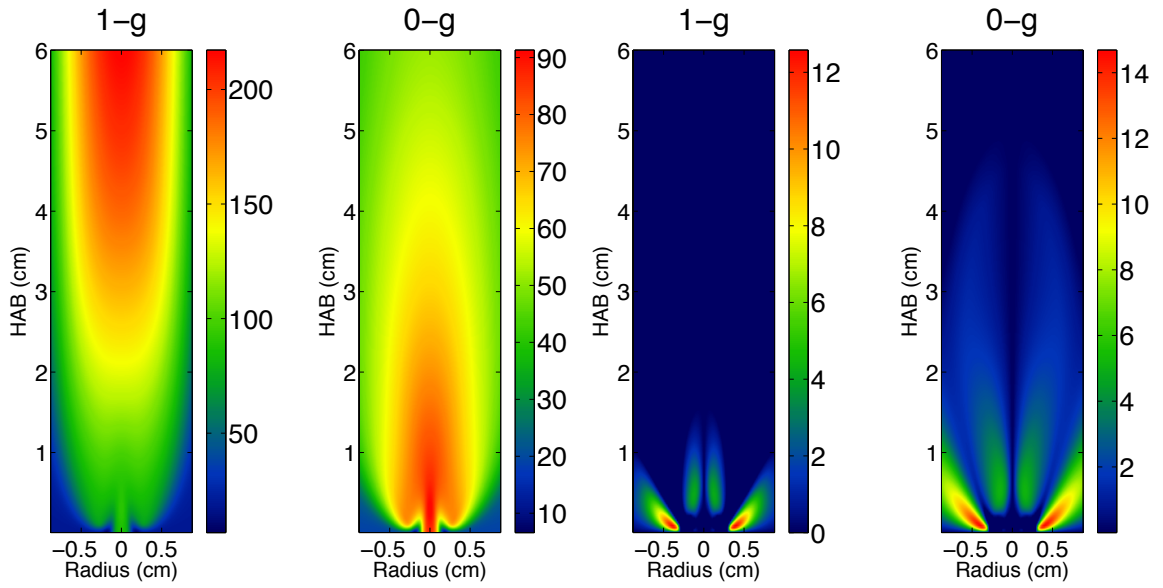
Fig. 4.8. 1-g and 0-g computed axial velocity comparison (left) and 1-g and 0-g radial velocity comparison (right) [cm/s]. 100% CH_4 flame with 3.2 mm ID nozzle. Average fuel speed is 46 cm/s and coflow speed is 15 cm/s.

In other experiments, the fuel velocity was increased to 169 cm/s by using a 1.6 mm ID nozzle while the coflow velocity was kept unchanged at 15 cm/s. Experimental and computational results for this condition are shown in Fig. 4.9. Experimental results for soot temperature and volume fraction at 1-g and 0-g are shown in the top of Fig. 4.9, and the corresponding computational results are shown in the bottom of Fig. 4.9. The axial and radial velocities are also numerically simulated and are shown in Fig. 4.10. Very similar trends have been observed, such as higher soot volume fraction in 0-g, and soot peaks on the wings in 0-g.
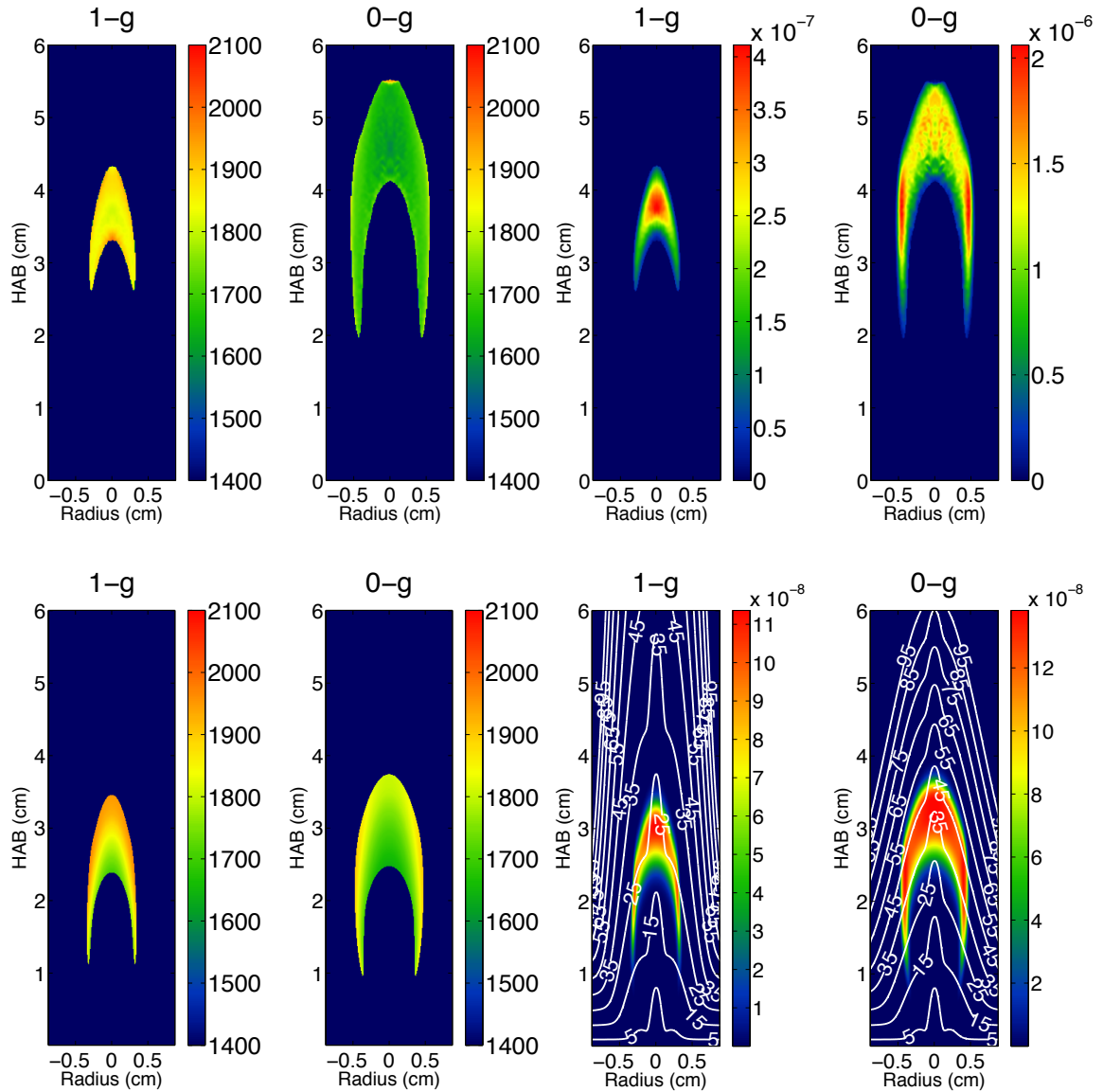
Fig. 4.9. 1-g and 0-g measured (top) and computed (bottom) soot temperature comparison (left) and soot volume fraction comparison (right). 100% CH_4 flame with 1.6 mm ID nozzle. Average fuel speed is 169 cm/s and coflow speed is 15 cm/s. Residence time contours (milliseconds) are superimposed on calculated soot volume fraction maps.
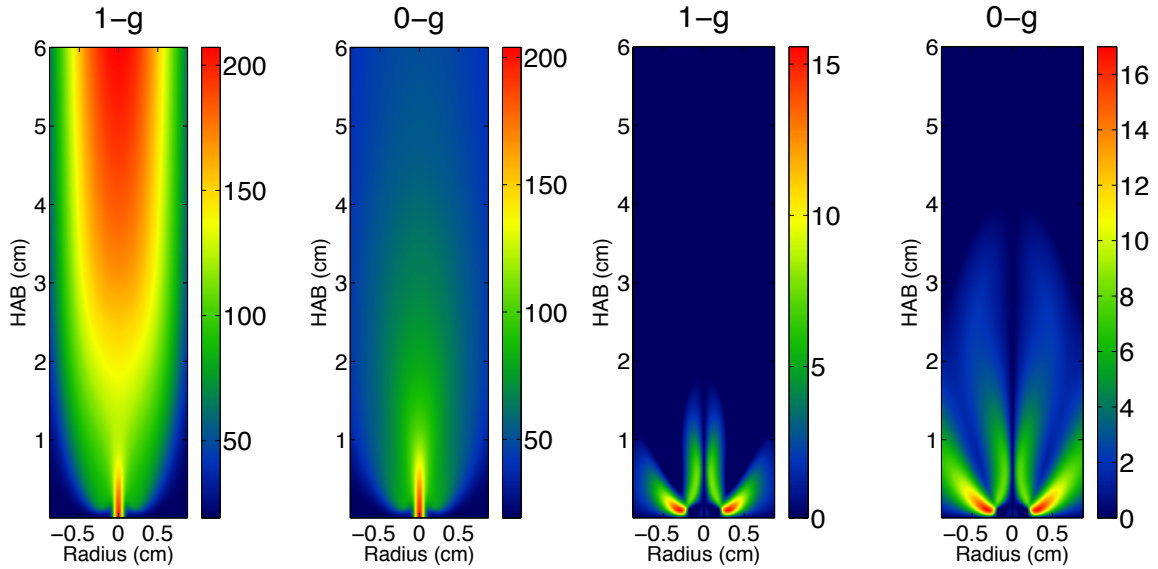
Fig. 4.10. 1-g and 0-g computed axial velocity comparison (left) and 1-g and 0-g radial velocity comparison (right) [cm/s]. 100% CH_4 flame with 1.6 mm ID nozzle. Average fuel speed is 169 cm/s and coflow speed is 15 cm/s.

To investigate the effect of coflow velocities, the coflow air velocity was increased to 40 cm/s from 15 cm/s while the fuel velocity was kept unchanged at 169 cm/s. The addition of coflow is expected to increase the axial convection around the flame wings. The 1-g flame did not change significantly, given the fact that this addition is relatively small compared to the buoyancy-induced convection in the 1-g flame. However, it has a bigger effect on the 0-g flame that is mainly momentum controlled. As can be seen from Fig. 4.11, where the experimental results of Fig. 4.9 are re-plotted in the top row for easy comparison, the 1-g flame sooting behavior is relatively unchanged while changing the coflow velocity from 15 cm/s to 40 cm/s. However, the 0-g flame becomes shorter and narrower. The soot volume fraction on the wings is greatly reduced, while the centerline soot volume fraction is relatively unchanged.

111
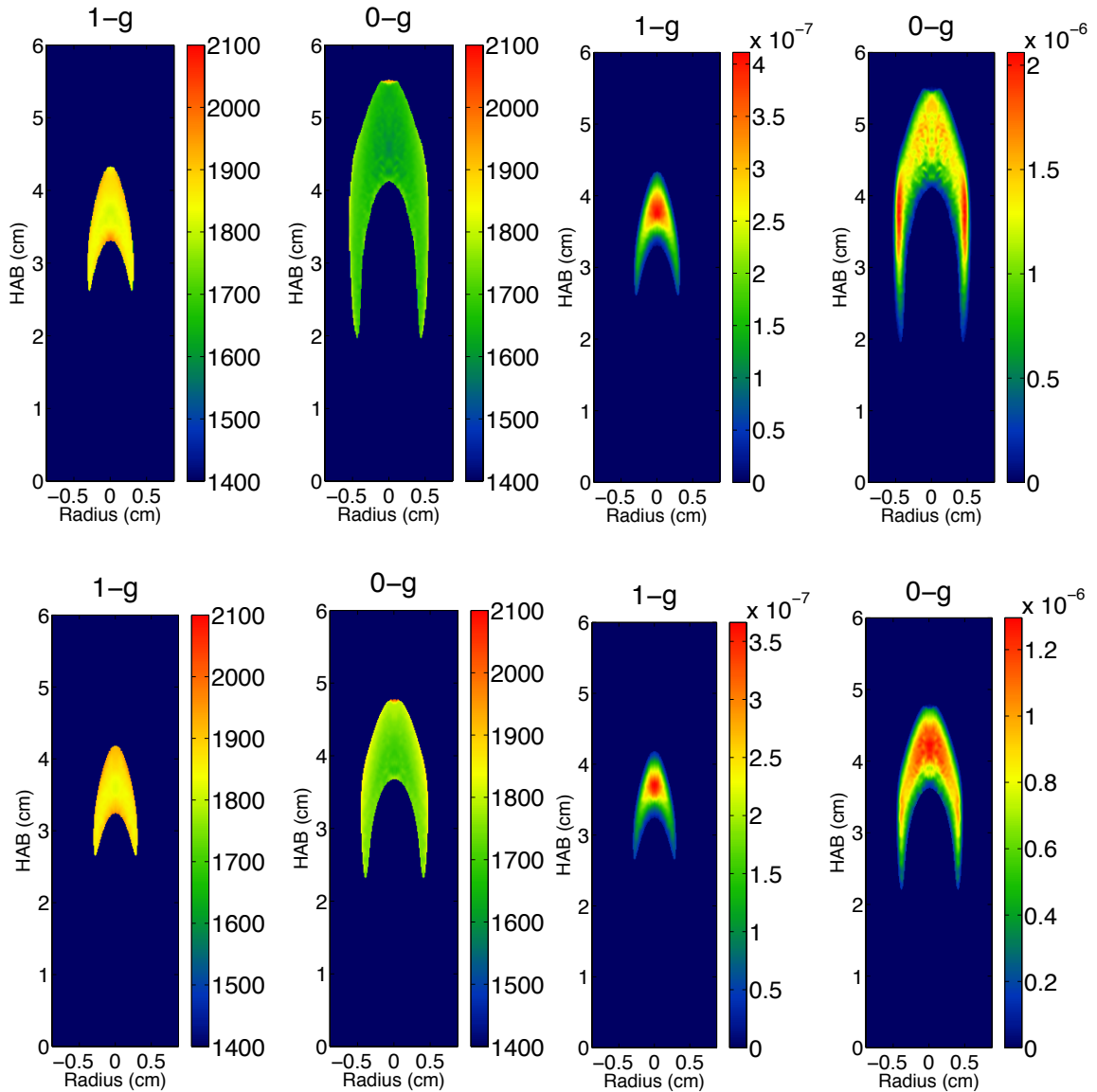
Fig. 4.11. 1-g and 0-g measured soot temperature (left) and volume fraction (right) comparison with increased coflow velocity. 100% CH_4 flame with 1.6 mm ID nozzle. Average fuel flow speed is 169 cm/s, coflow is 15 cm/s (top) and 40 cm/s (bottom).

From the experiments, the microgravity flames were found to be sootier than normal gravity flames by almost one order of magnitude in terms of the peak soot volume fraction. The distribution of soot was also found to have a tendency of propagating from

the centerline of the flame at normal gravity to the wings at microgravity. The flame temperature in 0-g is lower than its 1-g counterpart due to higher soot loading and more radiation loss. Computations of both 1-g and 0-g flames are currently in progress and only preliminary results are shown. More advanced reabsorption submodels will be introduced in the future, and the soot surface growth coefficient will be adjusted to improve the accuracy of the predictions.

4.3 Pre-investigation of ACME – the pressure effect

Our previous experimental and computational studies for the lifted methane/air coflow laminar diffusion flames are mainly performed at atmospheric pressure [Walsh 1998; Walsh 2000b; Walsh 2005]. Since the ACME chamber will not be actively vented, moderate pressure change is expected during the experiment, which may complicate the interpretation of flame behaviors under microgravity. In this study, previous experimental and computational investigations were extended to assess the influence of moderate changes in pressure between 1.0 atm and 1.5 atm. The flame front shape, lift-off height and temperature have been measured and calculated, and the results are compared in this study.

4.3.1 Experimental approach

The burner used in this study consists of a central fuel jet (4 mm inner diameter, 0.4 mm wall thickness) surrounded by coflowing air (50 mm diameter). The schematic drawing of the burner configuration is shown in Fig. 4.12. The plug flow exit velocity of both fuel and coflow was kept at 35 cm/s under different pressure levels, which means that the mass flow rate was changed accordingly. A wide range of flow conditions were measured in this study, with CH_4/N_2 fuel composition varying from 50% CH_4 (denoted

113

50/50) to 65% CH$_4$ (denoted 65/35), and with pressure varying from 1.0 atm to 1.5 atm in 0.1 atm increments. As pressure goes beyond 1.5 atm, considerable amount of soot is produced for both 50/50 and 65/35 flames. In this study, only non-sooty flames are investigated. A color photograph of the 1 atm 65/35 flame is shown in Fig. 4.13. A summary of all the flames investigated is shown in Fig. 4.14.
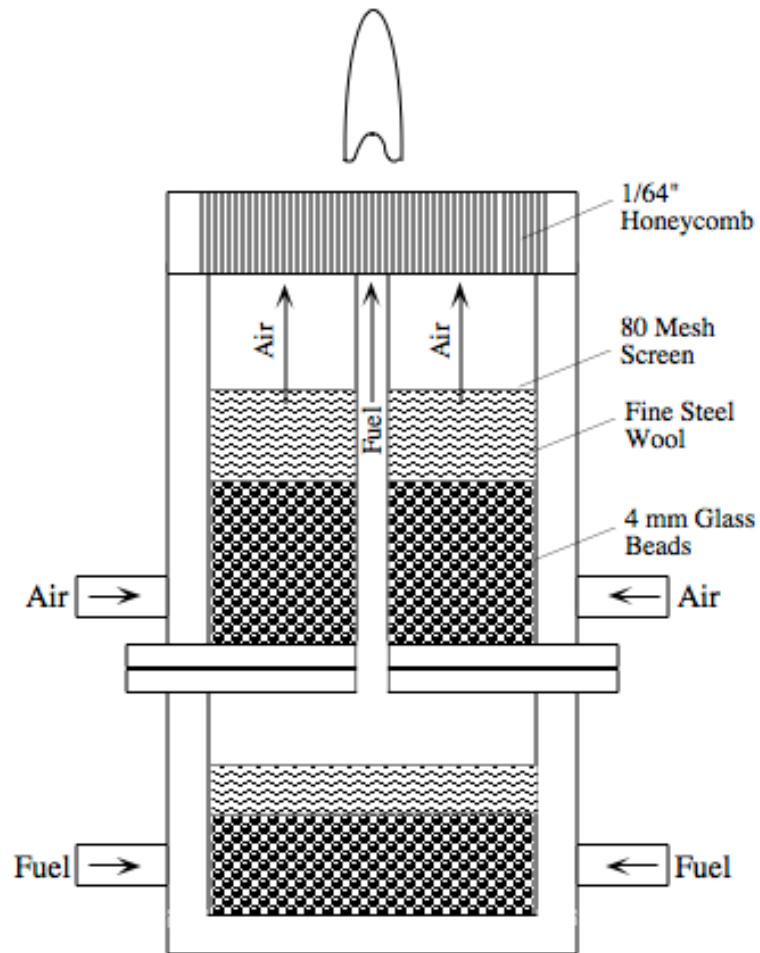
Fig. 4.12. Burner configuration

Fig. 4.13. A photograph of the 65% CH$_4$ flame

		Pressure (atm)					
		1	1.1	1.2	1.3	1.4	1.5
Dilution Level CH$_4$/N$_2$	50/50						
	65/35						

Fig. 4.14. A summary of the investigated flames with two levels of dilution under different pressures.

The burner and ignition system were housed on a stepper motor that can move in the vertical direction inside a 44.2 liter pressure chamber. The elevated pressures were stabilized by a servo valve using closed-loop control. The error of pressure is less than

1%. Three quartz windows on the chamber provided optical access to the flame. A ceramic grade SiC fiber 15 μm in diameter with known emissivity of 0.88 was mounted horizontally above the burner. A consumer DSLR camera (Nikon D300s) was fully characterized and used as the detector for the thin-filament pyrometry [Kuhn 2011] and chemiluminescence measurements. The camera utilizes a Bayer pattern color filter array and offers the necessary manual user control of settings and 14-bit raw data format. The raw format NEF file can be separated into red, green and blue channels after a decoding process [Coffin 2013]. A BG glass filter was used in the ratio pyrometry setup in order to provide better balance among the red, green, and blue intensities. An interference filter centered at 431 nm with a bandwidth of 10 nm was used in the chemiluminescence measurements to isolate CH* emission. An exposure time of 10 seconds was used to obtain good signal to noise ratios.

The flame front shape and lift-off height were inferred from the chemiluminescence measurement of CH*. Because the detected signal is a line-of-sight integration, a three-point Abel inversion [Walsh 2000a] was applied to obtain the radial distribution. The flame temperatures were obtained by thin-filament ratio pyrometry [Kuhn 2011]. Three signal ratios (green/red, blue/red and blue/green) can be calculated. With knowledge of the fiber's emissivity and camera's color filter transmission curves, the calculated ratios, which are functions of temperature, can be tabulated as a lookup table to infer the temperature. The measured temperature is essentially the one-dimensional fiber temperature. The local flame temperature was derived by considering the heat balance between the fiber radiation loss and the hot gas conductive heating [Kuhn 2011]. In order to obtain the two-dimensional temperature profile of the flame, the

burner was moved up in steps of 0.5 mm, and temperatures at different spatial heights were then stacked together to form 2-D temperature profiles as shown in Fig. 4.18 and Fig. 4.19.

4.3.2   Computational approach

The numerical simulation was performed by Professor Smooke's group. The computational models used here are similar to those discussed in Section 2.2.6 and Section 4.2.4 except that no soot model is included. Addition of a soot model would have caused some of the flames to become cooler, but would not have significantly changed the flame shape [Connelly 2009c]. The Reynolds number based on the fuel jet ranges from 42 in the 65/35 flame at ambient pressure to 63 in the 50/50 flame at 1.5 atm; therefore, all twelve flames are laminar. Two different chemical mechanisms have been employed: the GRI 3.0 mechanism without nitrogen chemistry (35 species and 217 reactions) and the SERDP mechanism [You 2007] (171 species and 1001 reactions). All thermodynamic, chemical, and detailed transport properties are evaluated using the CHEMKIN [Kee 1987] and TRANSPORT [Kee 1986] subroutine libraries, parts of which have been rewritten and restructured for greater speed [Giovangigli 1988]. The boundary conditions are similar to those in [Bennett 2008].

The solution process for each flame is identical to that discussed previously, except that the size of the mesh is 218×347 points and the finest spacings are $\triangle r = 0.004$ cm and $\triangle z = 0.008$ cm. Flame structure was calculated over a range of flow conditions at both ambient and elevated pressures. The computed solution at flow composition of 65/35 and ambient pressure was used as a starting point. In subsequent calculations, the pressure was increased by 0.1 atm, and a new solution was found using Newton's

method. The 50/50 mixture condition was reached by using the 65/35 flame as an initial condition and varying the fuel mixture in 5% increments.

4.3.3 Preliminary results and discussion

The spatial locations of CH and CH* have been shown to coexist [Walsh 2005] and are reasonable markers of the flame front region [Reuter 1986]. The CH concentration profiles computed based on GRI 3.0 and the measured CH* concentration profiles were compared for all the flames as shown in Fig. 4.15. Since only the flame front shape and lift-off height were investigated in this study, the absolute concentrations of CH and CH* were not required and the data were normalized to 1. For the 65/35 flames, the agreement is very good in terms of lift-off height, flame length and width. However, the computed lift-off heights for 50/50 flames are under-predicted. The computational results based on the two mechanisms (GRI 3.0 and SERDP) are almost the same; therefore only the results of GRI 3.0 are plotted in Fig. 4.15 for the sake of brevity.
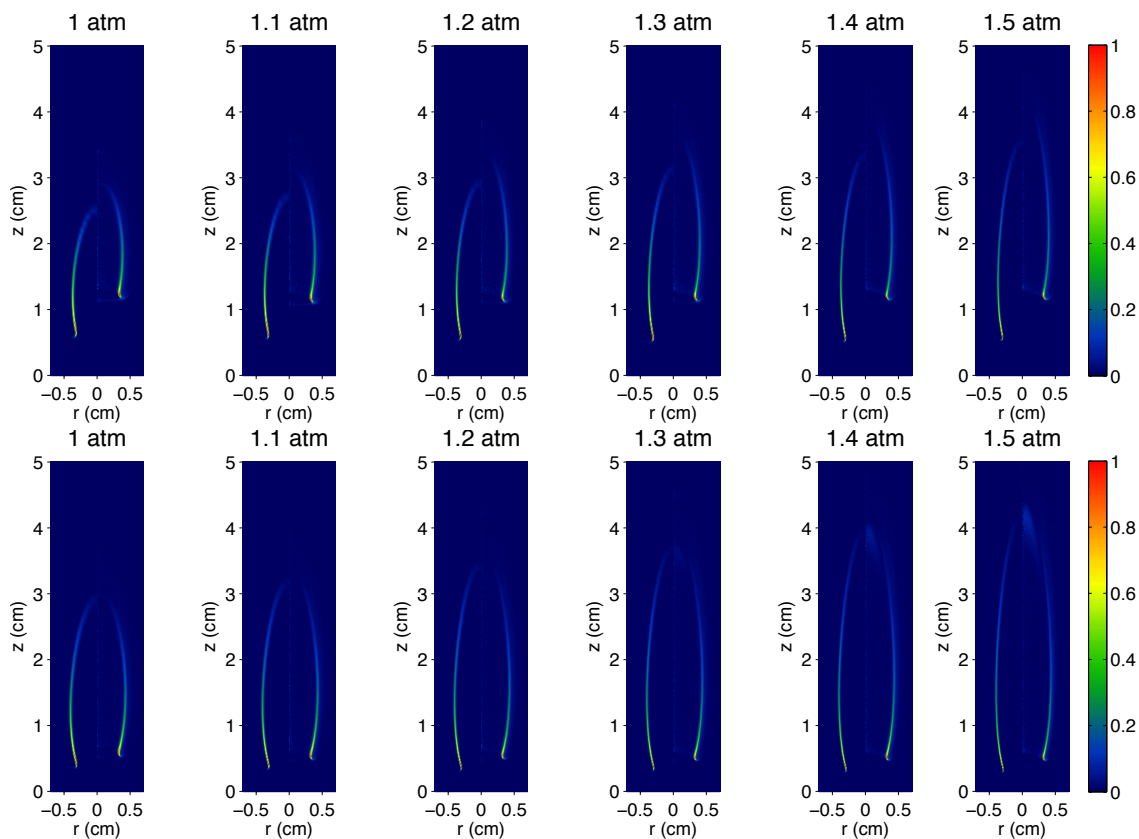
Fig. 4.15. Flame front shape comparison (50/50 top, 65/35 bottom, computation by GRI 3.0 left, experiment right).

At increased pressures, the mass flow rates were increased accordingly to maintain a constant unburned gas exit velocity. Since more mass was burned at higher pressure, the flame length increased with pressure. This trend has been captured both experimentally and computationally as shown in Fig. 4.16 by the modified flame length, which has been defined as the flame length minus the lift-off height. The flame length is the distance from the top of the burner to the location where the maximum temperature occurs along the flame centerline; the experimental and computational lift-off heights have been defined as the distance from the top of the burner to the location where the maximum CH* and CH concentration occurs, respectively. The lift-off heights seem to be insensitive to the pressure as shown in both Fig. 4.15 and Fig. 4.16.
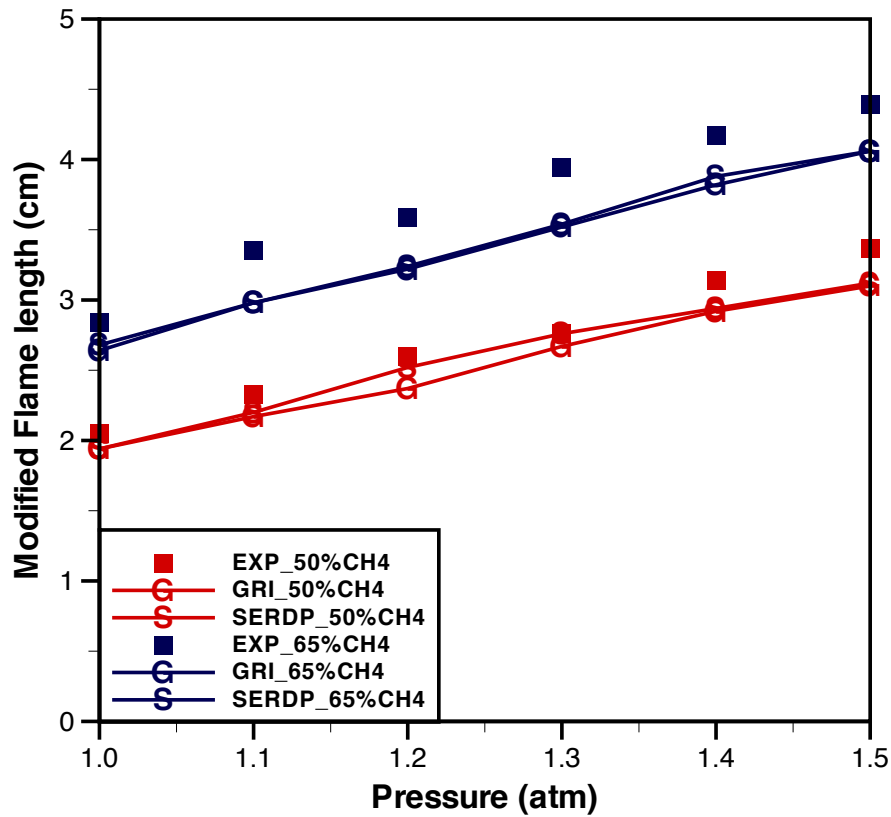
Fig. 4.16. Comparison of the modified flame length
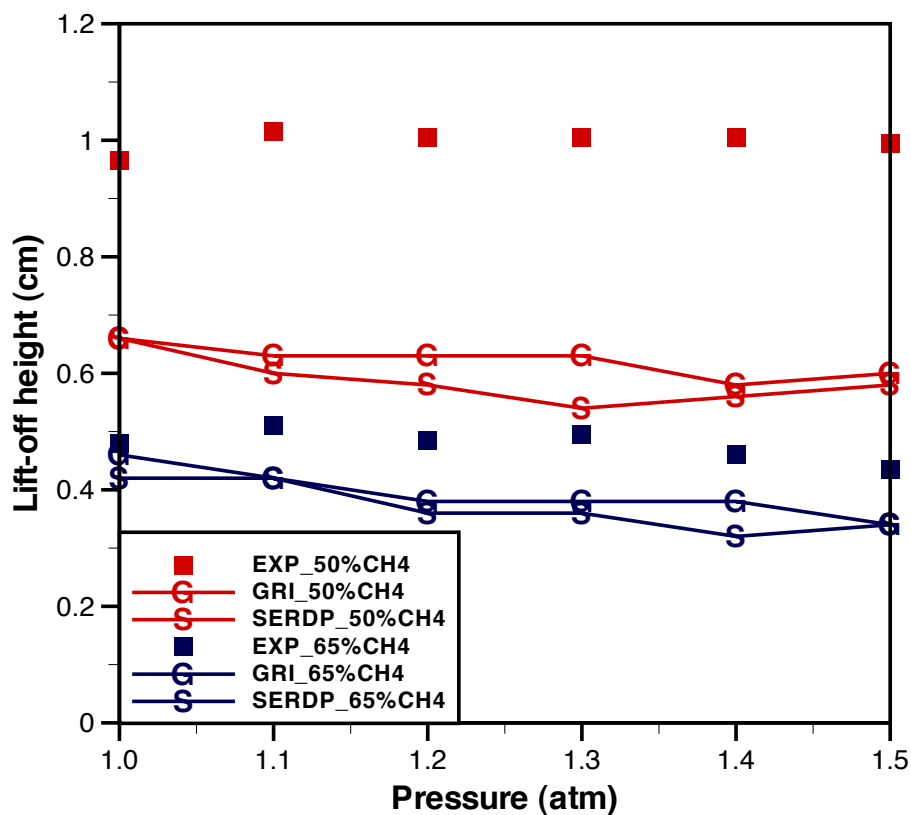
Fig. 4.17. Comparison of lift-off height

Despite the fact that the measured lift-off heights are higher than the computed ones, the flame temperatures have good agreement between the experiments and computations (Fig. 4.18 and Fig. 4.19). Also shown are the comparison of the computed temperatures by GRI 3.0 and SERDP; it is shown that the temperatures computed by the two mechanisms are essentially the same.
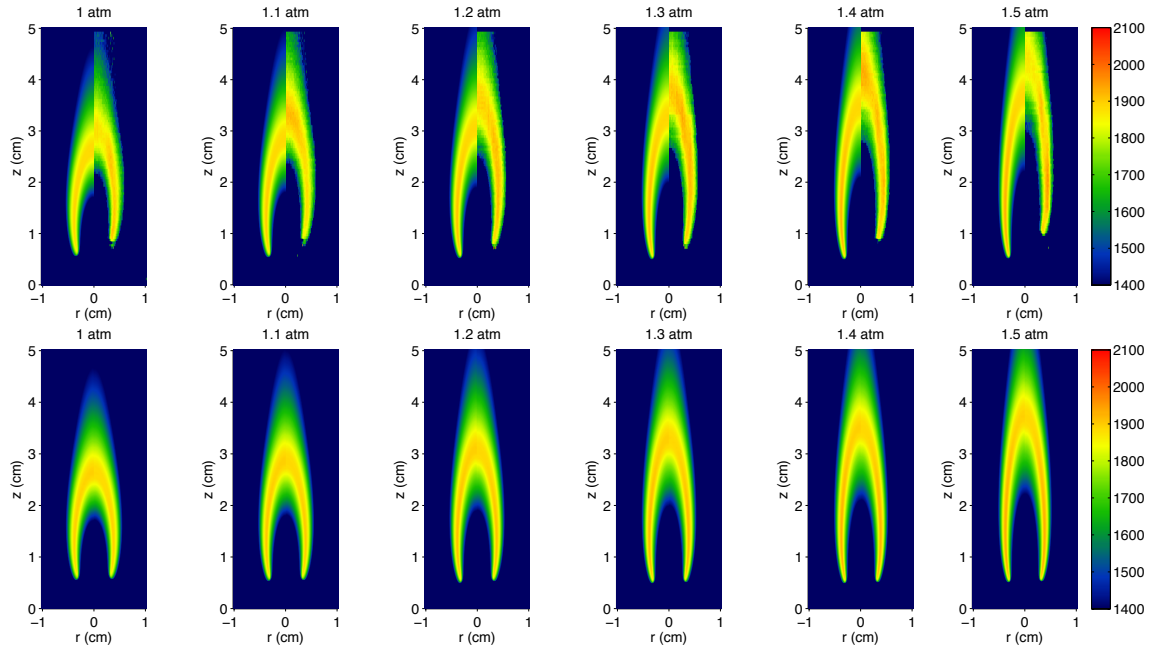
Fig. 4.18. 50/50 flame temperature. Top: GRI 3.0 (left) Experiment (right); Bottom: SERDP (left) GRI 3.0 (right).
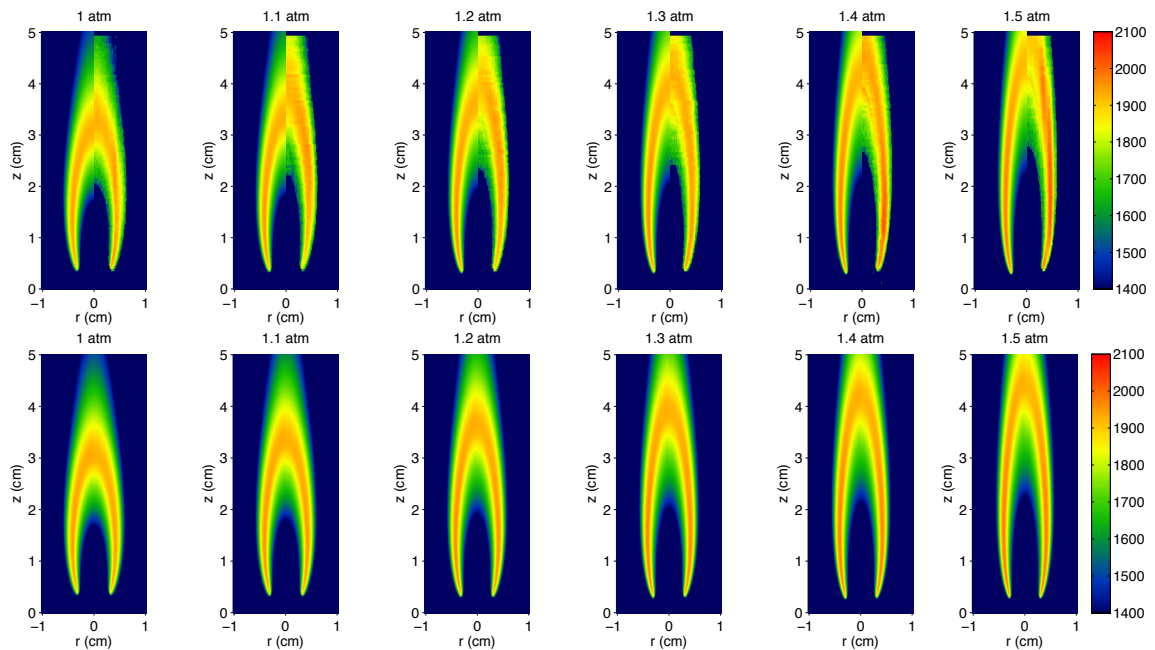
Fig. 4.19. 65/35 flame temperature. Top: GRI 3.0 (left) Experiment (right); Bottom: SERDP (left) GRI 3.0 (right)

Very good agreement was achieved for temperature and flame shape between experiments and computations at relatively lower dilution level. However, for the flames at higher dilution level, the predicted lift-off heights were lower than the experimental results. Further effort is needed to reduce such disagreement between experiment and computation, and such difference should be kept in mind while comparing the 1-g and 0-g flames in the CLD Flame experiment in the future.

5 Optical characterization of soot in the Yale coflow laminar diffusion flames

5.1 Introduction

Soot is a type of fine particulate matter under 2.5 μm (PM2.5) produced from incomplete combustion of hydrocarbon fuels and is considered as an airborne contaminant with known adverse effects on human health. Strict regulations enacted on the emission of PM2.5 by air-quality agencies require tight control of soot formation, which in turn requires understanding of the formation mechanisms. In the soot formation process, nearly spherical primary particles are first formed from large polycyclic aromatic hydrocarbon molecules, and then agglomerate into larger mass fractal aggregates that may contain hundreds of primary particles [Glassman 1989]. Various in-situ optical diagnostic techniques have been developed to characterize different properties of soot particles in point or planar measurements. For example, laser induced incandescence (LII) is often used to determine soot volume fraction and primary particle diameter in two dimensions [Will 1995; Schulz 2006; Thomson 2006; Michelsen 2007; Hofmann 2008]. One-angle elastic light scattering (ELS) can be used to determine soot radius of gyration in two dimensions if combined with LII [Will 1996; Reimann 2009]. Multi-angle light scattering (MALS), as an elastic light scattering technique, is often used to determine various aggregate parameters such as radius of gyration and fractal dimension, but is limited to point measurement [Sorensen 2001; Jones 2006; Oltmann 2010; Oltmann 2012]. In this work, two-dimensional multi-angle light scattering (2-D MALS) was developed, and used in conjunction with spectrally resolved line-of-sight attenuation

(spec-LOSA) to characterize N_2-diluted 60% and 80% C_2H_4 (with 40% N_2 and 20% N_2 by volume respectively) coflow laminar diffusion flames. The flames have been studied previously [Connelly 2009; Smooke 2005; Connelly 2009a; Connelly 2009b; Kuhn 2011; Ma 2013] and are target flames of the international sooting flame workshop [12/2013]. The results are combined with previously acquired particle sizing measurements performed by time-resolved laser-induced incandescence (TiRe-LII) [Connelly 2009] to provide insight on soot spectral emissivity and to correct soot pyrometry temperature measurements.

Multi-angle light scattering (MALS) is a powerful tool to characterize soot aggregate properties. In particular, the soot aggregate size can be measured by a multi-angle scattering experiment performed in the so-called Guinier regime through a Guinier analysis. Gangopadhyay *et al*. [Gangopadhyay 1991] applied the approach in measurement of soot aggregate size in a CH_4/O_2 premixed flame at several downstream points. The soot aggregate size was found to increase with height above the burner (HAB). Sorensen [Sorensen 2001] provided an excellent review on the subject of light scattering by fractal aggregates, in which the multi-angle scattering technique was discussed in detail. Oltmann *et al*. [Oltmann 2010] designed an experiment using an ellipsoidal mirror to collect the scattering signals from one point in a wide range of angles; this allows the determination of soot radius of gyration through single-shot acquisition of the full range of scattering angles. The approach was then applied in both laminar and turbulent flames, and good agreement was reported when comparing to TEM measurements [Oltmann 2012]. All of the previous MALS measurements, however, have been restricted to point measurements according to the authors' knowledge. Two-

dimensional full-field measurements are desired in order to better understand the soot formation process. In this work, the possibility of extending the Guinier analysis to two-dimensions through proper image processing is demonstrated. Two-dimensional maps of the weighted average or effective radius of gyration [Sorensen 2001; Oltmann 2012] are reported for N_2-diluted 60% and 80% C_2H_4 coflow laminar diffusion flames.

Light extinction, sometimes referred to as line-of-sight attenuation (LOSA), has been extensively used for soot measurements [Haynes 1980; Greenberg 1997a; Zhao 1998; Snelling 1999; Thomson 2008]. The light beam from some source (e.g., a laser or lamp) is arranged to traverse the absorbing media (i.e., the flame) before reaching a detector. The light attenuation can be determined by taking ratios of the attenuated beam over the non-attenuated beam, and can be used to determine the soot volume fraction, or even soot optical properties if combined with other measurements. The spec-LOSA technique is a further modification of LOSA made by Coderre *et al*. [Coderre 2011] that incorporates an imaging spectrometer to measure light attenuation as a function of wavelength. This technique has been applied to investigate the optical properties of both cooled soot [Coderre 2011] and in-flame aging soot [Migliorini 2011] at several downstream locations. In the current work, spec-LOSA has been used to measure soot extinction over the full sooty region of N_2-diluted 60% and 80% C_2H_4 coflow laminar diffusion flames by sequential measurements at different vertical heights above the burner. Spatially and spectrally resolved line-of-sight integrated extinction profiles are obtained, from which two-dimensional radially distributed extinction coefficient maps can be recovered by Abel inversion.

The measurements of flame extinction, soot radius of gyration, and soot primary particle sizes are combined to determine the dispersion exponent that describes the wavelength dependence of soot spectral emissivity. The dispersion exponents are determined in two dimensions, which allows for the calculation of soot spectral emissivity for each pixel location. Previously acquired soot temperatures determined by color-ratio pyrometry using a "nominal" constant value of the dispersion exponent [Kuhn 2011] are compared to those determined using measured dispersion exponents. Uncertainty analysis on the pyrometry-derived temperature is also performed.

5.2   Two-dimensional multi-angle light scattering

5.2.1   Guinier analysis

Multi-angle light scattering has been performed in the so-called Guinier regime to determine the effective soot aggregate size through a Guinier analysis. Excellent theoretical reviews on light scattering by fractal aggregates are available in Refs. [Sorensen 2001; Jones 2006] and only a brief introduction is presented here. An essential equation to describe soot aggregates is expressed as Eq. (5.2.1),

$$N = k_0 \left(\frac{R_g}{a} \right)^D \quad (5.2.1)$$

where N is the number of primary particles in an aggregate, k_0 is a proportionality factor of order unity, R_g is the radius of gyration and is defined as the root mean square of the distances between each primary particle and the center of mass of the aggregate, a is the radius of the primary particle, and D is the fractal dimension – normally in the range of

1.7 to 1.8 for soot [Sorensen 2001]. The objective of aggregate sizing is to measure the parameter R_g, which is a representative parameter for aggregate size. In the scattering experiment, an important experimental parameter is the scattering wave vector $\vec{q}$ defined as the difference of the incident and the scattered wave vector, and its magnitude is shown in Eq. (5.2.2).

$$q = 4\pi\lambda^{-1}\sin\left(\theta/2\right) \qquad (5.2.2)$$

The magnitude of the scattering wave vector $\vec{q}$ can be set by choosing the laser wavelength λ and detection angle θ. For monodisperse aggregates composed of monodisperse primary particles, the scattered light intensity can be expressed as follows under the approximations that primary particles are in the Rayleigh limit and each primary particle scatters independently:

$$I_{sca}\left(q\right) = I_{inc}nN^2V\frac{d\sigma^p}{d\Omega}S\left(qR_g\right) \qquad (5.2.3)$$

where I_{inc} is the incident laser intensity, n is the aggregate number density, N is the number of primary particles in a soot aggregate, V is the measurement volume, $\frac{d\sigma^p}{d\Omega}$ is the scattering cross section of a primary particle, and $S(qR_g)$ is the so-called structure factor, which is dependent on the radius of gyration. It can be seen that the ratio of the scattered signal $I_{sca}(0)$ at $\theta=0$ and $I_{sca}(q)$ at a certain angle is a function of only the

structure factor and simple geometric relationships that cause V to change with the angle. All other parameters are isotropic at any angle and cancel out. Furthermore, when the aggregate size is smaller or close to q^{-1} (the length scale of the scattering) in the so-called Guinier regime (i.e., $qR_g \leq 1$), the ratio can be approximately expressed by Eq. (5.2.4), which forms the basis of the Guinier analysis.

$$I_{sca}(0)/I_{sca}(q) = S(0)/S(qR_g) \approx 1 + \frac{1}{3}q^2 R_{g,eff}^2, \quad qR_g \leq 1, \quad \frac{I_{sca}(0)}{I_{sca}(q)} < 2 \qquad (5.2.4)$$

For real soot aggregates that are polydisperse, the measured radius of gyration must be considered as an effective value $R_{g,eff}$ that has the physical meaning of being a weighted average as defined by Eq. (5.2.5) with the polydispersity of the monomer radius, which should be significantly smaller than that of the aggregates, neglected [Sorensen 1992]. The value of $R_{g,eff}$ is generally greater than the arithmetic mean since it is strongly influenced by the large end of the distribution, but it still provides insight into the size of aggregates.

$$R_{g,eff}^2 = \frac{\int N^2 R_g^2(N)n(N)dN}{\int N^2 n(N)dN} = a^2 k_0^{-\frac{2}{D}} \frac{M_{2+2/D}}{M_2} \qquad (5.2.5)$$

where $n(N)$ and $R_g(N)$ are the distributions of number density and radius of gyration of the aggregate respectively. The moment term M_i is defined by Eq. (5.2.6) as

$$M_i = \int_{N=1}^{N=\infty} n(N) N^i \, dN \qquad (5.2.6)$$

A routine procedure to determine $R_{g,eff}$ is to first obtain the scattering signal ratios through a multi-angle scattering experiment, and then plot the ratios as a function of q^2. The effective radius of gyration $R_{g,eff}$ can then be obtained from a linear curve fitting with the slope equal to $\frac{1}{3} R_{g,eff}^2$. The range of $I_{sca}(0)/ I_{sca}(q)$ with good linearity is normally extended up to a value of 2 [Sorensen 2001; Oltmann 2010]. Therefore the Guinier evaluation range of this study is also bounded by $I_{sca}(0)/I_{sca}(q) < 2$.

5.2.2 Experimental setup

The experimental setup for two-dimensional multi-angle light scattering is shown in Fig. 5.1. The flames investigated in this work are sooting, axisymmetric, laminar diffusion flames operating under 1 atm at 298 K. The fuel consisted of 60% and 80% C_2H_4 by volume, with the balance being N_2. The burner consists of a 0.4 cm inner diameter vertical tube, surrounded by a 7.4 cm diameter coflow. The fuel velocity at the burner surface had a parabolic profile and the air coflow was plug flow, both with average velocities of 35 cm/s. The burner was mounted on a programmable stepping motor for vertical movement. A frequency-doubled 532 nm Nd:YAG laser (Continuum PL-8010) with a repetition rate of 10 Hz provided the illumination. A 300 mm focal length cylindrical lens focused the laser to a vertical sheet that traversed the center of the flame. The laser sheet thickness is measured to vary from 72 μm at the flame centerline to 81 μm at a radius of 3 mm near the luminous edge of the flame. The long focal length lens is preferred to provide a nearly constant beam thickness across the flame.

Nevertheless, slight variation of beam thickness is not critical since a divergent beam increases the sample volume while proportionately decreasing with laser fluence. The total signal is kept relatively constant. The laser sheet was spatially cropped by an aperture to ~ 7 mm in height. The flame was sequentially measured at different heights by vertically moving the burner in steps of 2 mm using a stepper motor. The central region of the laser sheet, where the intensity is more stable and evenly distributed, was used for signal evaluation and used to composite the full flame information. Similar results were obtained if the central 4 mm region was used to composite the full flame image, but only the results of the 2 mm case are shown here. A neutral density filter was placed in the optical path to attenuate the laser beam to an energy level of ~ 5 mJ per pulse to prevent laser-induced incandescence (LII). Negligible LII signal was verified by comparing the signals at 431 nm (collected through a narrowband interference filter) with the laser turned on and off. A pyroelectric power meter (LaserProbe RjP-734) was used to monitor the laser energy and to stop the beam. The measured laser energy was used for signal normalization to account for laser power fluctuations and drift.
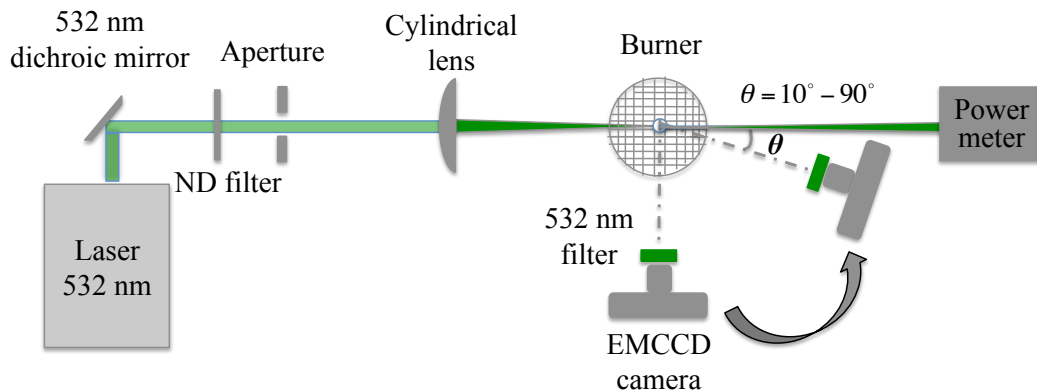
Fig. 5.1. Two-dimensional multi-angle light scattering setup.

The multi-angle scattering experiment involves imaging the soot-scattered signal at a set of angles. The detector was a cooled interline EMCCD camera (Andor Luca S) with 658 × 496 pixels and a pixel size of 10 μm. The camera was operated using the shortest available gate time of 470 μs. The camera was attached to a bar that rotated concentrically about the burner. The distance between the camera and the burner was fixed at 25 cm to ensure the same collection efficiency at each angle and each image was centered on the burner. The detection angle between the lens optical axis and the laser beam was varied from 10° to 90°. Since the distance between the camera and the burner (25 cm) is much larger than the maximum flame diameter (~ 7 mm), the variation of detection angle as a function of position in the image can be neglected. A 50 mm focal length camera lens with extension tube was coupled to the detector. The horizontal spatial projection onto a single pixel varied from 25 μm at a detection angle of 90° to 144 μm at a 10° detection angle. A sufficient depth of field (i.e., greater than the maximum flame diameter of ~ 7 mm) was maintained with the f-number set at 16 such that even at the 10° detection angle, the entire flame scattering image remained in good focus. This was verified by comparison of target images at different angles, which is discussed in the next section. Each image was averaged over 50 laser shots to minimize the effect of small spatial variations of the flame caused by room air currents. For the sooty flames investigated in the study, the scattering signal is significantly greater (~ two orders of magnitude greater in the sooty region) than flame luminosity. Nevertheless, flame background images were also acquired in the same way with the laser turned off and subtracted from the scattering signal images.

5.2.3 Image processing

The entire flame was sequentially imaged from upstream to downstream. However, only images at one downstream location are shown in this section to illustrate the image processing procedure. Raw scattering images taken at different angles from 10° to 90° are shown in Fig. 5.2. The image at the right-bottom corner is a normally-observed image viewed at a 90° detection angle. When the camera was rotated around the burner to a smaller detection angle, the observed images became narrower in shape and the signal on each pixel was increased due to an increased sample volume as illustrated in Fig. 5.3. The sample volume illuminated by the laser beam and then projected onto a pixel is shown as a red shaded area and varies with detection angle. At angle θ, the sample volume $V(\theta)$ is a factor of $1/sin(\theta)$ greater than the sample volume at an angle of 90°. The soot distribution is assumed to be uniform over the small sample volume and therefore the signal is expected to increase by a factor of $1/sin(\theta)$ from the 90° detection angle to a smaller detection angle θ.
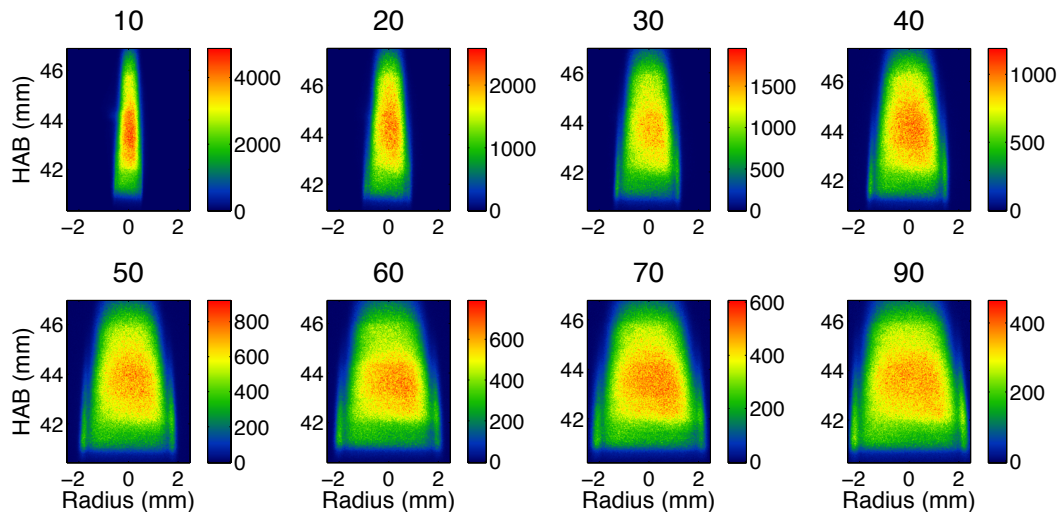
Fig. 5.2. Background-subtracted and signal-averaged scattering images taken at 10° - 90° detection angles as specified. The data are from a region near the tip of the 60% flame with signal values expressed as average CCD counts.
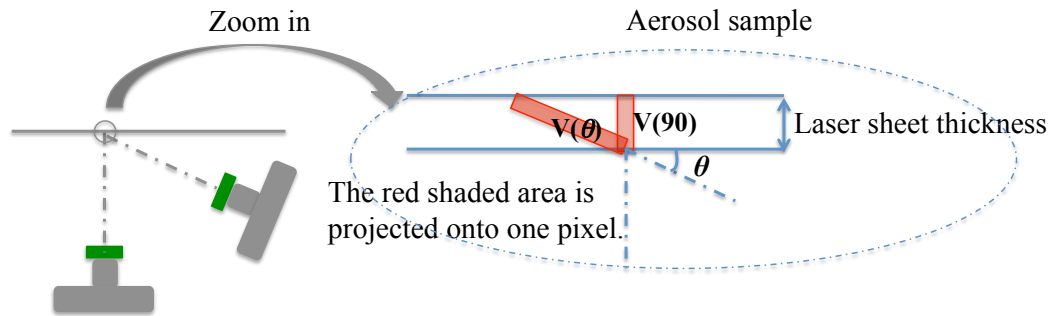
Fig. 5.3. An illustration of the increased sample volume at a decreased detection angle.

To perform the Guinier analysis in two dimensions, the raw images must be first transformed to images with good spatial coincidence so that the ratio can be directly taken on a pixel-by-pixel basis. The spatially transformed images must then be re-sampled to carry the correct intensity information (i.e., pixel value). In this work, the image transformation was performed through bilinear image warping in Matlab. Image warping involves a geometric mapping from the coordinate space of a source image to that of a destination image and a re-sampling procedure to determine the destination signals through an interpolation based on source signals. Bilinear image warping is an eight parameter warping that can be used to transform an arbitrary quadrilateral in the source image to an arbitrary quadrilateral in the destination image. The source coordinate

(x,y) is correlated with the destination coordinate (u,v) through Eq. (5.2.7) [Glasbey 1998].

$$
\begin{aligned}
u &= a_{10}x + a_{01}y + a_{11}xy + a_{00} \\
v &= b_{10}x + b_{01}y + b_{11}xy + b_{00}
\end{aligned}
\qquad (5.2.7)
$$

where a_{ij} and b_{ij} are the eight parameters that can be solved given an initial source/destination image pair. To determine the eight parameters in Eq. (5.2.7), an engineering graph paper consisting of an equally spaced grid was used as a target. The target was fixed in the plane of the laser sheet, centered on the burner nozzle. Target shots were taken at a set of detection angles as shown in the top of Fig. 5.4. The 90° shot was chosen as the destination image while others are the source images. The same four non-collinear points on the target shots were chosen in each image as illustrated by the red crosses. For every pair of source/destination images (e.g., 10°/90° or 70°/90°), four points (eight coordinate values) were used to solve for the eight parameters using Eq. (5.2.7). After the parameters were solved, the target shots in the source coordinates were spatially transformed into new images in destination coordinates as shown in the bottom of Fig. 5.4. Re-sampling of the images was performed by a bilinear interpolation. Good spatial coincidence was achieved in the transformed images. The images at smaller detection angle (e.g., at 10°) are seen to be blurrier mainly due to their smaller spatial resolution in the original image, which is a factor of ~ 5.8 [$sin(90°)/sin(10°)$] smaller than the resolution at the 90° detection angle. An estimate of the spatial mismatch between the images can be obtained by considering the standard deviation in pixel locations between intersecting grid points in the transformed target images. By considering random 4 pixels over the central 2 mm region used for the composite flame images, maximum standard

deviations of 0.091 mm and 0.096 mm were found in the radial and axial directions, respectively.
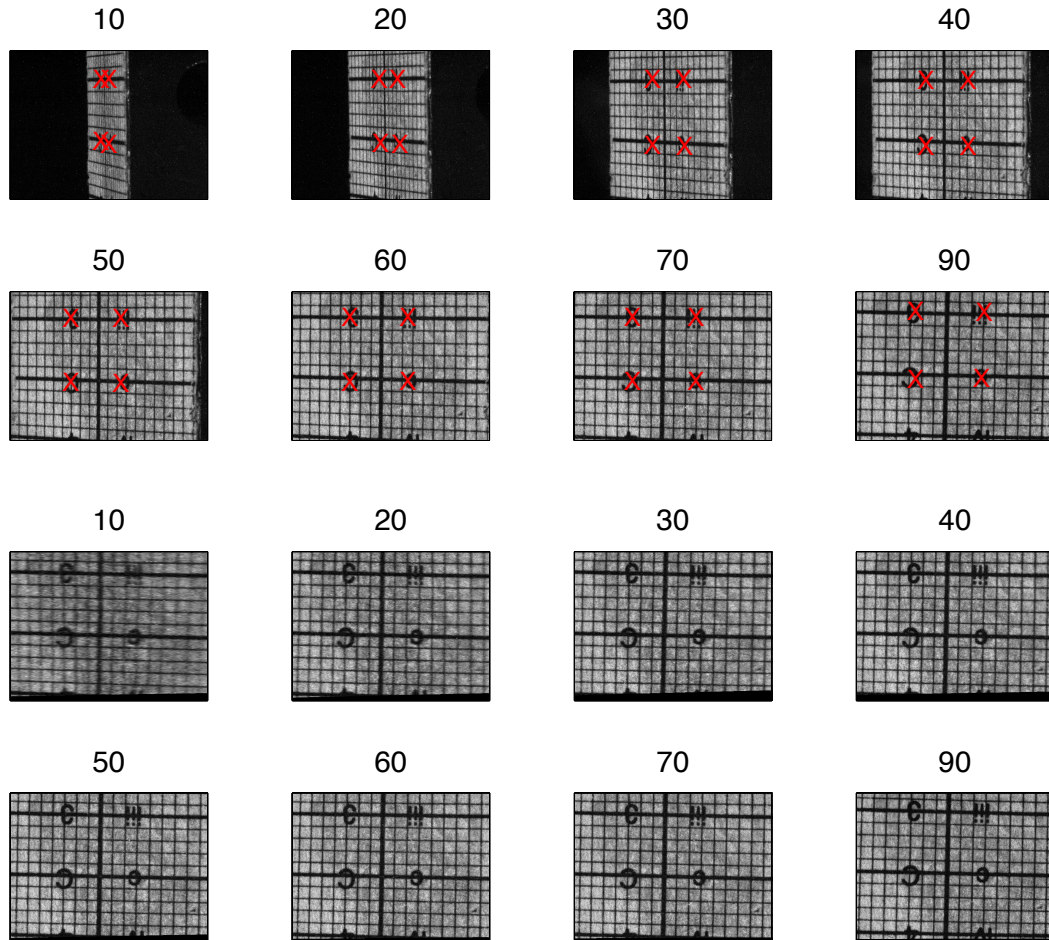
Fig. 5.4. The original target images (top) and spatially transformed target images (bottom).

The same spatial transformation and signal interpolation procedure was then applied to the background-subtracted scattering images. The images were then normalized by a factor of $1/sin(\theta)$ at each detection angle θ due to sample volume

considerations shown in Fig. 5.3. The warped scattering images were cropped and are shown in Fig. 5.5.
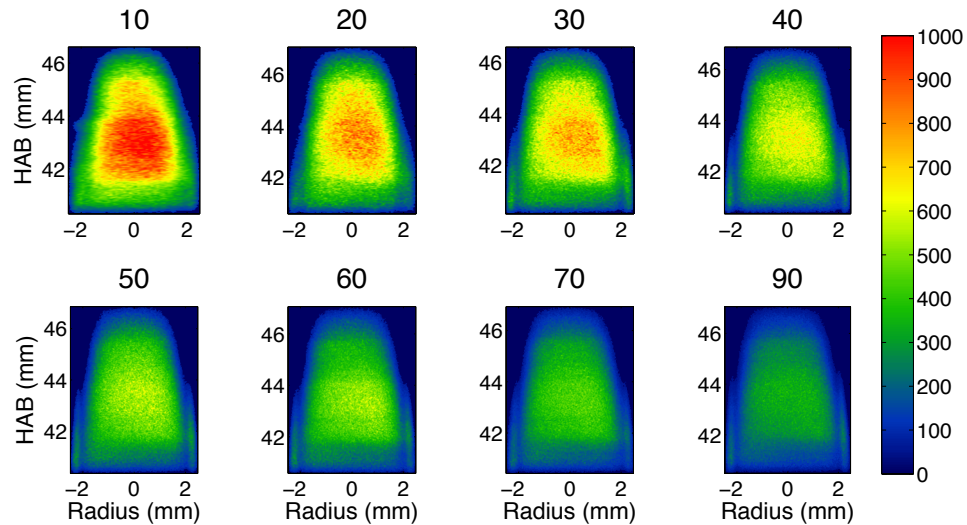
Fig. 5.5. Warped scattering images at 10°-90° detection angles.

As can be seen, two small peaks, possibly a result of different temperature-time history of soot particles, at a radius of 2 mm are visible in images taken at angles from 30° to 90°, however, they are not clearly visible in the images taken at 10° and 20°. This is expected since for imaging at small detection angles, fine features (e.g., large gradients) are not well resolved due to the smearing effect as shown in Fig. 5.6. For the normal view, the features at different depths of the sample volume will project onto the same location on the CCD. In contrast, at a small detection angle θ, the projection of features at different depths of the sample volume will be slightly shifted on the CCD, with the maximum shift ($72 \times cos(\theta)$ μm) occurring at the front and back surface of the sample volume (based on the measured laser beam thickness of 72 μm). In the case of $\theta =$ 10°, the shift spans roughly 7 pixels. Such a shift creates smeared images at small

detection angles and fails to capture large gradient features as seen in both Fig. 5.4 and Fig. 5.5, where the images at 10° and 20° are blurred and do not preserve the steep gradients (i.e., the peaks) at a radius of 2 mm. When taking ratios of the image at 10° (without peaks) over images at other different angles (with peaks) for the Guinier analysis, the ratio images will contain artificial peaks due to the smearing effect. To address this problem, images taken at angles from 20° to 90° were all degraded via image processing to the 10° viewing angle, in order to match the spatial resolution, and more importantly, to match the smearing effect. The image degradations were performed based on computer simulations of the smearing effect. The sample volume was first sliced into at least ten layers along the depth of the sample volume, and each layer was projected onto the CCD plane with a slight spatial shift. The summation of the projected layers is the simulated smeared image shown in Fig. 5.6, where its normal view image was also shown for comparison.
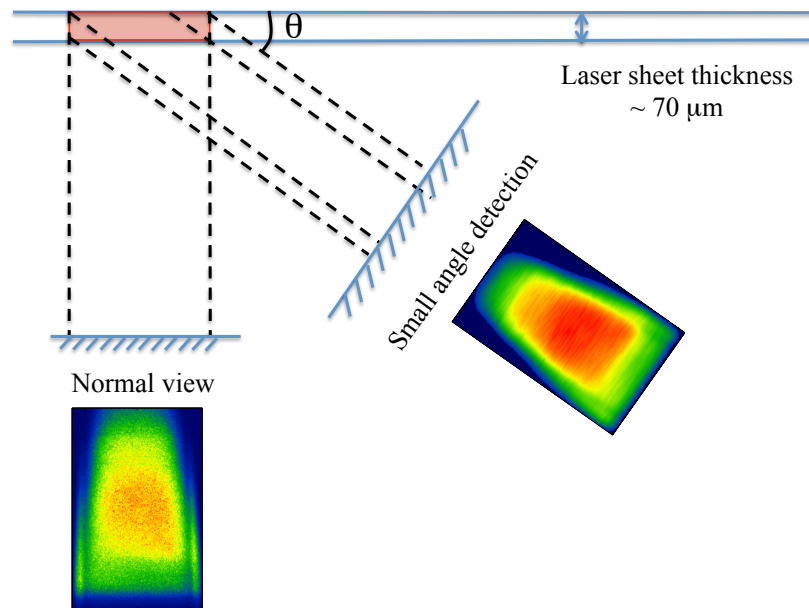
Fig. 5.6. An illustration of the smearing effect at a small detection angle. Here, the

small angle detection image was calculated based on the normal view

image.

The purpose of image processing in this work is to transform images taken at different angles into spatially coincident images, as a preparation for taking ratios on a pixel-by-pixel basis for the Guinier analysis in two-dimensions. During the image processing, it is important to make sure that the final warped images still carry the correct intensity signals. A useful check is to compare the total signal value of the original image and the warped image, as this total value should not be significantly altered by various image-processing steps. The total signal was calculated by summing up all the pixel values in the frame, with any pixels outside the scattering region set to zero. The ratio of the total signal of raw images and warped images are calculated to be close to unity with variations less than 3%.

Following the Guinier analysis, ratios of the $I(0)$ image over $I(\theta)$ image were taken. Since it is not possible to obtain the scattered signal at strictly 0°, 10° is often used as the smallest angle for taking ratios [Sorensen 2001; Oltmann 2012]. The approximation tends to reduce the derived radius of gyration somewhat, with the greatest effect for larger aggregates. However even for the largest $R_{g,eff}$ reported here, the error is ~ 3%. The ratio images without and with smear correction are shown in Fig. 5.7 in the top row and bottom row respectively. The ones with smear correction are better at removing the artificial peaks on the wings.
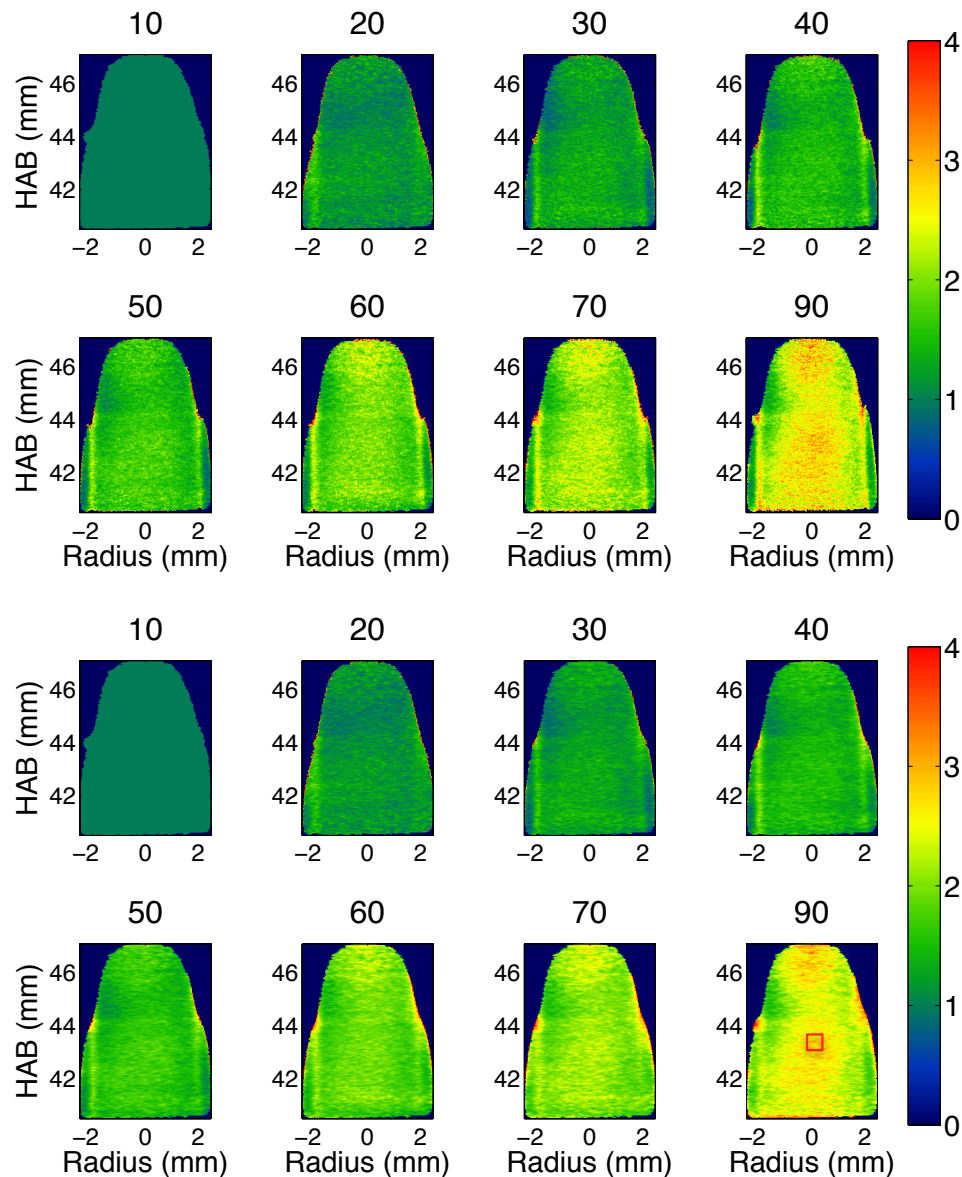
Fig. 5.7. Ratio images of $I(10)/I(\theta)$ without the smearing correction (top) and with the smearing correction (bottom).

Average values were calculated for a small region in each of the ratio images and are shown as a function of q^2 in Fig. 5.8. The position of the small region is illustrated by a red rectangle shown in the last image in Fig. 5.7. Good linearity is obtained in the Guinier evaluation range where $I_{sca}(0)/I_{sca}(\theta) < 2$. A linear curve fitting was performed in

the range and a R^2 value of 0.992 was obtained as a representation for the goodness of fitting. $R_{g,eff}$ was determined to be 130.1 nm from the slope of the fitted curve.
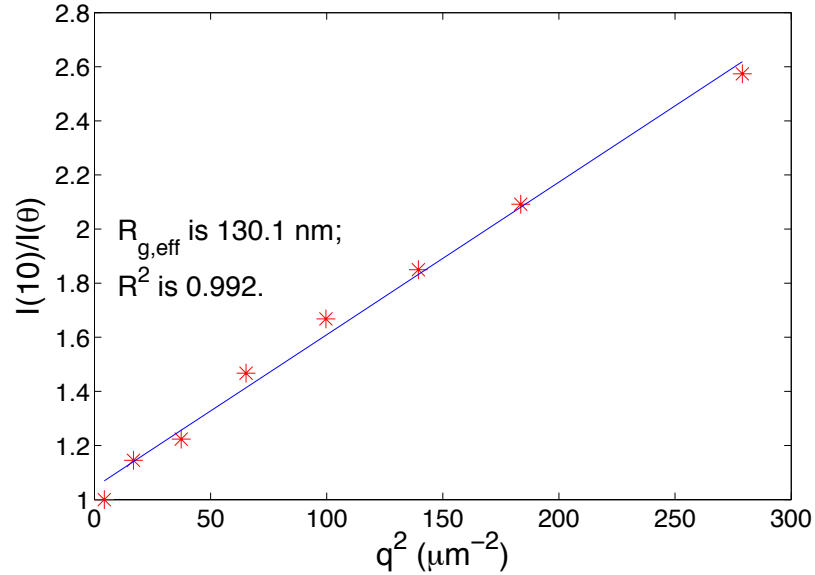
Fig. 5.8. The measured ratio of $I(10)/I(\theta)$ plotted as a function of q^2 (red dots) and a linearly fitted curve (blue line).

The flame was sequentially measured at different heights by vertically moving the burner in steps of 2 mm using a stepper motor and the above procedure was performed for each pixel at each height. Full flame $R_{g,eff}$ and R^2 maps of the 60% C_2H_4 and 80% C_2H_4 coflow laminar diffusion flames are composited and shown in Fig. 5.9. A spatial filter based on R^2 maps was created to filter out $R_{g,eff}$ points with R^2 values less than 0.5. It should be noted that the data at the flame tip for the 80% flame has a discontinuity at 73 mm HAB. This is mainly due to the fact that multiple images taken at different times, with small spatial fluctuations on the tip, were used to evaluate $R_{g,eff}$, and the fluctuating signals were likely to distort the slope of fitting and result in greater or smaller value of $R_{g,eff}$. The $R_{g,eff}$ peaks along the wings may be problematic as well, since the intensity

gradients of scattering images at these regions are large and a slight spatial mismatch could result in distorted ratios and therefore $R_{g,eff}$ values. The R^2 values are also observed to be relatively low at the upstream locations around HAB = 30 mm and HAB = 38 mm for 60% and 80% flames respectively. In these regions, the scattering intensities at the wings saturate much earlier than the intensities around the flame centerline. In order to obtain unsaturated images, the signals around the centerline were low and noisy, which results in lower R^2 values. These issues mentioned above might be improved in a future experiment by imaging the large gradient regions (e.g., the wings) with higher spatial resolution, and spatially filtering the wings to obtain greater signal around the centerline. Nevertheless, the R^2 values, generally greater than 0.9 except at the low signal regions, give confidence in the validity of the $R_{g,eff}$ values. The centerline $R_{g,eff}$ values for both flames are plotted in Fig. 5.10. Despite the noise of the plot, $R_{g,eff}$ is shown to monotonically increase with the HAB from 80 nm to 160 nm for the 60% C_2H_4 flame and 100 nm to 200 nm for the 80% C_2H_4 flame.
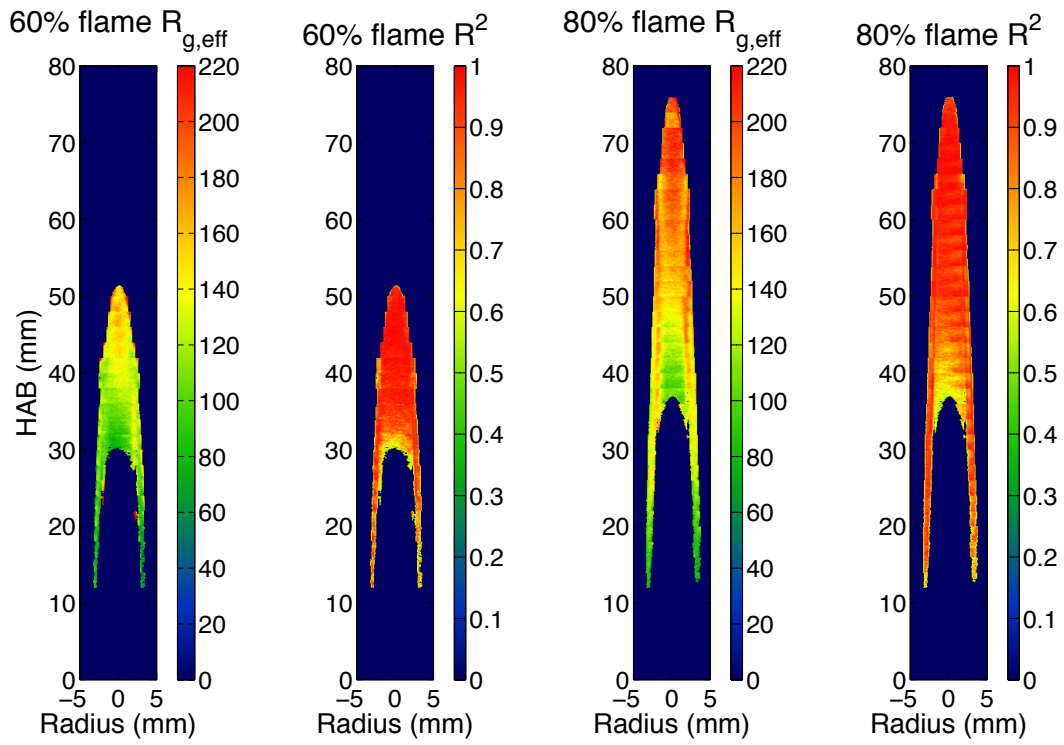
Fig. 5.9. Soot radius of gyration of the 60% and 80% C$_2$H$_4$ flame and its corresponding R^2 maps.
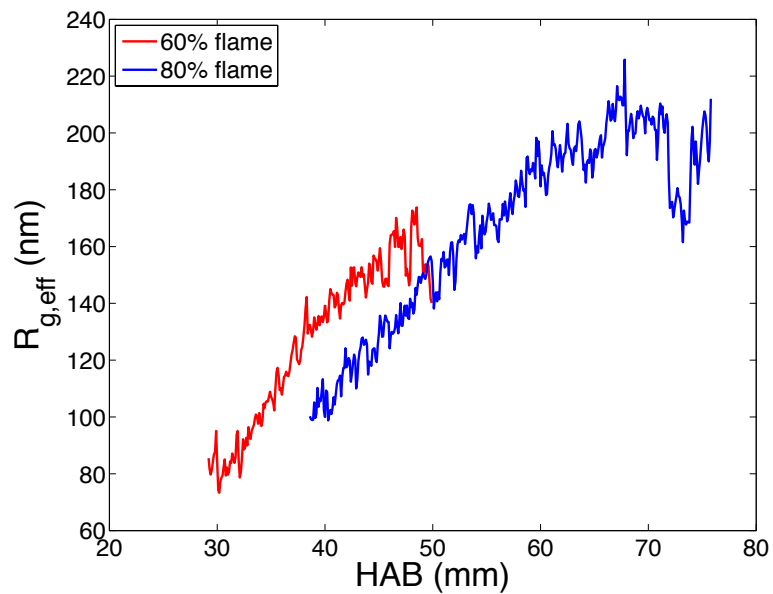
Fig. 5.10. Effective soot radius of gyration along the centerline of 60% and 80% flames as a function of the height above the burner.

5.3 Spectrally resolved line-of-sight attenuation

5.3.1 Experimental setup

The experimental configuration for making spectrally resolved absorption measurements along a radial line through the flame is shown in Fig. 5.11. A high intensity illuminator (Dolan-Jenner Fiber-Lite series 180) was observed to provide stable output after a 20-minute warm-up and was used as the light source. A 2 mm diameter aperture was placed in front of the light to provide a point source. Three spherical glass lenses, with focal length 200 mm, 125 mm and 125 mm respectively, were used to collimate and focus the light beam. The distance between the aperture and lens matches the focal length. The maximum angular dispersion due to chromatic effects between 400 nm and 750 nm is estimated to be ~ 0.01°. Therefore, parallel beams can be assumed to pass the flame and enter into the spectrograph as shown by the dashed lines. An externally controlled mechanical shutter was placed in the optical path and was synced with image acquisition to block or unblock the light source. A thermoelectrically cooled CCD camera (SBIG STF-8300M chip, 16 bits/pixel digitization, 3326 × 2504 pixels at 5.4 microns) was used in conjunction with an imaging spectrograph (Jobin Yvon CP200), with a 200-groove/mm grating and a 0.05 mm horizontal entrance slit. The cooling temperature was stabilized at -10°C to reduce thermal noise on the CCD chip.
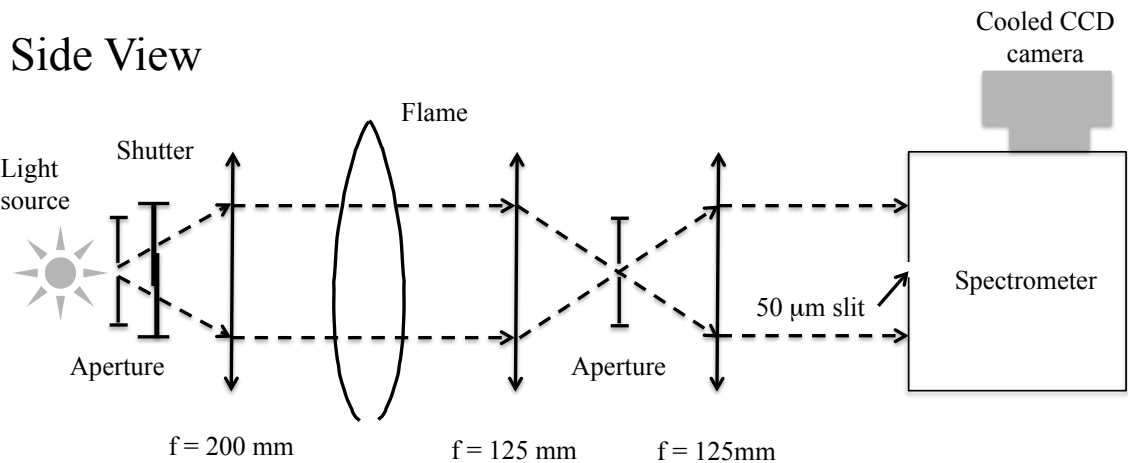
Fig. 5.11. Spec-LOSA experimental setup.

Hyperspectral images were captured with the spatial coordinate along the radius of the flame and the spectral coordinate covering the range from 400 nm to 750 nm. The spatial projection is 5.95 μm per pixel and the spectral dispersion is 0.14 nm per pixel. For this imaging configuration, the maximum flame width was smaller than the long dimension of the entrance slit. Therefore, the full width of the flame was imaged into the spectrograph without being clipped, which allowed the inversion of the natural log of the line-of-sight integrated transmissivity to obtain a radial profile of the extinction coefficients. The burner was mounted on a stepper motor to allow vertical movement. The flame was traversed at steps of 0.5 mm starting from 1 cm above the burner, below which there was no measurable visible light attenuation. For the 60% and 80% flames, 90 and 130 steps were used to traverse the flames respectively. Data acquisition was automated with the open source software OMA, which was used to control the movement of the stepper motor, image acquisition of the CCD camera and the open/close status of the mechanical shutter. At each height, with the flame kept ignited, transmission and emission images were acquired as the lamp was unblocked and blocked. A lamp image

and dark background image were taken when the flame was turned off after scanning the whole flame to reduce the total experiment time. The final images are summations of five exposures of 0.2 seconds each, to average small spatial variations of the flame caused by room air currents as well as to improve the signal-to-noise ratio.

5.3.2 Image processing

A typical set of raw images is shown in Fig. 5.12. The TRANSMISSION image was taken when the flame and lamp were both turned on. The EMISSION image was taken when the flame was on but the lamp was blocked. The LAMP image was taken only once when the flame was turned off and lamp was unblocked. The DARK image was taken when the flame and lamp were both turned off.
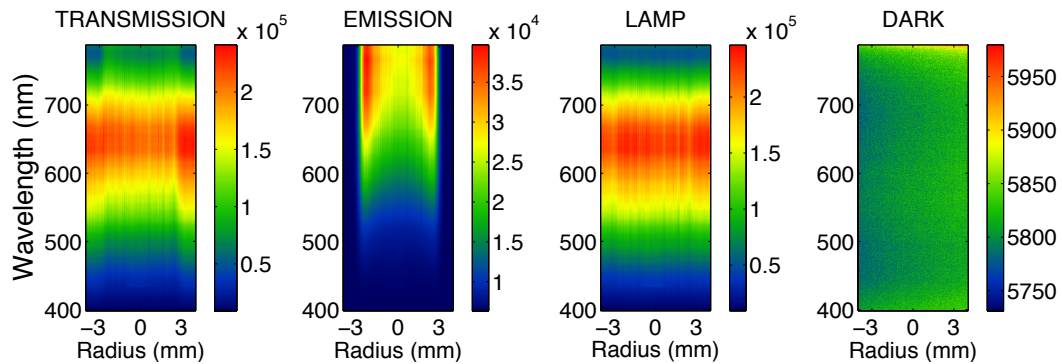
Fig. 5.12. Sample raw images at a height of 35 mm above the burner for the 80 % C_2H_4 flame.

The line-of-sight integrated spectral transmissivity, τ_λ, can be obtained via Eq. (5.3.1) and is shown in Fig. 5.13 on the left.

$$Transmissivity(\tau_\lambda) = \frac{Transmission - Emission}{Lamp - Dark} \quad (5.3.1)$$
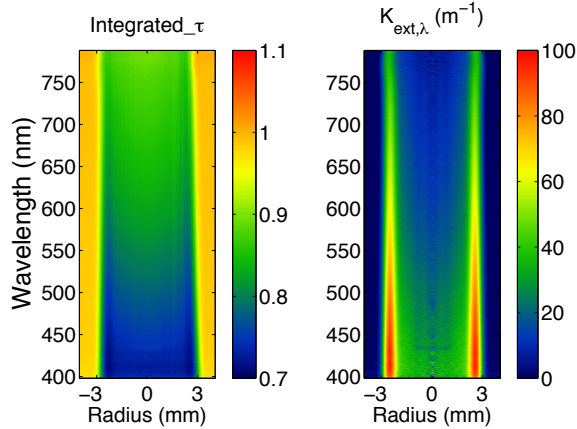
Fig. 5.13. Integrated transmissivity τ (left) and extinction coefficient $K_{ext,\lambda}$ maps

(right) at a height of 35 mm above the burner for the 80% C_2H_4 flame.

Ideally, the transmissivity value outside the flame region should be one since there is no attenuating media. However, values from 0.99 to 1.01 were obtained since the LAMP image was taken at a time later than the TRANSMISSION image for the sake of overall experiment time, and the lamp intensity varied by ~ 2% over the entire measurement time of ~ 80 minutes. In post-processing, appropriate factors were multiplied to the LAMP image at each height to compensate for the small variation of lamp intensity and to ensure unity in the integrated_τ map outside the flame region. The line-of-sight spectral transmissivity $\tau_\lambda(y)$ at a distance of y from the flame center can be calculated by Eq. (5.3.2) [Liu 2013].

$$\tau_\lambda(y) = \exp\left[-\int_{-\sqrt{R^2-y^2}}^{\sqrt{R^2-y^2}} K_{ext,\lambda}(x,y)\,dx\right] \qquad (5.3.2)$$

where R and x are the flame radius and distance along the optical path, respectively. $K_{ext,\lambda}$ is the spectral extinction coefficient. Since the flame is axisymmetric, the spectral extinction coefficients $K_{ext,\lambda}$ can be determined by Eq. (5.3.3).

$$K_{ext,\lambda} = Abelinv\left(-\ln\left(\tau_\lambda\right)\right)/L \qquad (5.3.3)$$

where $Abelinv(x)$ indicates that an Abel-inversion operated on an axisymmetric image x, L is the effective extinction length that equals the depth of the projection onto a single pixel, and $\ln(\tau_\lambda)$ is the natural log of the spectral transmissivity image τ_λ. A three-point inversion algorithm [Martin 2002; Dasch 1992] was built into the OMA software to perform the Abel inversion. Since Abel inversion is very sensitive to noise, all images were 2×2 binned to reduce noise and image processing time. The spatial projection L is 11.9 μm after the image binning. Gaussian smoothing using a one-dimensional kernel with σ = 5.71 over 21 pixels was also applied along the radial direction before inversion to reduce the noise of the inverted images. Gaussian smoothing was chosen to effectively reduce noise while keeping the shape of the distribution. The smoothing parameters were

chosen so that the processing time is relatively short and further smoothing did not improve the image signal/noise ratio significantly. The derived $K_{ext,\lambda}$ map with units of m$^-$^{1} is shown in Fig. 5.13 on the right.

The above images show varying spectral information at a fixed spatial height. A full flame scan was performed by traversing the flame vertically over the visible flame height. A two-dimensional spatial distribution can be composited with scans at different heights for the specific wavelengths. For illustration, images of line-of-sight transmissivity τ and extinction coefficient $K_{ext,\lambda}$ maps of the 80% flame at several discrete wavelengths (450, 550, 600 and 700 nm) are shown in Fig. 5.14 with corresponding radial line plots at 30 mm and 50 mm HAB. As can be seen, the transmissivity outside the flame region is very close to one as expected. Extinction gradually decreases with increasing wavelength, and greater extinction occurs on the wings of the flame as suggested by the $K_{ext,\lambda}$ maps. The peaks of the $K_{ext,\lambda}$ maps at different wavelengths also line up very well, which indicates that there is no obvious chromatic aberration associated with the optical setup.
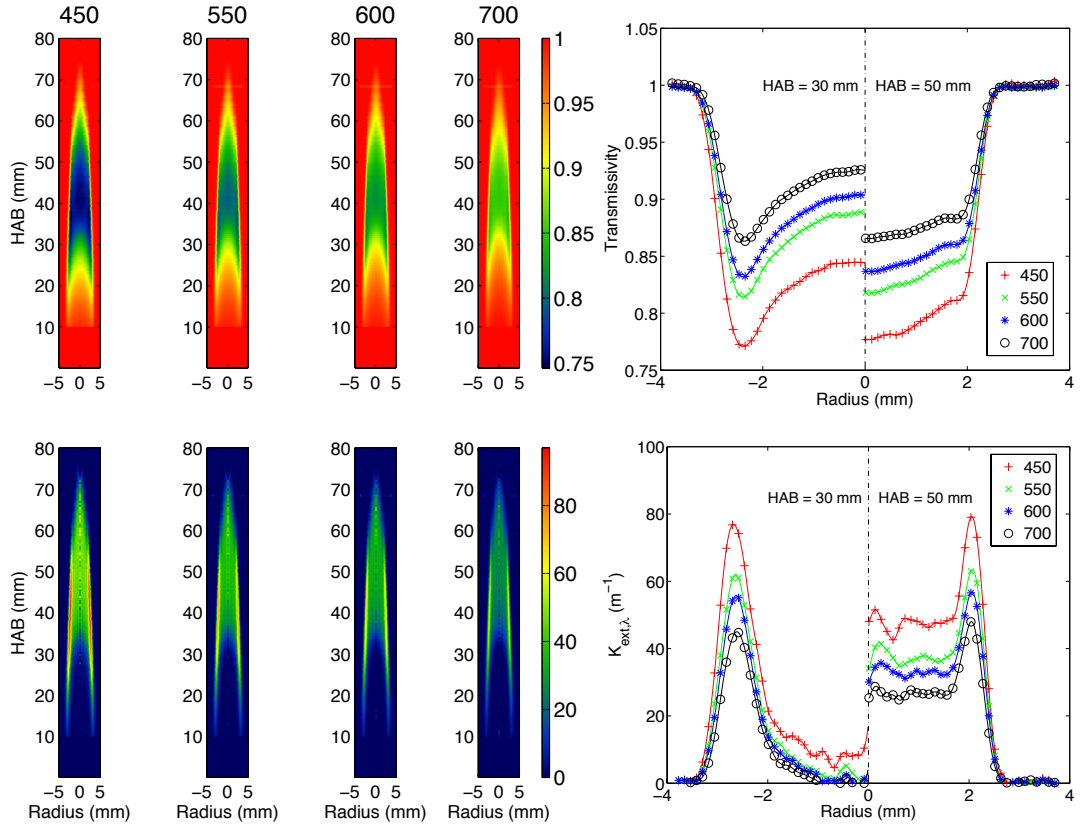
Fig. 5.14. Line-of-sight integrated transmissivity (top) and extinction coefficient $K_{ext,\lambda}$ (m^{-1}) maps (bottom) at 450, 550, 600 and 700 nm (from left to right) for the 80% flame. Corresponding radial line profiles are also shown at HAB = 30 mm (left) and 50 mm (right).

5.4   Two-dimensional determination of the dispersion exponent

The dispersion exponent, α, is fundamentally dependent on the soot refractive index m and is introduced to describe the wavelength dependence of the soot absorption coefficient as shown by Eq. (5.4.1) [Hottel 1932; Millikan 1961; De Iuliis 1998b].

151

$$K_{abs,\lambda} = \frac{36\pi E(m) f_v}{\lambda} \propto \frac{1}{\lambda^\alpha} \qquad (5.4.1)$$

where $K_{abs,\lambda}$ is the soot absorption coefficient, $E(m)$ is the absorption function of soot which depends on the refractive index m, f_v is the soot volume fraction and λ is wavelength. α is a non-unity value since $E(m)$ also has a wavelength dependence to be determined. Assuming the validity of Kirchhoff's law, i.e., at thermal equilibrium, the emitted radiation is balanced with absorbed energy. The dispersion exponent can be related to the soot spectral emissivity via Eq. (5.4.2) [Hottel 1932; De Iuliis 1998a; Zhao 1998], where L is the extinction length. Given $K_{abs,\lambda}L$ is a small value, the first order of the Taylor expansion can be used with good accuracy.

$$\varepsilon_\lambda = 1 - \exp\left(-K_{abs,\lambda}L\right) \propto K_{abs,\lambda} \propto \frac{1}{\lambda^\alpha} \quad (5.4.2)$$

The value of α is very important to color-ratio pyrometry, and has been measured as a function of H/C ratio of soot and reported to vary with flame downstream locations. It has been reported to be ~ 2.2 for young soot with H/C ratio of 0.5 - 0.6, and the value decreased to ~ 1.2 for more mature soot with H/C ratio of ~ 0.2 [Millikan 1961; D'Alessio 1972; Shaddix 2005]. The value of 1.2 falls into the range of 0.65-1.43 that was measured by many studies with different fuels and summarized in [Zhao 1998] for the visible light range. In our previous work [Kuhn 2011], a constant value of 1.38 was used for temperature measurement in the same flame as investigated here. However, this

value is obtained from different flames and neglects spatial variations in flames [De Iuliis 1998a; Zhao 1998]. To the best of the author's knowledge, all ratio pyrometry studies to date have used some "nominal" constant value for α. It is the objective of this study to obtain a spatially resolved two-dimensional α map and to determine more accurate temperatures using the two-dimensional α map rather than a single value.

The value of α is determined from exponential fitting of the absorption coefficient $K_{abs,\lambda}$ as shown in Eq. (5.4.1). $K_{abs,\lambda}$ is obtained from the spec-LOSA measurement of $K_{ext,\lambda}$ coupled with a correction for the scattering/absorption ratio $\rho_{sa,\lambda}$ as shown by Eq. (5.4.3).

$$K_{abs,\lambda} = \frac{K_{ext,\lambda}}{1 + \rho_{sa,\lambda}} \qquad (5.4.3)$$

The scattering/absorption ratio $\rho_{sa,\lambda}$ was determined from the primary particle sizes determined with TiRe-LII and the $R_{g,eff}$ determined from the 2-D MALS measurements. The differential scattering cross section of an ensemble of polydisperse aggregates was calculated by Eq. (5.4.4) considering the aggregate size distribution. The total scattering cross section was calculated by integrating the differential cross section over the 4π angle as Eq. (5.4.5) [Sorensen 2001].

$$\frac{d\sigma_{sca}^{agg}}{d\Omega} = \int_{N=1}^{N=\infty} n(N) \frac{d\sigma_{sca}^{pp}}{d\Omega} N^2 S(qR_g(N)) dN = \frac{d\sigma_{sca}^{pp}}{d\Omega} M_2 \left(1 - \frac{1}{3} q^2 R_{g,eff}^2\right) \qquad (5.4.4)$$

$$\sigma_{sca}^{agg} = \int_0^{2\pi} \int_{-1}^1 \frac{d\sigma_{sca}^{agg}}{d\Omega} \sin^2(\phi) d\cos(\phi) d\theta = \frac{8}{3} M_2 \pi k^4 a^6 F(m) \left(1 + \frac{4}{3D} k^2 R_{g,eff}^2\right)^{-\frac{D}{2}}$$

(5.4.5)

where the structure factor $S(qR_g)$ takes the Guinier form by assuming the majority of the aggregates fall into the Guinier regime, $\frac{d\sigma_{sca}^{pp}}{d\Omega} = k^4 a^6 F(m)$ is the Rayleigh differential scattering cross section of a primary particle, k is the wave vector, M_i is the ith moment as defined previously, a is the primary particle radius, $R_{g,eff}$ is the effective soot aggregate radius of gyration, D is the soot fractal dimension (a commonly used value of 1.8 is assumed), and $F(m)$ is the scattering function of refractive index m. The total absorption of an ensemble of polydisperse aggregates was calculated by Eq. (5.4.6).

$$\sigma_{abs}^{agg} = \int_{N=1}^{N=\infty} 4\pi N k a^3 E(m) n(N) dN = 4 M_1 \pi k a^3 E(m)$$

(5.4.6)

where $E(m)$ is the absorption function of refractive index m. Other parameters are as defined previously. The scattering/absorption ratio $\rho_{sa,\lambda}$ can then be calculated as Eq. (5.4.7).

$$\rho_{sa,\lambda} = \frac{\sigma_{sca}^{agg}}{\sigma_{abs}^{agg}} = \frac{\frac{8}{3}M_2\pi k^4 a^6 F(m)\left(1+\frac{4}{3D}k^2 R_{g,eff}^2\right)^{-\frac{D}{2}}}{4M_1\pi ka^3 E(m)}$$

$$= \frac{M_2/M_1}{\left(M_{2+2/D}/M_2\right)^{\frac{D}{2}}}\frac{\frac{8}{3}N_{eff}^2\pi k^4 a^6 F(m)\left(1+\frac{4}{3D}k^2 R_{g,eff}^2\right)^{-\frac{D}{2}}}{4N_{eff}\pi ka^3 E(m)} \qquad (5.4.7)$$

The effective number of primary particles N_{eff} that compose an aggregate is defined by Eq. (5.4.8), and is shown to equal the ratio of the two moments, which also validates the third equal sign of Eq. (5.4.7).

$$N_{eff} = k_0\left(\frac{R_{g,eff}}{a}\right)^D = \left(\frac{M_{2+2/D}}{M_2}\right)^{\frac{D}{2}} \qquad (5.4.8)$$

The value of N_{eff} is readily available using the measured effective radius of gyration $R_{g,eff}$ and primary particle radius a. There is a large discrepancy of the constant k_0 in the literature [Mountain 1988; Köylü 1995; Sorensen 1997]. Its value is assumed to be the more often used 2.41 (equivalent to $k_f = 8.5$) as measured in Ref. [Köylü 1995]. The ratio of $F(m)/E(m)$ is curve fitted to a second order polynomial in the visible range based on the tabulation available in Ref. [Krishnan 2000], and is also shown in Table 5.1 here for completeness.

Table 5.1

λ (nm)	351.2	405.0	457.9	488.0	514.5	632.8
$F(m)/E(m)$	0.63	0.76	0.87	0.93	0.98	1.17

As discussed in Ref. [Coderre 2011], this table of data is considered more appropriate for this work as opposed to other data measured from compressed soot pellets [Stagg 1993] or with soot morphology neglected [Chang 1990a]. The ratio $F(m)/E(m)$ serves as a scaling factor in the $\rho_{sa,\lambda}$ calculation and contributes only small uncertainty in the scattering correction given the small magnitude of $\rho_{sa,\lambda}$ [Coderre 2011]. In Eq. (5.4.7), the correction factor $(M_2/M_1)(M_{2+2/D}/M_2)^{-D/2}$, in conjunction with the use of effective radius of gyration, accounts for the aggregate polydisperse distribution. This factor can be determined once the aggregate distribution is known. In this work, we assume lognormal distribution with the geometric standard deviation $\sigma_g = 2$ and the median of the distribution $N_{med} = 30$ for the entire soot region. The correction factor is then evaluated to be 0.48 and is used in the calculation of $\rho_{sa,\lambda}$. This is certainly a simplification since the correction factor should vary with spatial location as the distribution changes. A rigorous approach is to use SEM sampling as discussed in [Coderre 2011] to determine the distribution and moments. However, performing extensive sampling over many points in a non-premixed flame to yield 2-D distributions of N_{med} and σ_g remains an interesting challenge. Nevertheless, as will be shown in next section, the scattering correction has a rather small effect on the derived pyrometry temperature.

The dispersion exponent is obtained by exponentially fitting $K_{ext,\lambda}$ and $1+\rho_{sa,\lambda}$ separately, and then subtracting one from the other as expressed by Eq. (5.4.9)

$$\alpha = \alpha_{ext} - \alpha_{sa} \quad (5.4.9)$$

156

where α_{ext} and α_{sa} are the fitted exponents for $K_{ext,\lambda}$ and $1+\rho_{sa,\lambda}$ as expressed by Eq. (5.4.10) and Eq. (5.4.11) respectively.

$$K_{ext,\lambda} \propto \frac{1}{\lambda^{\alpha_{ext}}} \qquad (5.4.10)$$

$$1+\rho_{sa,\lambda} \propto \frac{1}{\lambda^{\alpha_{sa}}} \qquad (5.4.11)$$

The value of α obtained in this way is checked to be very close to that obtained by correcting the scattering component first via Eq. (5.4.3) and then performing the exponential fitting. Calculating α_{ext} and α_{sa} separately has the advantage of showing both values and helps to estimate the uncertainties. The exponential fitting of $K_{ext,\lambda}$ at one flame location (1.5 mm radius at 35 mm HAB in the 80% C_2H_4 flame) is plotted in Fig. 5.15 (left) as an example. Since the lamp signal used in the spec-LOSA experiment is relatively low at wavelengths below 450 nm, only wavelengths greater than 450 nm are used for the exponential fitting. The determined α_{ext} at this location is 1.299 with R^2 value of 0.9907. An exponential fitting of $1+\rho_{sa,\lambda}$ is also plotted in Fig. 5.15 (right) as an example. The $R_{g,eff}$ and a used in the calculation are 100 nm and 40 nm respectively. The calculated $\rho_{sa,\lambda}$ is in the range of $0.07 \sim 0.12$ and the determined α_{sa} is 0.101.
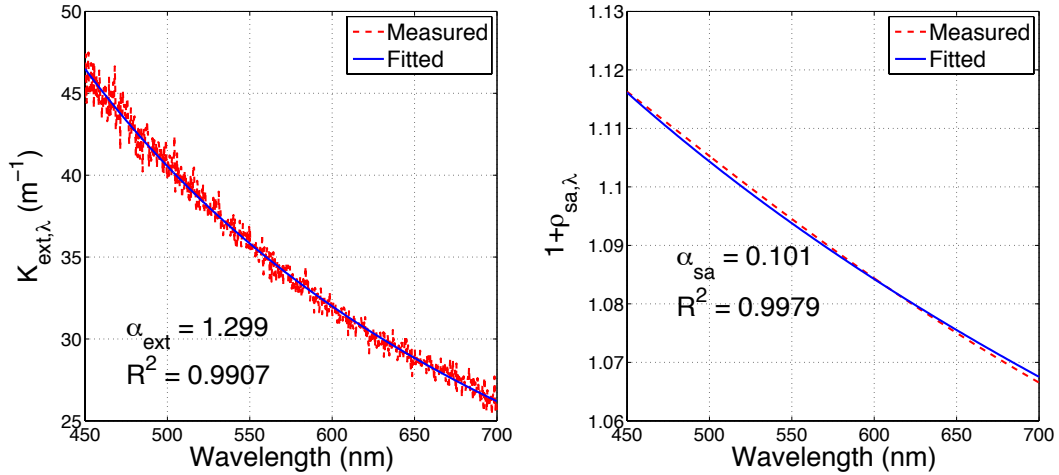
Fig. 5.15. An illustration of the exponential fitting of $K_{ext,\lambda}$ (left) and $1+\rho_{sa,\lambda}$ with

$R_{g,eff}$ = 100 nm and a = 40 nm (right).

The same fitting procedure was then performed for the entire soot region of the

flame to obtain the 2-D spatially resolved α. Multiple measurements on the same flame

are required for such determination and their results are summarized in Fig. 5.16. The

primary particle diameter (D_p) has been measured in previous work by time-resolved

laser induced incandescence (TiRe-LII) [Connelly 2009]. The effective radius of gyration

($R_{g,eff}$) was measured by 2-D MALS as described in Section 5.2. The 2-D extinction

coefficients were measured by spec-LOSA as described in Section 5.3 and the profile at

500 nm is shown as an example. The flame emission is captured by a color digital single

lens reflex (DSLR) camera (Nikon D300s). The radially resolved differential flame

emission shown here is obtained by Abel-inverting the line-of-sight integrated emission

image, which represents the emission signal from the flame sheet with thickness of the

spatial projection of a binned pixel (11.9 μm). As can be seen, all measurements yield

very good spatial overlap. A combination of these measurements was used to evaluate the

spatially resolved dispersion exponent α at the spatial region where all measurements overlap.
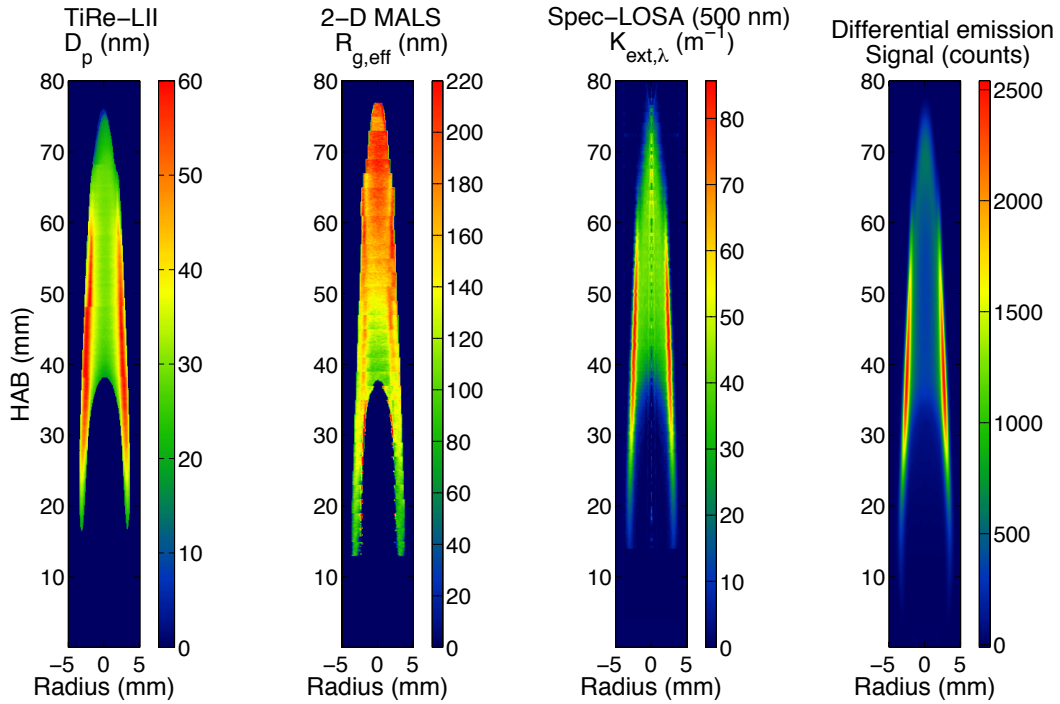
Fig. 5.16. Soot measurements of primary particle diameter D_p, effective radius of gyration $R_{g,eff}$, spectral extinction coefficients $K_{ext,\lambda}$ (only 500 nm is shown for illustration) and radially resolved differential emission signal on the 80% C_2H_4 flame using TiRe-LII, 2-D MALS, spec-LOSA and Abel-inversion of direct incandescence image, respectively.

The exponential fittings of $K_{ext,\lambda}$ and $1+\rho_{sa,\lambda}$ for the full flame region return R^2 values generally greater than 0.98. R^2 values of α_{ext} decrease to 0.9 along the flame centerline due to the noisy Abel-inverted signals at this location. The spatially resolved

two-dimensional dispersion exponent maps for α, α_{ext} and α_{sa}, along with their R^2 maps are shown in Fig. 5.17. The measured dispersion exponent is shown to vary with spatial location inside the flame corresponding to different degrees of soot aging. The determined α_{ext} value ranges from ~ 1 to ~ 2 across the entire sooty region, and is much larger than the α_{sa} values from 0.03 to 0.16. The centerline α_{sa} values peak at 0.07 around HAB = 48 mm and decrease to 0.06 towards both upstream and downstream at HAB = 41 mm and 61 mm respectively. In Ref. [Migliorini 2011], $\rho_{sa,\lambda}$ values were determined rigorously by considering the size distribution and reported for three heights (42 mm, 50 mm and 55 mm) above the burner along the centerline of a similar ethylene/air coflow laminar diffusion flame (i.e., the Gülder flame). Adding one to the reference $\rho_{sa,\lambda}$ values and then doing an exponential fit, yielded α_{sa} values of 0.083, 0.088 and 0.070 for the three heights respectively. Our measured values are not directly comparable to the literature values given the fact that the Gülder burner is different from our burner, and the Gülder flame operates at different flow rates without N_2 dilution. However, it is still interesting to see that the α_{sa} values obtained in our work and from Ref. [Migliorini 2011] are comparable and differ by less than ~ 0.02. The value of α, after subtracting α_{sa} from α_{ext}, is found to be ~ 2 at upstream locations where the young soot is formed, and is as small as ~ 0.9 on the wings of the flame where the soot is more mature.
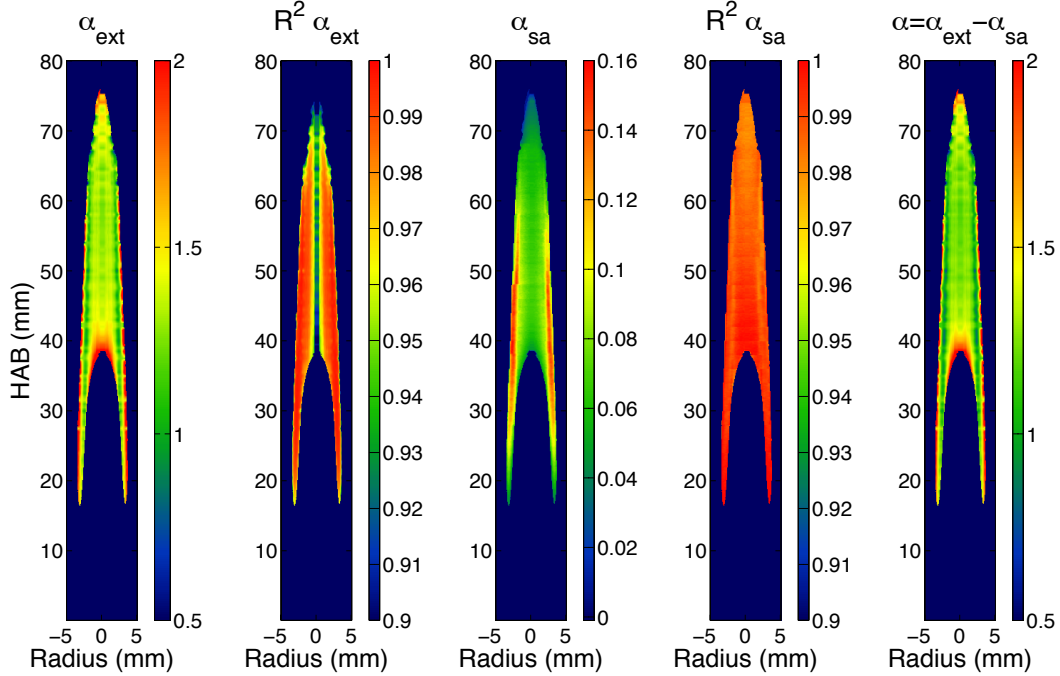
Fig. 5.17. Two-dimensional maps of α_{ext}, α_{sa} and their corresponding R^2 maps, and the dispersion exponent α for the 80% C_2H_4 flame.

5.5 Soot ratio pyrometry and temperature uncertainty

In our previous work as discussed in Ref. [Kuhn 2011], soot emissivity was assumed to vary with $\lambda^{-1.38}$. Using the results from the previous section, the soot spectral emissivity can be calculated via Eq. (5.4.2) using measured α on a pixel-by-pixel basis. Lookup tables that correlate color-ratio and temperature are also calculated for each pixel location using Eq. (5.5.1),

$$\frac{S_{F_1}}{S_{F_2}} = \frac{\int \lambda^{-5} \eta_{F_1}(\lambda)\varepsilon(\lambda)\left[\exp(hc/\lambda kT)-1\right]^{-1} d\lambda}{\int \lambda^{-5} \eta_{F_2}(\lambda)\varepsilon(\lambda)\left[\exp(hc/\lambda kT)-1\right]^{-1} d\lambda} \qquad (5.5.1)$$

where η_F is the detector spectral response of the DSLR camera with a BG glass filter in the setup and is shown in [Ma 2014]. The camera characterization followed the same procedure as discussed in [Kuhn 2011]. The measured α and a constant value of 1.38 along with their corresponding pyrometry temperatures and temperature differences are shown in Fig. 5.18.
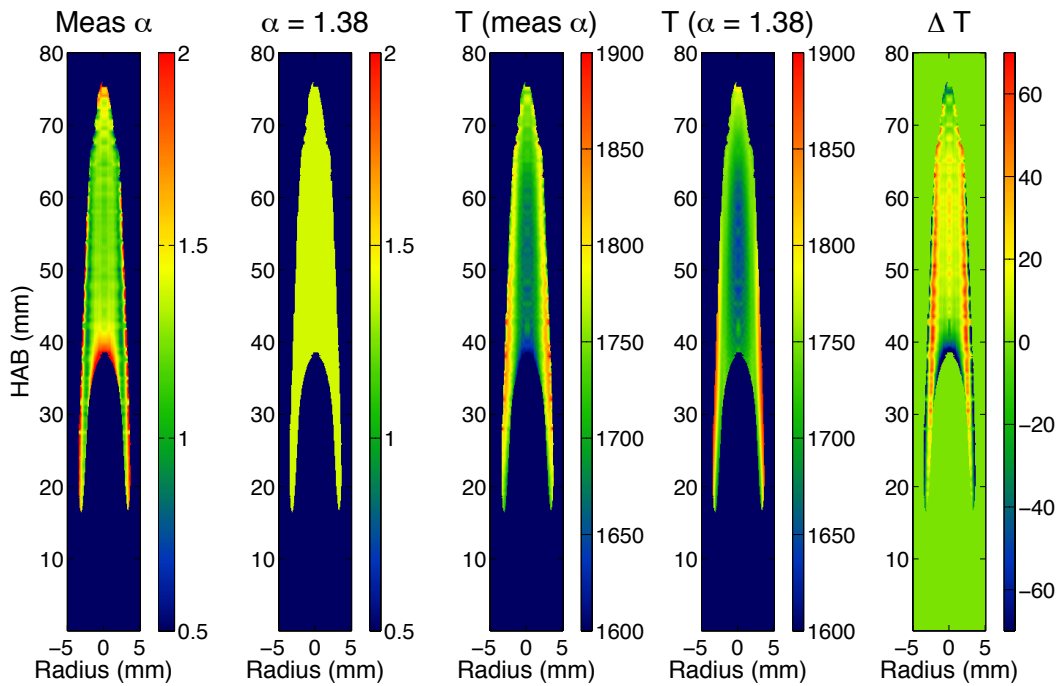
Fig. 5.18. Measured and constant dispersion exponent and their corresponding ratio-pyrometry temperatures and temperature differences.

The new temperature based on measured α has higher wing temperatures and lower upstream centerline temperatures than the old temperature based on a constant value of 1.38. The centerline temperature of both measurements is plotted in Fig. 5.19. The new temperature is more physically reasonable than the old measurements since the

162

centerline temperature is expected to monotonically increase with HAB in the soot-containing region. The higher temperatures at heights below ~ 40 mm in the old measurements resulted from neglecting the spatial variation of α and the value of 1.38 being smaller than the true α value in this region.
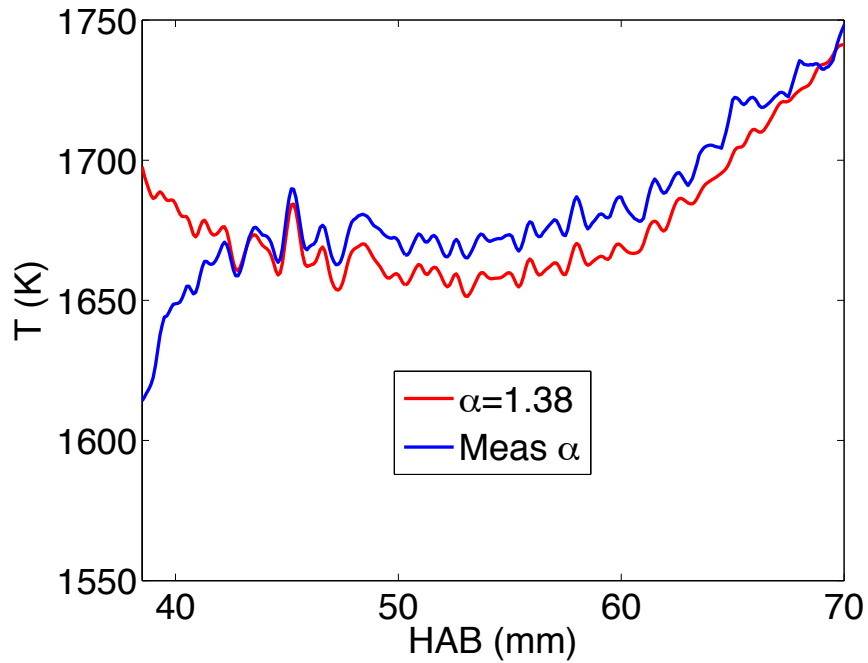
Fig. 5.19. Centerline pyrometry temperatures using measured the dispersion exponent α and a constant value of 1.38.

The new temperature based on the measured α is believed to be the most accurate measurement on this flame to date. The factors affecting the temperature uncertainties considered here are mainly the uncertainties of α. The uncertainty of α_{ext} is expected to be small given the straightforward and well-established LOSA method and good data quality (i.e., excellent goodness of fitting). The uncertainty of α_{sa}, however, is expected to be relatively large given that several assumptions and sources of uncertainty are included in deriving it. For example, Eq. (5.4.7) is based on the RDG approximation with

uncertainty no better than 10% [Farias 1996; Migliorini 2011]; the uncertainties in the fundamental soot optical properties such as $E(m)$ and $F(m)$, and the uncertainty of k_0 all add uncertainties to α_{sa}, which makes formal uncertainty analysis particularly hard. However, the exponent α_{sa} generally ranges from 0.03 to 0.16 in the flame and is much smaller than α_{ext}. A sensitivity analysis on the effect of the dispersion exponent on the pyrometry-derived temperature has been performed. Varying dispersion exponent from 1 to 1.5 with an increment of 0.1 was used to calculate the soot spectral emissivity and therefore the temperature/color-ratio lookup tables. These lookup tables were then applied on the same measured color-ratio signal taken along the flame centerline to infer temperature. The derived temperature and the dispersion exponent being used are plotted in Fig. 5.20. As can be seen, a variation of 0.1 in the value of α results in ~ 10 K change in the pyrometry-derived temperature.
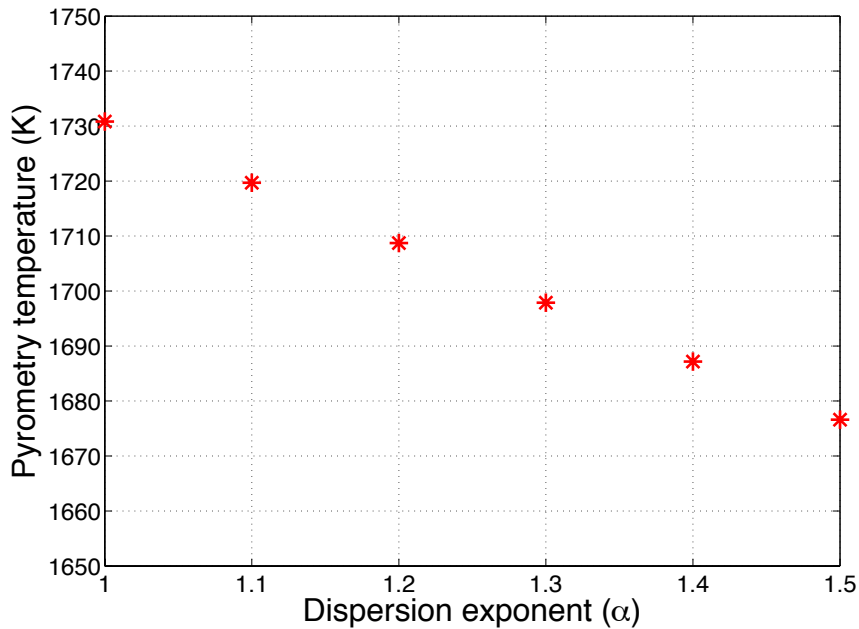
Fig. 5.20. The sensitivity of pyrometry measured temperature to the value of the

dispersion exponent α.

Since the value of α_{sa} is positive, the upper limit of α would be just α_{ext}. The temperature based on α_{ext}, in the case of neglecting the scattering component, could serve as a lower limit of the pyrometry-derived temperature given the fact that the temperature decreases with increasing α as seen in Fig. 5.20. The temperature based on α_{ext} without the scattering correction (the lower limit), the temperature based on α and their differences are shown in Fig. 5.21. The largest temperature difference of ~ 20 K occurs on the wings, and the temperature difference on the centerline is only ~ 8 K. If the current measured value of α_{sa} is larger than the actual value, the true temperature must be smaller than T(α) and greater than T(α_{ext}) as shown in Fig. 5.21. If the measurement of α_{sa} on the flame centerline is smaller than the actual value by 0.1 ($\sim 100\%$), the true temperature should be greater than the current T(α) by ~ 10 K according to the sensitivity analysis.
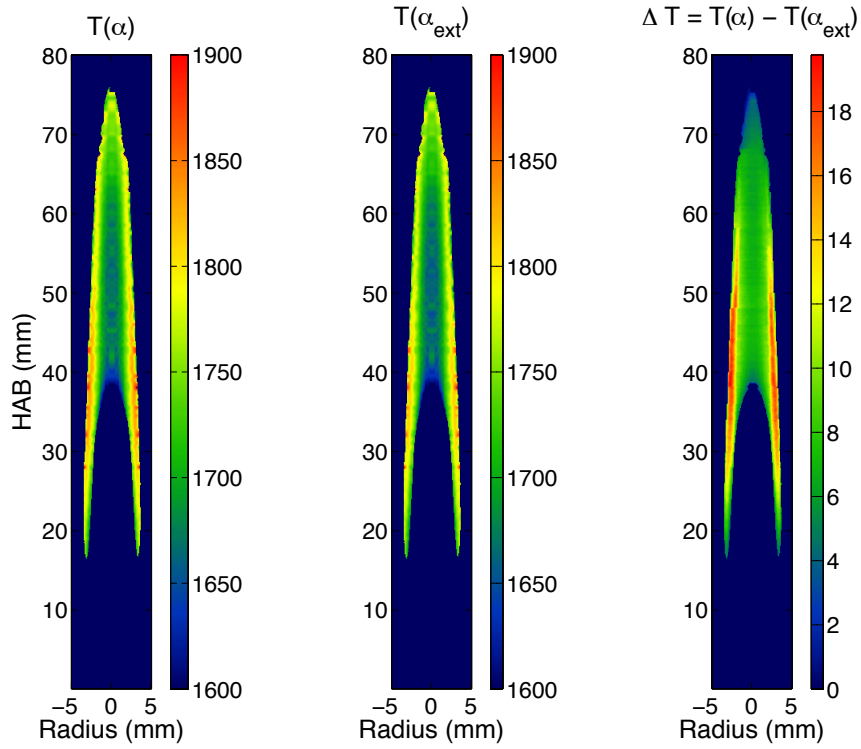
Fig. 5.21. The pyrometry temperatures based on α and α_{ext} and their differences.

5.6   Conclusions

Combined optical characterizations of coflow laminar diffusions have been performed using multiple techniques. Traditional point multi-angle light scattering has been extended to planar measurements. Spatially resolved soot radius of gyration was reported over the full flame region. Line-of-sight integrated extinction measurements were performed using spec-LOSA, from which two-dimensional spectral extinction coefficients were obtained after an Abel-inversion. The spatially resolved dispersion exponent, α, was obtained in two dimensions by combining the results from multiple techniques. It was shown that the value of α varies with the degree of soot aging. A large value of $\alpha \sim 2$ was obtained for young soot particles and small value of ~ 0.9 was

obtained for soot aggregates along the wings. The measured α was used to calculate soot spectral emissivities on a pixel-by-pixel basis and the pyrometry temperature measurement was improved by using the spatially resolved α compared with using a "nominal" constant value. Finally, uncertainty analysis showed that the uncertainties in α_{sa} have a relatively small impact on pyrometry temperature on the order of $\sim$ 20 K, and a lower temperature limit has been established in the case of neglecting the scattering component.

6 Summary and future directions

A color-ratio pyrometry technique using consumer grade digital single lens reflex cameras was developed for thin-filament and soot temperature measurement. The spectral responses of the cameras' built-in RGB Bayer pattern color filter array have been accurately measured, which turns the color cameras into color-ratio pyrometers with single-shot measurement capability.

A novel absolute light calibration technique using S-type thermocouples was also developed. The spectral emissivities of Platinum have been measured in the visible range. The thermocouple cylindrical junction can be used as a Lambertian emitter with temperature readily obtained from the thermocouple readings. The spectral radiance of the thermocouple junction can then be calculated using Planck's radiation equation and used as a light intensity calibration source similar to a blackbody source or a Tungsten lamp.

Thin-filament pyrometry has been further investigated and its accuracy and uncertainties have been quantified. Two approaches, namely the intensity-ratio approach and color-ratio approach, have been reviewed and their potential error sources have been identified and examined. The accuracy of the thin-filament measurements has been compared against N_2 CARS measurements in well-calibrated flames. Uncertainty analysis has also been performed to suggest possible ways to reduce uncertainties.

The developed pyrometry and absolute light intensity calibration techniques have been used in the microgravity SLICE experiments for soot temperature and volume fraction measurements. It was found that, for CH_4 laminar diffusion flames, the peak soot volume fraction increased by a factor of 6 from 1-g to 0-g due to removal of the

buoyancy effect. The distribution of soot was also found to have a tendency of propagating from the centerline of the flame at 1-g to the wings at 0-g. The flame temperature in 0-g is lower than its 1-g counterpart due to higher soot loading and more radiation loss. Longer residence time in 0-g is expected and has been verified by computational simulation, and it is considered as the major reason for the different sooting behaviors between 1-g and 0-g. A similar trend has been successfully captured by the computational model. However, the disagreement on the soot volume fraction is still large. More advanced reabsorption submodels will be introduced, and the soot surface growth coefficient will be adjusted to improve the accuracy of the predictions.

As a pre-investigation of the CLD flame experiment, the pressure effects on coflow laminar diffusion flames have been investigated both experimentally and computationally. CH* chemiluminescence and thin-filament pyrometry were performed to measure the flame shape and temperature respectively. The experimental results were compared with computations and found that the computational model is capable of predicting flame shapes and temperatures accurately under elevated pressures, though the lift-off height is under predicted for flames with higher dilution levels.

A 2-D multi-angle light scattering technique was developed to measure soot radius of gyration in the Yale standard coflow laminar diffusion flames. The technique, based on Guinier analysis, was extended from point measurements using proper image processing techniques. The radius of gyration was found to monotonically increase with height above the burner along the centerline from 80 nm to 160 nm and 100 nm to 200 nm for the 60% and 80% flames respectively. Spectrally resolved line-of-sight attenuation measurements have also been performed in the same flames over the full

flame. Radially resolved extinction profiles were obtained via Abel inversion. The measurements of soot radius of gyration and soot primary particle sizes have been combined to estimate the scattering/absorption ratio, and used to correct the extinction measurements to obtain the absorption coefficient. The absorption coefficient was then fitted using an exponential curve to determine the dispersion exponent over the full flame. The 2-D map of dispersion exponent clearly suggests that the wavelength dependence of the spectral emissivity of young soot and mature soot are different. Using a "nominal" constant value is likely to introduce error in the color-pyrometry measurements of soot temperature. The measured 2-D dispersion exponent was used in conjunction with color-ratio pyrometry to improve the accuracy of soot temperature. Uncertainty analysis has also been performed suggesting the lower temperature limit is bounded by the case without any scattering/absorption correction.

The information presented in this dissertation thesis has attempted to develop optical diagnostic techniques and improve the knowledge and understanding of the combustion process. It should be possible to further expand on this work by refining the experimental measurements presented here. For example, in the current 2-D MALS experiment, the measured soot radius of gyration on flame wings may be problematic due to possible spatial mismatches among different images at these large gradient regions. It would be nice to perform point measurements with relatively high spatial resolution along the flame radius to verify the 2-D measurements on the flame wings. The current scattering/absorption correction neglects the primary particle size distribution within an aggregate. TEM sampling of soot aggregates is useful to determine soot morphology and could potentially improve the correction accuracy. The measurements on soot radius of

gyration are also potentially useful to improve the computational models for better soot simulation.

7 References

(08/2013a). http://www.intl-lighttech.com/applications/light-sources/tungsten-filament-lamps.

(08/2013b).

http://www.us.schott.com/advanced_optics/english/download/schott_bandpass_bg7_2008_us.pdf.

(12/2013). http://www.adelaide.edu.au/cet/isfworkshop/data-sets/laminar/.

(2013). http://srdata.nist.gov/its90/main/.

Anselmitamburini, U., G. Campari, G. Spinolo and P. Lupotto (1995). "A 2-color spatial-scanning pyrometer for the determination of temperature profiles in combustion synthesis reactions." Review of Scientific Instruments **66**(10): 5006-5014.

Beatrice, C., C. Bertoli, N. C. Cirillo, N. D. Giacomo and S. D. Stasio (1995). "Two-colour pyrometry measurements of soot loading in a diesel engine burning model fuels of varying quality." Combustion Science and Technology **110**(1): 321 - 339.

Bédat, B., A. Giovannini and S. Pauzin (1994). "Thin filament infrared pyrometry: instantaneous temperature profile measurements in a weakly turbulent hydrocarbon premixed flame." Experiments in Fluids **17**(6): 397-404.

Bennett, B. A. V., Z. Cheng, R. W. Pitz and M. D. Smooke (2008). "Computational and experimental study of oxygen-enhanced axisymmetric laminar methane flames." Combustion Theory and Modelling **12**: 497-527.

Bennett, B. A. V., C. S. McEnally, L. D. Pfefferle and M. D. Smooke (2000). "Computational and experimental study of axisymmetric coflow partially premixed methane/air flames." Combustion and Flame **123 (4)**: 522-546.

Blunck, D., S. Basu, Y. Zheng, V. Katta and J. Gore (2009). "Simultaneous water vapor concentration and temperature measurements in unsteady hydrogen flames." Proceedings of the Combustion Institute **32**(2): 2527-2534.

Böhm, B., J. H. Frank and A. Dreizler (2011). "Temperature and mixing field measurements in stratified lean premixed turbulent flames." Proceedings of the Combustion Institute **33**(1): 1583-1590.

Boslough, M. B. and T. J. Ahrens (1989). "A sensitive time-resolved radiation pyrometer for shock-temperature measurements above 1500-K." Review of Scientific Instruments **60**(12): 3711-3716.

Brooker, J. E., K. Jia, D. P. Stocker and L.-D. Chen (1999). "Influence of buoyant convection on the stability of enclosed laminar flames." Proceedings of the Fifth International Microgravity Combustion Workshop: 97-100.

Cao, S., B. A. V. Bennett and M. D. Smooke (in preparation).

Chang, H. and T. T. Charalampopoulos (1990a). "Determination of the Wavelength Dependence of Refractive Indices of Flame Soot." Proceedings: Mathematical and Physical Sciences **430**(1880): 577-591.

Chang, H. and T. T. Charalampopoulos (1990b). "Determination of the wavelength dependence of refractive-indexes of flame soot." Proceedings of the Royal Society of London Series a-Mathematical Physical and Engineering Sciences **430**(1880): 577-591.

Charest, M. R. J., C. P. T. Groth and Ö. L. Gülder (2011). "Effects of gravity and pressure on laminar coflow methane–air diffusion flames at pressures from 1 to 60 atmospheres." Combustion and Flame **158**(5): 860-875.

Cignoli, F., S. De Iuliis, V. Manta and G. Zizak (2001). "Two-dimensional two-wavelength emission technique for soot diagnostics." Applied Optics **40**(30): 5370-5378.

Coderre, A. R., K. A. Thomson, D. R. Snelling and M. R. Johnson (2011). "Spectrally resolved light absorption properties of cooled soot from a methane flame." Applied Physics B: Lasers and Optics **104**(1): 175-188.

Coffin, D. (2013). http://www.cybercom.net/~dcoffin/dcraw/.

Connelly, B. C. (2009). Quantitative characterization of steady and time-varying, sooting, laminar diffusion flames using optical techniques (Doctoral dissertation), Yale University.

Connelly, B. C., B. A. V. Bennett, M. D. Smooke and M. B. Long (2009a). "A paradigm shift in the interaction of experiments and computations in combustion research." Proceedings of the Combustion Institute **32**(1): 879-886.

Connelly, B. C., S. A. Kaiser, M. D. Smooke and M. B. Long (2005). Two-dimensional soot pyrometry with a color digital camera. Proceedings of the Joint Meeting of the U.S. Sections of the Combustion Institute, Drexel University, Philadelphia, PA.

Connelly, B. C., M. B. Long, M. D. Smooke, R. J. Hall and M. B. Colket (2009b). "Computational and experimental investigation of the interaction of soot and NO in coflow diffusion flames." Proceedings of the Combustion Institute **32**: 777-784.

Connelly, B. C., M. B. Long, M. D. Smooke, R. J. Hall and M. B. Colket (2009c). "Computational and experimental investigation of the interaction of soot and NOx in coflow diffusion flames." Proceedings of the Combustion Institute **32**: 777-784.

D'Alessio, A., F. Beretta and C. Venitozzi (1972). "Optical Investigations on Soot Forming Methane-Oxygen Flames." Combustion Science and Technology **5**(1): 263-272.

Dambach, E. M., B. A. Rankin, T. L. Pourpoint and S. D. Heister (2012). "Temperature Estimations in the Near-Flame Field Resulting from Hypergolic Ignition Using Thin Filament Pyrometry." Combustion Science and Technology **184**(2): 205-223.

Dasch, C. J. (1992). "One-dimensional tomography: a comparison of Abel, onion-peeling, and filtered backprojection methods." Applied Optics **31**(8): 1146-1152.

De Iuliis, S., M. Barbini, S. Benecchi, F. Cignoli and G. Zizak (1998a). "Determination of the soot volume fraction in an ethylene diffusion flame by multiwavelength analysis of soot radiation." Combustion and Flame **115**(1-2): 253-261.

De Iuliis, S., F. Cignoli, S. Benecchi and G. Zizak (1998b). "Determination of soot parameters by a two-angle Scattering-extinction technique in an ethylene diffusion flame." Applied Optics **37**(33): 7865-7874.

Deuflhard, P. (1974). "A modified Newton method for the solution of ill-conditioned systems of nonlinear equations with application to multiple shooting." Numerische Mathematik **22**(4): 289-315.

Diez, F. J., C. Aalburg, P. B. Sunderland, D. L. Urban, Z. G. Yuan and G. M. Faeth (2009). "Soot properties of laminar jet diffusion flames in microgravity." Combustion and Flame **156**(8): 1514-1524.

Dworkin, S. B., M. D. Smooke and V. Giovangigli (2009). "The impact of detailed multicomponent transport and thermal diffusion effects on soot formation in ethylene/air flames." Proceedings of the Combustion Institute **32**(1): 1165-1172.

Edwards, D. K. (1976). "Molecular gas band radiation." Advances in heat transfer. **12**: 115-193.

Farias, T. L., U. O. Köylü and M. G. Carvalho (1996). "Range of validity of the Rayleigh-Debye-Gans theory for optics of fractal aggregates." Applied Optics **35**(33): 6560-6567.

Gangopadhyay, S., I. Elminyawi and C. M. Sorensen (1991). "Optical structure factor measurements of soot particles in a premixed flame." Applied Optics **30**(33): 4859-4864.

Gelbard, F. and J. H. Seinfeld (1980a). "Simulation of multicomponent aerosol dynamics." Journal of Colloid and Interface Science **78**(2): 485-501.

Gelbard, F., Y. Tambour and J. H. Seinfeld (1980b). "Sectional representation for simulating aerosol dynamics." Journal of Colloid and Interface Science **76**: 541-556.

Giovangigli, V. and N. Darabiha (1988). Vector computers and complex chemistry combustion. Mathematical Modeling in Combustion and Related Topics. C.-M. Brauner and C. Schmidt-Lainé, Springer Netherlands. **140:** 491-503.

Glasbey, C. A. and K. V. Mardia (1998). "A review of image-warping methods." Journal of Applied Statistics **25**(2): 155-171.

Glassman, I. (1989). "Soot formation in combustion processes." Proceedings of the Combustion Institute **22**(1): 295-311.

Gordon, R. L., C. Heeger and A. Dreizler (2009). "High-speed mixture fraction imaging." Applied Physics B: Lasers and Optics **96**(4): 745-748.

Greenberg, P. S. and J. C. Ku (1997a). "Soot volume fraction imaging." Applied Optics **36**(22): 5514-5522.

Greenberg, P. S. and J. C. Ku (1997b). "Soot volume fraction maps for normal and reduced gravity laminar acetylene jet diffusion flames." Combustion and Flame **108**(1–2): 227-230.

176

Hall, R. J. (1993). "The radiative source term for plane-parallel layers of reacting combustion gases." Journal of Quantitative Spectroscopy and Radiative Transfer **49**(5): 517-523.

Hall, R. J. (1994). "Radiative dissipation in planar gas-soot mixtures." Journal of Quantitative Spectroscopy and Radiative Transfer **51**(4): 635-644.

Hall, R. J., M. D. Smooke and M. B. Colket (1997). Predictions of soot dynamics in opposed jet diffusion flames. Physical and Chemical Aspects of Combustion: A Tribute to Irvin Glassman (R.F. Sawyer and F.L. Dryer, Eds.), Combustion Science and Technology Book Series. Amsterdam, Gordon and Breach.

Harris, S. J. and A. M. Weiner (1983). "Surface growth of soot particles in premixed ethylene air flames." Combustion Science and Technology **31**(3-4): 155-167.

Haynes, B. S., H. Jander and H. G. Wagner (1980). "Optical studies of soot-formation processes in premixed flames." Berichte der Bunsengesellschaft für physikalische Chemie **84**(6): 585-592.

Hofmann, M., B. F. Kock, T. Dreier, H. Jander and C. Schulz (2008). "Laser-induced incandescence for soot-particle sizing at elevated pressure." Applied Physics B: Lasers and Optics **90**(3): 629-639.

Hottel, H. C. and F. P. Broughton (1932). "Determination of true temperature and total radiation from luminous gas flames." Industrial & Engineering Chemistry Analytical Edition **4**(2): 166-175.

Hura, H. S. and I. Glassman (1989). "Soot formation in diffusion flames of fuel/oxygen mixtures." Proceedings of the Combustion Institute **22**(1): 371-378.

Jeon, B.-H. and J. Choi (2010). "Effect of buoyancy on soot formation in gas-jet diffusion flame." Journal of Mechanical Science and Technology **24**(7): 1537-1543.

Jones, A. (2006). Light scattering in combustion. Light Scattering Reviews. A. Kokhanovsky, Springer Berlin Heidelberg**:** 393-444.

Kalt, P. A. M. and M. B. Long (2013). "OMA – Image processing for Mac OS X." http://www.oma-x.org.

Kaplan, C. R., E. S. Oran, K. Kailasanath and H. D. Ross (1996). "Gravitational effects on sooting diffusion flames." Proc. Combust. Inst. **26**(1): 1301-1309.

Kee, R. J., G. Dixon-Lewis, J. Warnatz, M. E. Coltrin and J. A. Miller (1986). "A Fortran computer code package for the evaluation of gas-phase, multicomponent transport properties." Sandia National Laboratories Report SAND86-8246.

Kee, R. J., J. A. Miller and T. H. Jefferson (1980). "Chemkin:A general-purpose, problem-independent, transportable, Fortran chemical kinetics code package." Report No. SAND80-8003, Sandia National Laboratories.

Kee, R. J., F. M. Rupley and J. A. Miller (1987). "The Chemkin thermodynamic data base." Sandia National Laboratories Report SAND87-8215.

Kee, R. J., J. Warnatz and J. A. Miller (1983). "A Fortran computer code package for the evaluation of gas-phase viscosities, conductivities, and diffusion coefficients." Report No. SAND83-8209, Sandia National Laboratories.

Kong, W. and F. Liu (2009). "Numerical study of the effects of gravity on soot formation in laminar coflow methane/air diffusion flames under different air stream velocities." Combustion Theory and Modelling **13**(6): 993 - 1023.

Kong, W. J. and F. S. Liu (2010). "Effects of gravity on soot formation in a coflow laminar methane/air diffusion flame." Microgravity Science and Technology **22**(2): 205-214.

Kook, S. and L. M. Pickett (2012). "Liquid length and vapor penetration of conventional, Fischer–Tropsch, coal-derived, and surrogate fuel sprays at high-temperature and high-pressure ambient conditions." Fuel **93**(0): 539-548.

Köylü, Ü. Ö., G. M. Faeth, T. L. Farias and M. G. Carvalho (1995). "Fractal and projected structure properties of soot aggregates." Combustion and Flame **100**(4): 621-633.

Krishnan, S. S., K. C. Lin and G. M. Faeth (2000). "Optical Properties in the Visible of Overfire Soot in Large Buoyant Turbulent Diffusion Flames." Journal of Heat Transfer **122**(3): 517-524.

Kuhn, P. B., B. Ma, B. C. Connelly, M. D. Smooke and M. B. Long (2011). "Soot and thin-filament pyrometry using a color digital camera." Proceedings of the Combustion Institute **33**(1): 743-750.

Levendis, Y. A., K. R. Estrada and H. C. Hottel (1992). "Development of multicolor pyrometers to monitor the transient-response of burning carbonaceous particles." Review of Scientific Instruments **63**(7): 3608-3622.

Liu, F., G. J. Smallwood and W. Kong (2011). "The importance of thermal radiation transfer in laminar diffusion flames at normal and microgravity." Journal of Quantitative Spectroscopy and Radiative Transfer **112**(7): 1241-1249.

Liu, F., K. A. Thomson and G. J. Smallwood (2013). "Soot temperature and volume fraction retrieval from spectrally resolved flame emission measurement in laminar

axisymmetric coflow diffusion flames: Effect of self-absorption." Combustion and Flame **160**(9): 1693-1705.

Luque, J. and D. R. Crosley (1996a). "Absolute CH concentrations in low-pressure flames measured with laser-induced fluorescence." Applied Physics B: Lasers and Optics **63**(1): 91-98.

Luque, J. and D. R. Crosley (1999). "LIFBASE: Database and spectral simulation (version 1.5)", SRI International Report MP 99-009 (1999).

Luque, J., J. B. Jeffries, G. P. Smith, D. R. Crosley, K. T. Walsh, M. B. Long and M. D. Smooke (2000). "CH(A-X) and OH(A-X) optical emission in an axisymmetric laminar diffusion flame." Combustion and Flame **122**(1-2): 172-175.

Luque, J., G. P. Smith and D. R. Crosley (1996b). "Quantitative CH determinations in low-pressure flames." Proceedings of the Combustion Institute **26**(1): 959-966.

Ma, B. and M. B. Long (2013). "Absolute light calibration using S-type thermocouples." Proceedings of the Combustion Institute **34**(2): 3531-3539.

Ma, B., G. Wang, G. Magnotti, R. S. Barlow and M. B. Long (2014). "Intensity-ratio and color-ratio thin-filament pyrometry: Uncertainties and accuracy." Combustion and Flame **161**(4): 908-916.

Martin, K. M. (2002). Acoustic modification of sooting combustion (Doctoral dissertation), The University of Texas at Austin.

Maun, J. D., P. B. Sunderland and D. L. Urban (2007). "Thin-filament pyrometry with a digital still camera." Applied Optics **46**(4): 483-488.

McEnally, C. S., A. M. Schaffer, M. B. Long, L. D. Pfefferle, M. D. Smooke, M. B. Colket and R. J. Hall (1998). "Computational and experimental study of soot formation in

a coflow, laminar ethylene diffusion flame." Proceedings of the Combustion Institute **27**(Vol. 1): 1497-1505.

Michelsen, H. A., F. Liu, B. F. Kock, H. Bladh, A. Boiarciuc, M. Charwath, T. Dreier, R. Hadef, M. Hofmann, J. Reimann, S. Will, P. E. Bengtsson, H. Bockhorn, F. Foucher, K. P. Geigle, C. Mounaïm-Rousselle, C. Schulz, R. Stirn, B. Tribalet and R. Suntz (2007). "Modeling laser-induced incandescence of soot: a summary and comparison of LII models." Applied Physics B: Lasers and Optics **87**(3): 503-521.

Migliorini, F., K. Thomson and G. Smallwood (2011). "Investigation of optical properties of aging soot." Applied Physics B: Lasers and Optics **104**(2): 273-283.

Millikan, R. C. (1961). "Optical properties of soot." Journal of the Optical Society of America **51**(6): 698-699.

Mountain, R. D. and G. W. Mulholland (1988). "Light scattering from simulated smoke agglomerates." Langmuir **4**(6): 1321-1326.

Neuer, G. and G. Jaroma-Weiland (1998). "Spectral and total emissivity of high-temperature materials." International Journal of Thermophysics **19**(3): 917 - 929.

Oltmann, H., J. Reimann and S. Will (2010). "Wide-angle light scattering (WALS) for soot aggregate characterization." Combustion and Flame **157**(3): 516-522.

Oltmann, H., J. Reimann and S. Will (2012). "Single-shot measurement of soot aggregate sizes by wide-angle light scattering (WALS)." Applied Physics B: Lasers and Optics **106**(1): 171-183.

Panagiotou, T., Y. Levendis and M. Delichatsios (1996). "Measurements of particle flame temperatures using three-color optical pyrometry." Combustion and Flame **104**(3): 272-287.

Patton, R. A., K. N. Gabet, N. Jiang, W. R. Lempert and J. A. Sutton (2012). "Multi-kHz mixture fraction imaging in turbulent jets using planar Rayleigh scattering." Applied Physics B: Lasers and Optics **106**(2): 457-471.

Pitts, W. M. (1996). "Thin-filament pyrometry in flickering laminar diffusion flames." Proceedings of the Combustion Institute **26**(1): 1171-1179.

Pitts, W. M., K. C. Smyth and D. A. Everest (1998). "Effects of finite time response and soot deposition on thin filament pyrometry measurements in time-varying diffusion flames." Proceedings of the Combustion Institute **27**(1): 563-569.

Reimann, J., S.-A. Kuhlmann and S. Will (2010). "Investigations on soot formation in heptane jet diffusion flames by optical techniques." Microgravity Science and Technology **22**(4): 499-505.

Reimann, J., S. A. Kuhlmann and S. Will (2009). "2D aggregate sizing by combining laser-induced incandescence (LII) and elastic light scattering (ELS)." Applied Physics B: Lasers and Optics **96**(4): 583-592.

Reuter, D., B. R. Daniel, J. Jagoda and B. T. Zinn (1986). "Periodic mixing and combustion processes in gas fired pulsating combustors." Combustion and Flame **65**(3): 281-290.

Rohsenow, W. M., J. P. Hartnett and Y. I. Cho (1988). Handbook of Heat Transfer. New York, McGraw-Hill.

Schulz, C., B. F. Kock, M. Hofmann, H. Michelsen, S. Will, B. Bougie, R. Suntz and G. Smallwood (2006). "Laser-induced incandescence: recent trends and current questions." Applied Physics B: Lasers and Optics **83**(3): 333-354.

Shaddix, C. R., Á. B. Palotás, C. M. Megaridis, M. Y. Choi and N. Y. C. Yang (2005). "Soot graphitic order in laminar diffusion flames and a large-scale JP-8 pool fire." International Journal of Heat and Mass Transfer **48**(17): 3604-3614.

Smith, G. P., D. M. Golden, M. Frenklach, N. W. Moriarty, B. Eiteneer, M. Golderberg, C. T. Bowman, R. K. Hanson, S. Song, W. C. Gardiner, V. V. Lissianski and Z. Qin (1999). GRI-Mech 3.0; available at http://www.me.berkeley.edu/gri_mech.

Smooke, M. D. (1983). "Error estimate for the modified Newton method with applications to the solution of nonlinear, two-point boundary-value problems." Journal of Optimization Theory and Applications **39**(4): 489-511.

Smooke, M. D., M. B. Colket and R. J. Hall (1999). "Towards quantitative modeling of soot formation in coflow diffusion flames." Chemical and Physical Processes in Combustion: 344-347.

Smooke, M. D., R. J. Hall, M. B. Colket, J. Fielding, M. B. Long, C. S. McEnally and L. D. Pfefferle (2004). "Investigation of the transition from lightly sooting towards heavily sooting co-flow ethylene diffusion flames." Combustion Theory and Modelling **8**(3): 593-606.

Smooke, M. D., M. B. Long, B. C. Connelly, M. B. Colket and R. J. Hall (2005). "Soot formation in laminar diffusion flames." Combustion and Flame **143**(4): 613-628.

Snelling, D. R., K. A. Thomson, G. J. Smallwood and Ö. L. Gülder (1999). "Two-dimensional imaging of soot volume fraction in laminar diffusion flames." Applied Optics **38**(12): 2478-2485.

Snelling, D. R., K. A. Thomson, G. J. Smallwood, Ö. L. Gülder, E. J. Weckman and R. A. Fraser (2002). "Spectrally resolved measurement of flame radiation to determine soot temperature and concentration." AIAA Journal **40**(9): 1789-1795.

Sorensen, C. M. (2001). "Light scattering by fractal aggregates: A review." Aerosol Science and Technology **35**(2): 648-687.

Sorensen, C. M., J. Cai and N. Lu (1992). "Light-scattering measurements of monomer size, monomers per aggregate, and fractal dimension for soot aggregates in flames." Applied Optics **31**(30): 6547-6557.

Sorensen, C. M. and G. C. Roberts (1997). "The prefactor of fractal aggregates." Journal of Colloid and Interface Science **186**(2): 447-452.

Stagg, B. J. and T. T. Charalampopoulos (1993). "Refractive indices of pyrolytic graphite, amorphous carbon, and flame soot in the temperature range 25° to 600°C." Combustion and Flame **94**(4): 381-396.

Struk, P., D. Dietrich, R. Valentine and I. Feier (2003). Comparisons of gas-phase temperature measurements in a flame using thin-filament pyrometry and thermocouples. 41st Aerospace Sciences Meeting and Exhibit. Reno, Nevada, AIAA.

Sun, C. J., C. J. Sung, H. Wang and C. K. Law (1996). "On the structure of nonsooting counterflow ethylene and acetylene diffusion flames." Combustion and Flame **107**(4): 321-335.

Thomson, K. A., M. R. Johnson, D. R. Snelling and G. J. Smallwood (2008). "Diffuse-light two-dimensional line-of-sight attenuation for soot concentration measurements." Applied Optics **47**(5): 694-703.

Thomson, K. A., D. R. Snelling, G. J. Smallwood and F. Liu (2006). "Laser induced incandescence measurements of soot volume fraction and effective particle size in a laminar co-annular non-premixed methane/air flame at pressures between 0.5–4.0 MPa." Applied Physics B: Lasers and Optics **83**(3): 469-475.

Van der Vorst, H. A. (1992). "Bi-CGSTAB: A fast and smoothly converging variant of Bi-CG for the solution of nonsymmetric linear systems." SIAM Journal on Scientific and Statistical Computing **13**(2): 631-644.

Vilimpoc, V. and L. P. Goss (1989). "SiC-Based thin-filament pyrometry: Theory and thermal properties." Proceedings of the Combustion Institute **22**(1): 1907-1914.

Walsh, K. T., J. Fielding and M. B. Long (2000a). "Effect of light-collection geometry on reconstruction errors in Abel inversions." Optics Letters **25**(7): 457-459.

Walsh, K. T., J. Fielding, M. D. Smooke and M. B. Long (2000b). "Experimental and computational study of temperature, species, and soot in buoyant and non-buoyant coflow laminar diffusion flames." Proceedings of the Combustion Institute **28**: 1973-1979.

Walsh, K. T., J. Fielding, M. D. Smooke, M. B. Long and A. Linan (2005). "A comparison of computational and experimental lift-off heights of coflow laminar diffusion flames." Proceedings of the Combustion Institute **30**: 357-365.

Walsh, K. T., M. B. Long, M. A. Tanoff and M. D. Smooke (1998). "Experimental and computational study of CH, CH*, and OH* in an axisymmetric laminar diffusion flame." Proceedings of the Combustion Institute **27**(1): 615-623.

Will, S., S. Schraml and A. Leipertz (1996). "Comprehensive two-dimensional soot diagnostics based on laser-induced incandescence (LII)." Proceedings of the Combustion Institute **26**(2): 2277-2284.

Will, S., S. Schraml and A. Leipertz (1995). "Two-dimensional soot-particle sizing by time-resolved laser-induced incandescence." Optics Letters **20**(22): 2342-2344.

Worthing, A. G. (1926). "Spectral emissivities of Tantalum, Platinum, Nickel and Gold as a function of temperature, and the melting point of Tantalum." Physical Review **28**(1): 174-189.

You, X., A. V. Joshi, S. G. Davis, A. Laskin, F. N. Egolfopoulos, C. K. Law and H. Wang (2007). USC Mech Version II. High-Temperature Combustion Reaction Model of H2/CO/C1–C4 Compounds. http://ignis.usc.edu/USC_Mech_II.htm.

Zhao, H. and N. Ladommatos (1998). "Optical diagnostics for soot and temperature measurement in diesel engines." Progress in Energy and Combustion Science **24**(3): 221-255.

Appendix

An in-house fabricated thermocouple with cylindrical junction (thermocouple A) is compared to a commercially available bead thermocouple (thermocouple B) and a commercial butt-welded thermocouple (thermocouple C). Figure A1 (top) shows microscopic junction images of thermocouples A, B and C respectively. For thermocouple A, the junction was measured to have the same diameter of 200 μm as the adjacent wires and the location is illustrated by the red rectangle. For thermocouple B, the wire diameter is 200 μm and the junction is nearly spherical with a diameter of approximately 500 μm. Thermocouple C is a butt-welded thermocouple with wire diameter of 250 μm and a nearly cylindrical junction. Figure A1 (bottom) shows 532 nm filtered color images of the three heated glowing thermocouples above the flat premixed flame, with junctions in the middle of the wire.

In order to estimate of the potential uncertainty in using a thermocouple with an ill-defined junction, temperature measurements have been performed at the same location 3 cm above the premixed flat burner surface with the three S-type thermocouples. The temperature readings and derived gas temperatures are shown as blue/red plus, asterisk and cross signs in Fig. A2 for thermocouples A, B and C respectively. Nusselt number correlation for a cylinder as expressed by Eq. (3.2.4) is used for thermocouple A and C. The junction of thermocouple B is modeled as a sphere according to the microscopic image and the Nusselt number correlation for a sphere expressed by Eq. (A1) is used according to [Struk 2003] in the main text. Beyond the characteristic length and Nusselt number correlation, all other parameters are kept consistent for the three thermocouples.

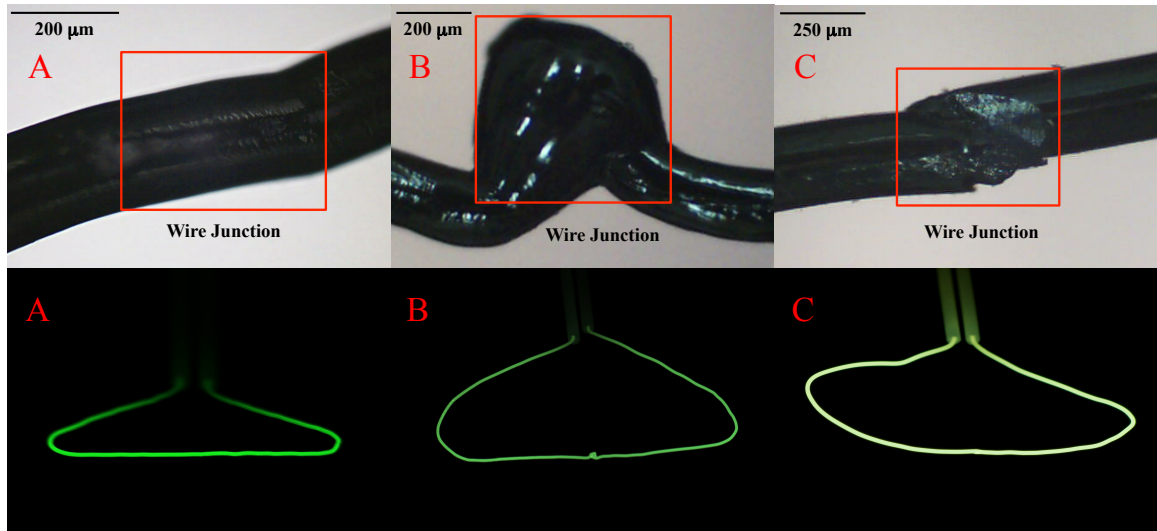$$Nu = 2 + \left(0.2 \times \mathrm{Re}^{0.82}\right) \qquad \text{(A1)}$$

Fig. A1. (Top) Microscopic images of thermocouple A, B and C. (Bottom) Color images of the heated glowing thermocouple A , B and C above a flat premixed flame through a 532 nm interference filter.
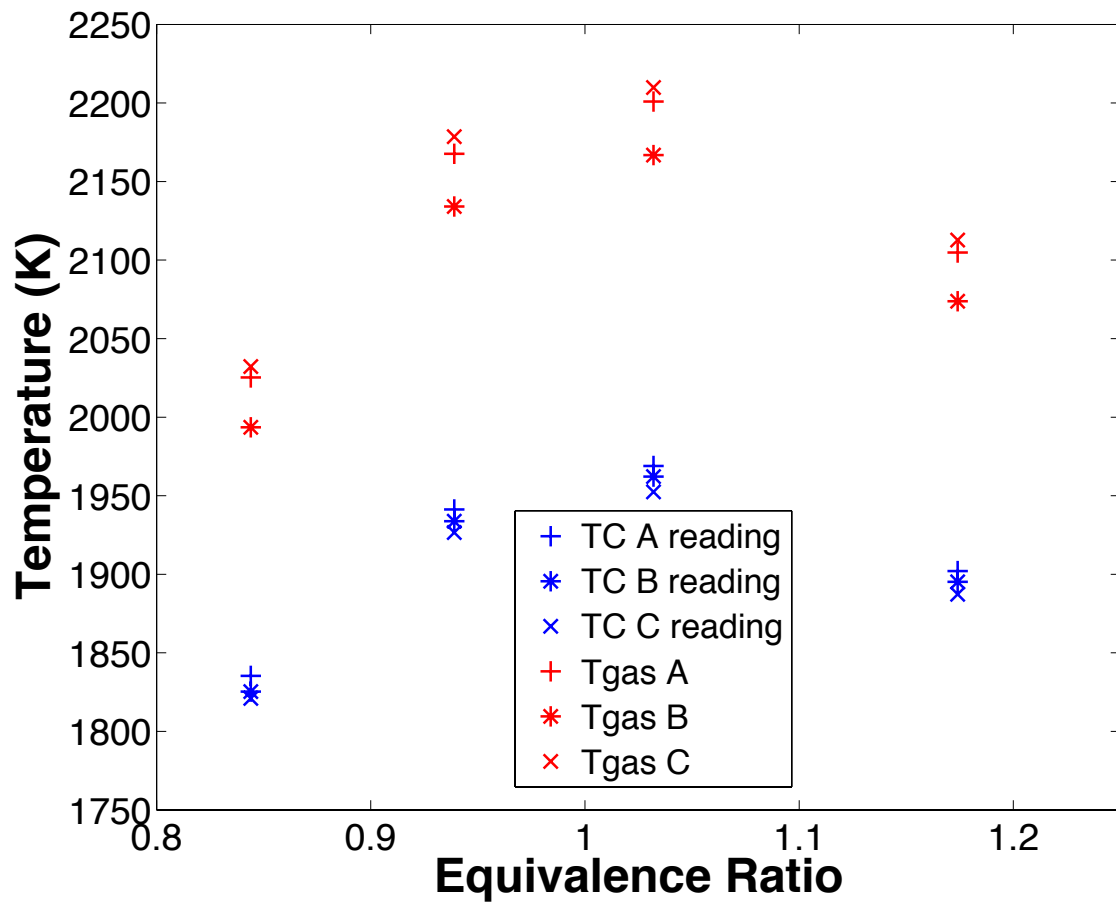
Fig. A2. Temperature measurements using thermocouples A, B and C.

As shown in Fig. A2, there is ~ 30 K difference in the derived gas temperature between thermocouples A and B and ~ 10 K difference between thermocouples A and C. The differences are most likely due to inaccurate Nusselt number correlations used in radiation correction for thermocouples B and C. Apparently, the junction of thermocouple B is neither an ideal sphere nor a nice spheroid as seen in the image of thermocouple B in Fig. A1. The butt-welded junction of thermocouple C is also not an ideal cylinder, as the two wires are not fully connected, causing the effective characteristic length for Reynolds number and Nusselt number to be smaller than 250 μm. The observation is in agreement with the temperature measurements shown in Fig. A2. The derived gas temperature from thermocouple C agrees perfectly with thermocouple A if 235 μm is used as the characteristic length. Therefore the radiation corrections for thermocouples B and C with ill-defined geometry apply within certain uncertainty. By contrast, thermocouple A has better accuracy given its simple and well-defined cylindrical geometry. Its accuracy is directly compared against CARS measurements as seen in Section 3.4 in the main text. Though admittedly not from a large sample set, the results suggest that self-manufactured thermocouples with well-defined cylindrical junctions can minimize temperature uncertainty, and commercial butt-welded thermocouples may have advantages over bead thermocouples.